Characterization of natural porous media by NMR and MRI techniques: High and low magnetic field studies for estimation of hydraulic properties

Von der Fakultät für Mathematik, Informatik und Naturwissenschaften der RWTH Aachen University zur Erlangung des akademischen Grades einer Doktorin der Naturwissenschaften genehmigte Dissertation

vorgelegt von

Diplom-Ingenieurin
Laura-Roxana Stingaciu
aus Tg-Jiu, Romania

Berichter: Universitätsprofessor Dr. rer. nat. Siegfried Stapf
Universitätsprofessor Dr. rer. nat. Bernhard Blümich

Tag der mündlichen Prüfung: 28. Mai 2010

Forschungszentrum Jülich GmbH
Institute of Chemistry and Dynamics of the Geosphere (ICG)
Agrosphere (ICG-4)

Characterization of natural porous media by NMR and MRI techniques: High and low magnetic field studies for estimation of hydraulic properties

Laura-Roxana Stingaciu

Schriften des Forschungszentrums Jülich
Reihe Energie & Umwelt / Energy & Environment Band / Volume 75

ISSN 1866-1793 ISBN 978-3-89336-645-3

Bibliographic information published by the Deutsche Nationalbibliothek.
The Deutsche Nationalbibliothek lists this publication in the Deutsche Nationalbibliografie; detailed bibliographic data are available in the Internet at http://dnb.d-nb.de.

Publisher and Distributor:	Forschungszentrum Jülich GmbH Zentralbibliothek 52425 Jülich Phone +49 (0) 24 61 61-53 68 · Fax +49 (0) 24 61 61-61 03 e-mail: zb-publikation@fz-juelich.de Internet: http://www.fz-juelich.de/zb
Cover Design:	Grafische Medien, Forschungszentrum Jülich GmbH
Printer:	Grafische Medien, Forschungszentrum Jülich GmbH
Copyright:	Forschungszentrum Jülich 2010

Schriften des Forschungszentrums Jülich
Reihe Energie & Umwelt / Energy & Environment Band / Volume 75

D 82 (Diss., RWTH Aachen, Univ., 2010)

ISSN 1866-1793
ISBN 978-3-89336-645-3

The complete volume ist freely available on the Internet on the Jülicher Open Access Server (JUWEL) at http://www.fz-juelich.de/zb/juwel

‘’To Andreas for his wisdom, to Lutz for his friendship, to Sigi for his trust and to Peter for his humor, together with my warmest thanks’’

…But I, being poor, have only my dreams;
I have spread my dreams under your feet;
Tread softly because you tread on my dreams.
W.B. Yeats

Contents

List of abbreviations and symbols

Abbreviations

NMR	Nuclear Magnetic Resonance
MRI	Magnetic Resonance Imaging
NMRR	Nuclear Magnetic Resonance relaxometry
^{1}H NMR	hydrogen proton NMR
MSO	multi-step-outflow
pF	water retention curve
RF	radio frequency
CPMG	Carr-Purcell-Meiboom-Gill
PSD	pore size distribution

Physical symbols

α	(mm, cm)	reciprocal value of the air entry value(bubble point)
B_0	(Tesla)	magnetic flux density
C	(cm^{-1})	soil water capacity
D	(m^2/s)	diffusion coefficient of water
D	(μm)	pore diameter
F	(N)	force
Φ	(-)	soil porosity
φ	(degrees)	liquid-solid contact angle
G	(Tesla/m)	magnetic field gradient strength
g	(m/s^2)	gravitational acceleration (9.80665m/s^2)
γ	(MHz/Tesla)	gyromagnetic ratio
H	(cm)	hydraulic head
h	(cm)	pressure head
h_m	(cm)	matric head
$\hbar$	(J·s)	Plank constant/ 2π ($1.054 \cdot 10^{-34}$ J·s)
K	(mm/min; cm/h)	soil hydraulic conductivity
K_r	(mm/min; cm/h)	unsaturated (relative) hydraulic conductivity
K_S	(mm/min; cm/h)	saturated hydraulic conductivity
k_B	(J/K)	Boltzmann constant ($1.38 \cdot 10^{-23}$ J/K)

m	(-)	vanGenuchten parameter
μ	(m^2/A or J/Tesla)	magnetic dipole moment
n	(-)	vanGenuchten parameter
ω_0	(MHz)	Larmor frequency
p	(N/m^2; bar; Pa)	pressure
p_a	(N/m^2)	air pressure
p_w	(N/m^2)	water pressure
r	(µm)	pore radius
ρ	(g/cm^3)	bulk density
ρ_1	(µm/ms)	longitudinal surface relaxivity
ρ_2	(µm/ms)	transversal surface relaxivity
q	(mm/min)	flux density
S/V	cm^{-1}	surface to volume ratio
σ_{wa}	(J/m^2; N/m)	surface tension of water-air interface (0.0725 J/m^2)
T	(ºC)	temperature
T_1	(ms)	spin-lattice relaxation time (longitudinal relaxation time)
T_2	(ms)	spin-spin relaxation time (transversal relaxation time)
T_E	(µs)	echo time
T_R	(s)	repetition time
θ	(cm^3/cm^3)	volumetric water content
θ_a	(cm^3/cm^3)	volumetric air content
θ_r	(cm^3/cm^3)	residual volumetric water
θ_s	(cm^3/cm^3)	saturated volumetric water content
ψ_w	($Kg{\cdot}m^2/s^2$)	soil water potential
ψ_g	($Kg{\cdot}m^2/s^2$)	gravitation potential
ψ_s	($Kg{\cdot}m^2/s^2$)	osmotic potential
ψ_{tp}	($Kg{\cdot}m^2/s^2$)	tensiometer pressure potential
ψ_m	($Kg{\cdot}m^2/s^2$)	matric potential
V_a	(cm^3)	volume of air phase
V_0	(cm^3)	total volume
V_w	(cm^3)	volume of water phase

1. Introduction

Soil is the natural material that covers most of the dry surface of the earth. It is the product of mechanical, chemical and biological interactions of different types of elements. Soils have a very complex composition and high variability in their occurrence and properties. The non-homogeneous mixture and interaction of their components and the changes induced upon usage ensures the complexity of their structure and a comfortable variable spatial distribution over the surface of the planet. The soils components can be found in nature in all the three aggregation states of matter: the solid state, the liquid state and the gas state. In spite of their complex structure and composition, soils can be easily handled and studied by a variety of methods. [*Koorevaar*, 1983]

Prediction of water movement in soils is a controlling factor in various processes of interest in water resources management such as: the runoff generation, the water and nutrients supply to vegetation, the groundwater recharge and contamination. From the physics point of view water distribution and transport in unsaturated soil represents a rather complex problem of porous media hydraulics. Among various techniques developed for investigating hydraulic phenomena in soils, Nuclear Magnetic Resonance (NMR) can be used successfully for the characterization of natural porous media.

1.1 Current state of NMR in soil

Nuclear Magnetic Resonance is a non-invasive and non-destructive method that allows various types of measurements in soils. One may differentiate between four ways of application: 1) NMR imaging (magnetic resonance imaging, MRI) allows for spatial detection of water contents and tracer transport [e.g., *Amin et al*., 1996; *Hermann et al*., 2002; *Pohlmeier et al*., 2008]; 2) NMR diffusometry determines the self-diffusion of the water molecules [*Callaghan et al.*, 1991; *Farrher et al*., 2007]; 3) NMR relaxometry (NMRR) determines magnetic properties of water such as longitudinal and transverse relaxation times in natural porous media [*Hinedi et al*., 1993; *Kleinberg*, 1996; *Hall et al*., 1997; *Votrubova et al*., 2000; *Stingaciu et al.,* 2009; *Pohlmeier et al*., 2009] and 4) NMR spectroscopy allows for analyzing and quantification of soil organic matter compounds [*Randall et al.*, 1997; *Kögel-Knabner*, 1997; *Lundberg et al*., 2001]. NMR relaxometry forms the basis of understanding signal intensities and contrast since MRI-signal intensities depend on local water content and relaxation times in the respective samples. In order to measure spatial water distributions one should first investigate the relaxometric properties of the porous media of interest.

The first use of the NMR technique for soil water monitoring was reported by *Matzkanin and Paetzold* in 1982. They tested the ability of MR technique to measure water content in packed soil samples. The same authors [*Paetzold and Matzkanin*, 1984; *Paetzold et al*., 1985] reported the use of MR techniques for soil water monitoring in field. *Tollner and Rollwitz*, [1988], published results of a study of the relationship between the NMR signal intensity and the water content of two packed soil samples at three different moisture contents. *Hinedi et al*., [1993], was the first to apply the concept of the pore size distribution assessment using the NMR relaxation measurements. *Hall et al*., [1997] reported the result of basic NMR measurements conducted for packed samples of 23 different soil materials using four different MR protocols. These results showed that many soils were characterized by quite fast relaxation times due to relaxation in local magnetic field gradients and they recommended the usage of low field NMR for the characterization of natural soils.

Over the last years new NMR methodologies and applications were developed and tested to quantify the total amounts of fluid phase, fluid saturation and porosity distributions [*Kleinberg and Horsfield*, 1990; *Latour et al*., 1995; *Hinedi et al*., 1997; *Schaumann et al*., 2005; *Ioannidis et al*., 2006, *Gladkikh et al*., 2007; *Stingaciu et al.,* 2009]. However, the majority of works on NMR relaxometry in natural porous media have been performed on consolidated porous materials such as rocks [*Hedberg et al*., 1993; *Kleinberg*, 1994; *Straley et al*., 1997] due to their importance for oil well logging applications.

In general, the amplitude of the ^{1}H NMR relaxation curve provides information about the fluid content of the rocks, while the transversal relaxation times are used for the characterization of the pore size distribution [*Dunn*, 2002]. On the other hand, echo intensities depend not only on the water content but also on relaxation times and experimental parameters such as echo time and repetition times. Therefore, *Edzes and van Dusschoten* [1998] proposed to use multi-echo MRI sequences for more reliable water content determination. Here, several echoes are recorded for each point in space, and convenient relaxation functions are fitted to the data yielding amplitude and relaxation time maps of the sample. The amplitude maps contain only information about the water content, and the influence of the samples texture is contained in the relaxation time maps. Most conventional NMR scanners operate at high magnetic field but prior knowledge [*Hall et al*., 1997; *Keating and Knight*, 2007] suggests the usage of low field scanners, which are currently under development for soil science, purposes [*Raich and Blümler*, 2004].

1.2 Aims

The aim of this thesis is to apply different NMR techniques for: i) understanding the relaxometric properties of unsaturated natural porous media and ii) for a reliable quantification of water content and its spatial and temporal change in model porous media and soil cores. For that purpose, porous media with increasing complexity and heterogeneity were used (coarse and fine sand and different mixture of sand/clay) to determine the relaxation parameters in order to adapt optimal sequence and parameters for water imaging. Conventional imaging is mostly performed with superconducting high field scanners but low field scanners promise longer relaxation times and therefore smaller loss of signal from water in small and partially filled pores. By this reason high and low field NMR experiments were conducted on these porous media to characterize the dependence on the magnetic field strength. Correlations of the NMR experiments with classical soil physics method like mercury intrusion porosimetry; water retention curves (pF) and multi-step-outflow (MSO) were performed for the characterization of the hydraulic properties of the materials.

Due to the extensive research the experiments have been structured in three major parts as follows. In the first part a comparison study between relaxation experiments in high and low magnetic field was performed in order to observe the influence of the magnetic field on the relaxation properties. Due to these results, in the second part of the study only low field relaxation experiments were used in the attempt of correlations with classical soil physics methods (mercury intrusion porosimetry and water retention curves) for characterizing the hydraulic behavior of the samples. Further, the aim was to combine also MRI experiments (2D and 3D NMR) with classical soil physics methods (multi-step-outflow, MSO) for the same purpose of investigating the hydraulic properties. Because low field MRI systems are still under developing for the moment [*Blümich et al.,* 2009], the MRI experiments were performed in high magnetic field and combined with MSO experiments in order to asses the changes in water content over the depth of the samples during pressure application, changes that are governed by the hydraulic properties of the material.

1.3 Short navigator

The thesis is structured into 7 major chapters. First chapter is an introduction to actual state of NMR research in soil science. The second and the third chapters are theoretical consideration over the NMR and soil physics methods that have been used for investigations. Nevertheless, only the basic theoretical aspects are covered here since due to extensive research we find it more appropriate to introduce each method used, separately, further on, into the content of the thesis. The materials and methods used for investigation differ from one part of the research to another; therefore they will be discussed in detail for each chapter separately. Chapter 4 is the comparison study between high and low field NMR; in chapter 5 is described the combination of low field NMR relaxometry with soil physics methods; chapter 6 presents the MRI studies on a coaxial sample and the parameterization of the water retention functions using a combination of MRI and MSO experiments. In chapter 7 a summary of the entire research is performed and the main conclusions are presented together with an outlook for further researches based on the obtained results.

2. NMR theoretical aspects

2.1 Spin & Precession

Spin, as the name suggests, was originally conceived as the rotation of a particle around some axis. In particle physics and quantum mechanics spin is a fundamental characteristic property of elementary particles, composite particles, and atomic nuclei. Spin can be positive or negative with value ½ or multiple of ½. Individual unpaired electrons, protons, and neutrons each possess a spin of ½. Two or more particles with spins having opposite signs can pair up to eliminate the observable manifestations of spin.

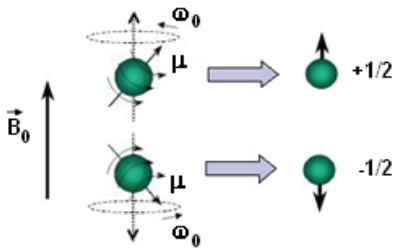

Fig.2.1.Particle with spin

When there is an odd number of nucleons, then there always exists one proton that is unpaired giving a magnetic dipole moment. In nuclear magnetic resonance, it is the unpaired nuclear spins that have importance (^{1}H, ^{23}Na, ^{13}C, ^{19}F).

In the absence of an external magnetic field, the spin polarizations (e.g. magnetic moments) are uniformly distributed, pointing in all possible directions in space (the distribution of the magnetic moments is completely isotropic). The total magnetic moment of the sample is very close to 0, since approximately the same number of spins point toward a given direction and opposite to it. When an external magnetic field, $\boldsymbol{B_0}$, is applied the magnetic moment associated with the spin, μ, starts to precess around the magnetic field lines with an angular frequency, ω_0, (Fig.2.1.) described by the *Larmor equation*:

$$\omega_0 = \gamma \cdot B_0 \qquad (2.1)$$

where γ is the gyromagnetic ratio (MHz/T) (see also Annex 1) and ω_0 is called the Larmor frequency. Therefore, the stronger the magnetic field is, the faster the spins will precess about it. During precession some of the spins are lined up (parallel) with the magnetic field $\boldsymbol{B_0}$ ⇨ lower energy state and some are aligned in the opposite direction of the magnetic field (antiparallel) ⇨ higher energy state. This orientation of the spins leads to a stable anisotropic

distribution of nuclear spin polarization, called thermal equilibrium. The spin populations of these two energy states are described by Maxwell–Boltzmann distribution:

$$\frac{n_-}{n_+} = \exp\left(-\frac{\hbar\gamma B_0}{k_B T}\right) \tag{2.2}$$

Where: n_+ = spin population from the lower energy state; n_- = spin population from the higher energy state; $\hbar$ = Plank constant/ 2π; k_B = Boltzmann constant; T = temperature. The difference between the amount of spin that precess parallel to the magnetic field and those which precess anti-parallel is the net magnetization, $\boldsymbol{M_0}$, the vector sum of all the individual spins polarizations. Since the individual spins precess out of phase with each other the net magnetization vector points along the direction of the $\boldsymbol{B_0}$ field and does not precess.

2.2 Excitation

Resonant absorption by nuclear spins will occur only when electromagnetic radiation of the correct frequency is being applied to match the energy difference between the nuclear spin levels, in a constant magnetic field of the appropriate strength (Fig.2.2.). The energy of an absorbed photon is then $E = \hbar\omega_0$, where ω_0 is the resonance radiofrequency that has to match, the Larmor precession frequency of the nuclear magnetization in the constant magnetic field $\boldsymbol{B_0}$.

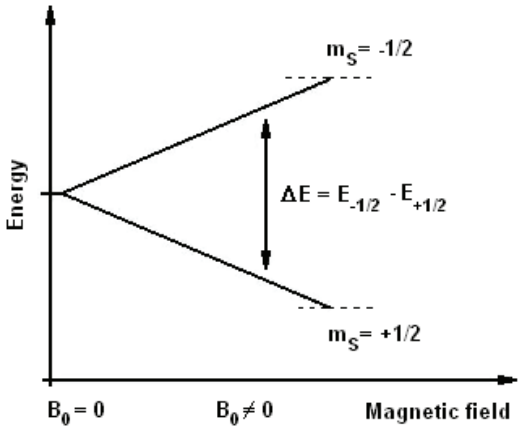

Fig.2.2.Energy difference between the nuclear spin levels

A magnetic resonance absorption will only occur when $\Delta E = \gamma\, \hbar B_0 = \hbar\omega_0$. Such magnetic resonance frequencies typically correspond to the radio frequency (RF) range of the electromagnetic spectrum for magnetic fields up to ~20 T. When a radio frequency pulse, e.g.

the magnetic component of the RF pulse, $\boldsymbol{B_1}$, with the characteristics described above is introduced into the system orthogonal to the main magnetic field, the protons that were previously aligned with the external magnetic field $\boldsymbol{B_0}$ (z axis) will begin to simultaneously precess about the axis of the new magnetic field $\boldsymbol{B_1}$ (x axis). This results in a spiral motion of the net magnetization vector, $\boldsymbol{M_0}$, from the z axis into the x-y plane, which is called nutation. As energy is added to the system by the RF pulse, the number of protons in both states can be equalized. When this occurs, a measurable longitudinal magnetization $\boldsymbol{M_0}$ no longer exists. In addition the RF pulse causes the spins to precess in phase with each other, a phase coherence effect, creating a transverse magnetization in the x-y plane, M_{xy}, which precesses at the Larmor frequency. In conclusion, the flip of the magnetization vector in the transverse plane is done both by in-phase precession of the spins as well as the nutation effect. When the entire vector flips into the x-y plane, the pulse that causes this flip is called a 90° RF pulse. The time it will take for an RF pulse to ''flip'' the spins in the transverse plane at the given RF strenght, $\boldsymbol{B_1}$, is given by equation:

$$\theta = 90^\circ = \pi / 2 = \gamma B_1 \tau_{\pi/2} \tag{2.3}$$

where θ is the flip angle and $\tau_{\pi/2}$ is the duration of the pulse. Consequently, an 180° pulse has twice the power or twice the duration of a 90° RF pulse. After 180° RF pulse the longitudinal magnetization vector $\boldsymbol{M_0}$ is inverted, and the spins begin to recover from $\boldsymbol{-M_0}$. An 180° RF pulse exactly reverses the equilibrium without inducing phase coherence, e.g. without creating transverse magnetization.

2.3 Relaxation

The process called relaxation refers to system nuclei that return to the thermodynamic equilibrium (the spins are relaxing back into their lowest energy state) in the magnet and the longitudinal magnetization before the 90° excitation pulse is recovered. Once the excitation RF pulse is turned off two types of relaxation processes will occur:

1) The spins will have to realign with the axis of the $\boldsymbol{B_0}$ magnetic field (lowest energy state) and give up all their excess energy→ res toration of thermal equilibrium. This process is called longitudinal relaxation and the time constant which characterizes the rate at which the z component of the net magnetization, M_z, recovers its initial value $\boldsymbol{M_0}$ is called longitudinal relaxation time, T_1 (spin-lattice relaxation time):

$$M_z(t) = M_0(1 - e^{-t/T_1}) \tag{2.4}$$

After an inversion pulse, the time constant which characterizes the rate at which the M_z component of the net magnetization recovers its initial value $\boldsymbol{M_0}$, is also the longitudinal relaxation time T_1 but the process is described by:

$$M_z(t) = M_0(1 - 2e^{-t/T_1}) \tag{2.5}$$

2) The spins will get out of phase with respect to each other because they are experiencing slightly different precession frequencies. This process is called transversal relaxation and the time constant that describes the rate at which the transversal magnetization, M_{xy}, decays is called transversal relaxation time, T_2 (spin-spin relaxation time) relaxation time:

$$M_{xy}(t) = M_0 \cdot e^{-t/T_2} \tag{2.6}$$

The result of the two relaxation processes is that the transverse component, M_{xy}, of the net magnetization vector decreases and $\boldsymbol{M_0}$ slowly recovers along the z axis.

2.3.1 Distribution of relaxation times

In a heterogeneous medium a multi-exponential decay of the signal is expected, and eq.2.6 is replaced by Laplace transformation of the distribution function which is represented by a semi-logarithmic plot of $\mathcal{F}(T_2)$ as a function of m logarithmically spaced T_2 relaxation times values [*Song et al*., 2002]:

$$M_{xy}(t) = \int_{T_2\,\min}^{T_2\,\max} \mathcal{F}(T_2)\exp(-n \cdot T_E / T_2)dT_2 + E(t) \tag{2.7}$$

The distribution function in eq.2.7 can be represented in a discretized matrix form:

$$\mathbf{Y} = \mathbf{KX} + \mathbf{E} \tag{2.8}$$

where $\boldsymbol{X}$ is the distribution function to be determined, $\boldsymbol{Y}$ is the measured signal, $\boldsymbol{K}$ is the known matrix of the kernel ($\exp(-n \cdot T_E/T_k)$) with T_k as the fixed relaxation times, and $\boldsymbol{E}$ is the experimental noise. However, the determination of the distribution function by a simple non-negative least square fit is a mathematically ill-posed problem.

To overcome this problem, a so-called regularization function is added to the system of equations. Several regularization procedures have been proposed, whereby the most commonly used one is the second derivative of the distribution function X'' which defines the smoothing amount, controlled by the regularization parameterα. Finally, the regularized variance can be written as:

$$\chi^2 = \left\|\mathbf{KX} + \mathbf{E}\right\|^2 + \alpha\left\|\mathbf{X}''\right\|^2 \tag{2.9}$$

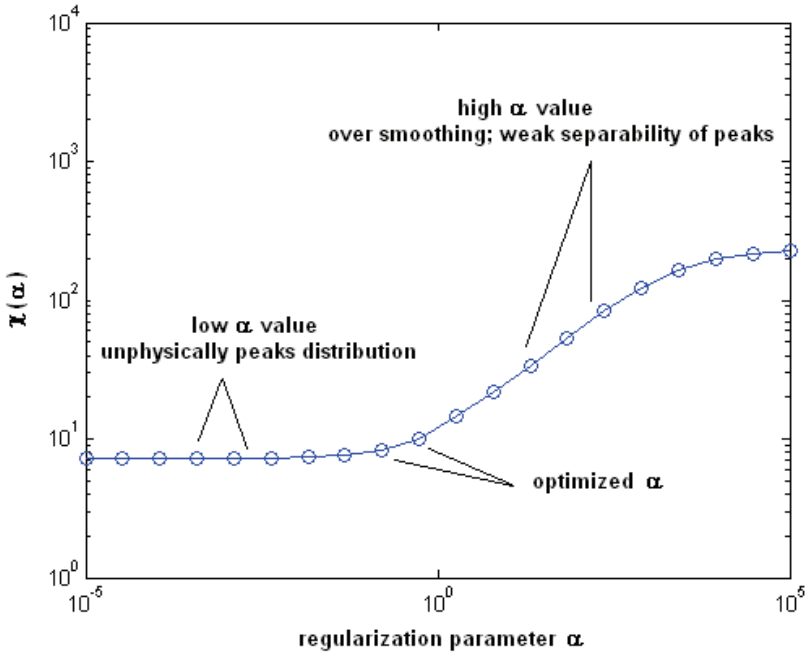

Fig.2.3.Determination of the regularization parameter α from the variance

The first right hand term in eq.2.9 is the classical least-square fit; the second term is the regularization function. The optimal value of the regularization parameter α is chosen from representation of χ^2 as a function of log α as demonstrated in Fig.2.3.

2.3.2. Relaxation in porous media

It has long been known that the NMR relaxation times as described above are only the apparent relaxations which for a fluid confined in porous media are constructed from three major relaxation times influenced by processes that can take place in a porous system as follow:

$$\frac{1}{T_{1,app}} = \frac{1}{T_{1,bulk}} + \frac{1}{T_{1,surf}} \tag{2.10a}$$

$$\frac{1}{T_{2,app}} = \frac{1}{T_{2,bulk}} + \frac{1}{T_{2,diff}} + \frac{1}{T_{2,surf}} = \frac{1}{T_{2,bulk}} + \beta T_E^2 + \frac{1}{T_{2,surf}} \tag{2.10b}$$

where $T_{1,2app}$ is the apparent relaxation time (s), $T_{2,\,diff}$ comprises the diffusion effect and $T_{1,2,\,surf}$ is the surface enhanced relaxation time. The factor β (s^{-3}) describes diffusion in local internal magnetic field gradients [*Barrie*, 2000]:

$$\beta = \frac{D}{12}(\gamma G)^2 \tag{2.11}$$

where D (m^2/s) is the diffusion coefficient of water and G (T/m) is the strength of the magnetic field gradient. For a porous media the dimensions of the pores are related to relaxation times by the Brownstein - Tarr equation [*Brownstein*, 1977; 1979]:

$$\frac{1}{T_{1,app}} = \frac{1}{T_{1,bulk}} + \rho_1 \cdot \frac{S}{V} \tag{2.12a}$$

$$\frac{1}{T_{2,app}} = \frac{1}{T_{2,bulk}} + \beta T_E{}^2 + \rho_2 \cdot \frac{S}{V} \tag{2.12b}$$

where ρ_1 and ρ_2 are the surface relaxivity parameters for longitudinal and transversal relaxation (μm/ms) and S/V is the pore surface to pore volume ratio (m^{-1}). From eq.2.12 T_1 and T_2 measurements can be used to determine surface relaxivity when information about the average surface to volume ratio is known from additional Brunauer-Emmett-Teller (BET) independent measurements [*Brunauer et al.*, 1938]. The surface relaxivity parameter is assumed to be constant for a given sample and is controlled by the surface properties of the pore walls. A recent study [Jaeger et al., 2009] has shown that the assumption of constant and homogeneously distributed surface relaxivity values is inconvenient for natural porous media at low water saturation. In macro-porous systems, there is normally fast exchange of the water molecules between the surface and bulk environments owing to rapid diffusion. In this case the diffusion term is usually neglected and eq.2.12 becomes:

$$\frac{1}{T_{1,2,app}} = \frac{1}{T_{1,2,bulk}} + \rho_{1,2} \cdot \frac{S}{V} \tag{2.13}$$

with $S/V = \alpha/r$ where r is the pore radius and α = 1, 2 or 3 is the shape factor for planar, cylindrical and spherical pore geometry, respectively [*Godefroy et al*., 2001; *Hinedi et al.* 1997].

2.4 MRI basics

Magnetic resonance imaging is the modality to construct images of the NMR signal from the hydrogen atoms in an object. However, if we transmit a radio frequency pulse, the received signal would be from the entire sample and there is no spatial discrimination. To encode the position of spins a spatially varied magnetic field (field gradient) is applied and each spin will experience a different magnetic field strength. The result is an NMR spectrum with more than one signal. This procedure is called position encoding and causes the resonance frequency to be proportional to the position *r(x, y, z)* of the spins.

$$\omega = \gamma(B_0 + r \cdot G_r) = \omega_0 + \gamma \cdot r \cdot G_r \tag{2.14}$$

If we transmit RF pulse with a desired frequency range (bandwidth) and turn on a field gradient in z direction (direction of the main magnetic field, B_0) in the same time, only the protons from a certain section of the sample that matches the precession frequency will resonate. As a result we will receive signal only from those particular protons. This procedure is called slice selection and the gradient is the slice-select gradient, $G_{z,}$ because it is used to gain signal only from a specific part (slice) of the sample. To select many slices from a sample the same gradient is used but the RF pulse's center frequency is modified. To avoid overlap of the signal from different slices, ''cross-talk'' as it is called in MRI, a gap must be introduced between the slices. Once the desired slice is selected the remaining problem is to differentiate between the protons within that slice. To solve this problem another two gradients are introduced: the phase-encoding gradient in y direction (G_y) and the readout or frequency-encoding gradient in *x* direction (G_x).

The phase encoding gradient is usually applied between the 90 and the 180˚ RF pulses or between the 180 pulse and the echo (see Fig.2.6.). After the 90 RF pulse all the proton in the selected slice precess at the same frequency (ω_0). When the gradient is applied in the *y* direction, spins from different levels of the slice will experience a different magnetic field so they will have different precession frequencies. Spins from the same level will remain in phase with one another but spins from different levels will experience different phase shift. When the gradient is stopped the spins will precess again at the same precession frequency but they will have a permanent phase shift (see Fig.2.4.). Differences in spatial position up and down are now reflected in that phase value. Hence, the gradient is called the phase encoding gradient.

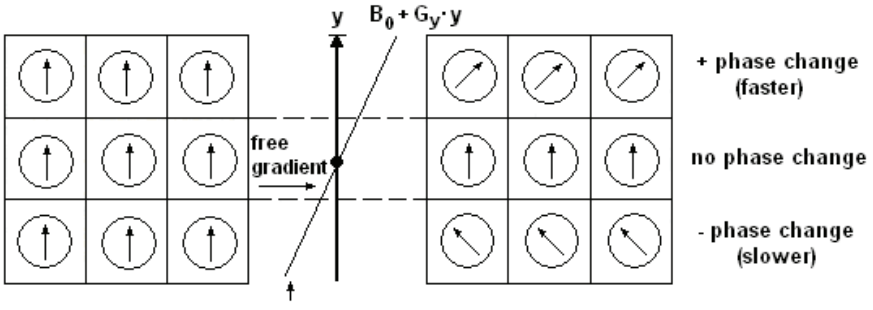

Fig.2.4.Phase encoding gradient

To be able to differentiate between spins from the same level that are still in phase with one another an additional gradient, G_x called the frequency encoding gradient, is introduced.

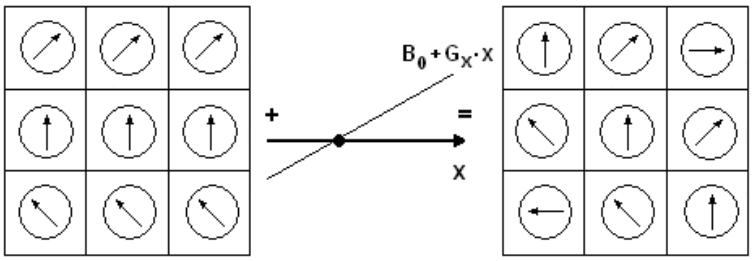

Fig.2.5.Frequency encoding gradient

This gradient is applied during the reception of the echo (readout) and will encode the position in the *x* direction by altering the Larmor frequency along the *x* axis. During the application of the readout gradient each spin will be characterized by a unique frequency and a unique phase (see Fig.2.5.).

A pulse sequence is a preselected set of defined RF and gradient pulses, usually repeated many times during a scan, wherein the time interval between pulses and the amplitude and shape of the gradient waveforms will control NMR signal reception and affect the characteristics of the MR images. Usual to describe pulse sequences, is to list parameters used in the sequence like: the repetition time, T_R, the echo time, T_E, if using inversion recovery, the inversion time, T_I, and in case of a gradient echo sequence, the flip angle.

One of the first and among the simplest pulse sequence used in MR imaging is the spin-echo *SE* sequence. It uses 90° radio frequency pulses to excite the magnetization and one or more 180° pulses to refocus the spins to generate signal echoes named spin echoes. The 90° excitation pulse rotates the longitudinal magnetization, M_z, into the xy-plane and the dephasing of the transverse magnetization, M_{xy} starts. The following application of a 180° refocusing pulse (rotates the magnetization in the x-plane) generates signal echoes. The purpose of the 180° pulse is to rephase the spins, causing them to regain coherence and thereby to recover transverse magnetization, producing a spin echo. The *SE* pulse sequence was devised in the early NMR days based on the detection of Hahn echo and later upgraded in the multi-echo sequence based on CPMG sequence of Carr and Purcell [*Carr and Purcell*, 1954; *Meiboom and Gill*, 1958]. More detailed information about this process will follow as the sequence is used in the experimental measurements (see 4.1.2).

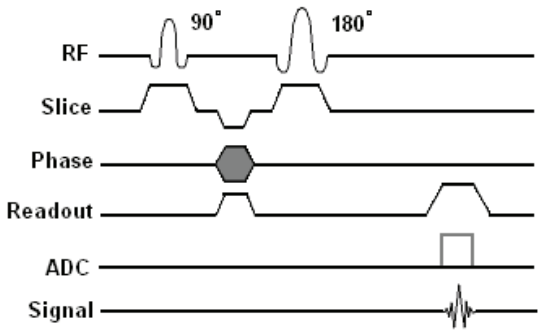

Fig.2.6.Spin-echo pulse sequence timing diagram

In Fig.2.6 the simplest form of a spin echo imaging sequence is illustrated. The SE sequence exists now in many forms: the multi echo pulse sequence using single or multi-slice acquisition; the fast spin echo imaging (FSE/TSE) pulse sequence; the gradient and spin echo (GRASE) imaging pulse sequences, etc. Nevertheless, due to some particular problems that SE sequences present when unsaturated porous media are investigated (see further in the thesis, chapter 6.1.7), in this work mainly single point imaging sequences have been used, in which a single data point per excitation is acquired, probing directly the FID with no echo involved.

2.5 *k*-space

k-space is the virtual reciprocal space which contains data from digitized MR signals recorded during data acquisition. The NMR signal is measured in the time domain, encoded and stored into ***k***-space defined by:

$$k_x = \frac{\gamma}{2\pi} G_x m \Delta t \tag{2.15}$$

and

$$k_y = \frac{\gamma}{2\pi} n \Delta G_y \tau \tag{2.16}$$

where x refers to frequency encoding, y to phase encoding, Δt is the sampling time (the reciprocal of sampling frequency), τ is the duration of G_y (phase encoding gradient), γ is the gyromagnetic ratio, m is the sample number in the frequency direction and n is the sample number in the phase direction (also known as partition number). From this data set, ($\boldsymbol{k}_x$, $\boldsymbol{k}_y$), in

reciprocal space (m^{-1}) the encoded signal $p(k_x,k_y)$ is transformed in signal intensity distribution in real space, (x,y), by the meaning of 2D-Fourier Transformation:

$$M_0(x,y) = (2\pi)^{-2} \iint p(k_x,k_y) \exp\{-ik_x x\} \exp\{-ik_y y\} dk_x dk_y \qquad (2.17)$$

Thus, spatial frequency and position constitute a Fourier transform pair (pair of Fourier-conjugated variables).

Different imaging experiments are distinguished in the way how ***k***-space is being sampled. For a simple spin echo sequence the *x* direction contains the frequency domain information and the *y* direction contains the locations of spins in the phase encoding gradient direction. The center of the ***k***-space contain the phase encoding step with weakest gradient and thus with the highest signal. The periphery of the ***k***-space will contain those phase-encoding steps with the largest gradients and thus with the least signal (Fig.2.7.). Because of the oscillating nature of the signal the image of the ***k***-space will appear as a series of concentric rings with alternating high and low intensity and an overall decrease in intensity as one goes from the center to periphery. The Fourier transformed data are displayed as an image by converting the intensities of the peaks to intensities of pixels representing the tomographic image. Detailed explanations on the NMR-MRI principles can be found in several text books from which the content of this chapter was inspired: *Callahan*, [1991]; *Blümich*, [2000]; *Hashemi et al*., [2004]; *Blümich*, [2004]; *Hornak*, [2006]; *Levitt*, [2007].

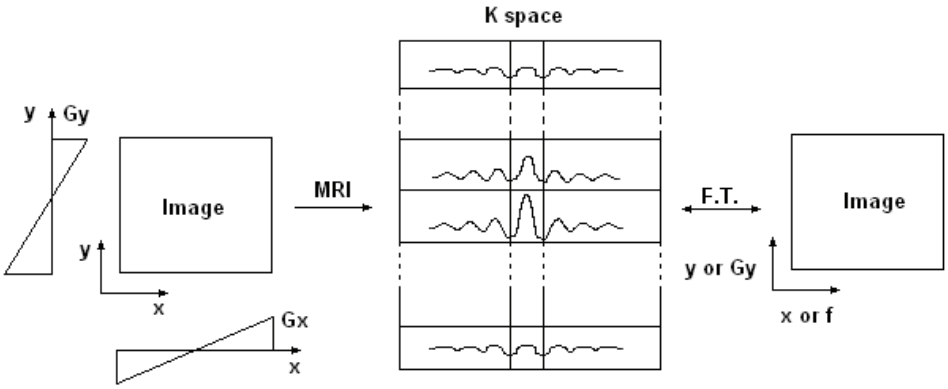

Fig.2.7.The relationship between frequency and position along the x axis and between phase-encode gradient increment and position along the y axis

3. Soil physics: basic considerations

Soil physics deals with physical processes in the pedosphere. In the three phase model the soil is described on the macroscopic scale by continuous fields, in particular by the phase densities of the soil matrix, soil water and soil air and by the respective energy densities. The distribution of energy is of fundamental importance for the behavior of the system because energy gradients are the driving forces for fluxes of matter and energy. Of particular interest are structure and dynamics of the soil matrix and the multitude of mass and energy fluxes through soil and along its surface.

3.1 Potential theory

In the simplest assumption, the solid soil matrix (solid phase) is a rigid porous structure that is made up of crystalline and quasi - crystalline particles. The structure of the matrix is presumed to be invariant in time and its energy density is constant. The soil water (liquid phase) consist of water with some dissolved chemicals for which we assume that they do not influence the physical properties of the fluid. The volumetric phase densities of the two fluid phases (water and air) in soil matrix are described by:

$$\theta_w = \frac{V_w}{V_0} \text{ and } \theta_a = \frac{V_a}{V_0} \tag{3.1}$$

Where θ_w and θ_a are the volumetric water and air content; V_w and V_a are the corresponding volumes of water and air phases and V_0 is the total volume of the soil matrix considered. The sum $\Phi = \theta_w + \theta_a$ is the porosity of the soil. In a porous medium, numerous forces act on soil water, the force field is composed of a variety of divergent partial forces. By virtue of its position in this force field, a unit quantity of soil water possesses potential energy.

The potential energy of the soil water may be defined by the work that is required for moving an infinitesimal volume of water from a reference state into the desired state within the soil matrix. The density of the soil's water potentials energy is called the soil water potential ψ_w. In accordance with the recommendations of the International Soil Science Society [*Bolt*, 1976] we distinguish three partial potentials:

Gravitation Potential ψ_g: The energy density (energy per volume of water) required to move an infinitesimal volume of pure, free water from the reference depth z_0 to a depth z. Notice the sign convention which makes z-z_0 negative if z is above z_0, hence the gravitational energy higher than at the reference point.

Osmotic Potential ψ_s: The energy density required to add to the infinitesimal volume of water at depth z the dissolved chemicals from a reservoir also at depth z.

Tensiometer Pressure Potential ψ_{tp}: The energy density required to bring the infinitesimal volume of soil solution (pure water with dissolved chemicals added) from the reservoir at depth z with pressure p_0 isothermally and reversibly into the soil. This potential encompasses the effects of surface adsorption, surface tension, air pressure and hydrostatic pressure, pressure from a non-rigid soil, matrix and overburden pressure. An important special case is a rigid, unsaturated soil where the air pressure is constant everywhere and equal to p_0. The only component of the tensiometer pressure potential then comes from the energy required to move water into the porous matrix. It is negative for unsaturated soil because water is transferred into a state of lower energy. Since the potential is determined by the soil matrix it is called the matric potential and denoted by ψ_m. Recognizing the three potentials ψ_g, ψ_s and ψ_{tp}, we write the total soil water potential as

$$\psi_w = \psi_g + \psi_s + \psi_{tp} \tag{3.2}$$

This reflects the three steps required to move pure, free water from the reference state to the required state in the soil: (i) moving it from z_0 to z in the gravitational field, (ii) adding the required dissolved chemicals from a reservoir at depth z, and (iii) transferring the solution into the soil environment at depth z. The potential on weight basis has the dimension of height and is called head. The head equivalent of the pressure potential is called pressure head, h,

$$h = \psi_{tp} / g \tag{3.3}$$

where g is the gravitational acceleration (m/s^2). The head equivalent of the soil water potential (hydraulic potential) is the hydraulic head, H. Referring to the special case described above; h_m, the matric head is the equivalent head of the matric potential.

3.2 Soil water characteristic

The relation between the matric potential, ψ_m(or matric head h_m) and the volumetric water content θ which is essentially determined by the geometry of the pore space is called the soil water characteristic. It is of fundamental importance for the hydraulic characterization of a soil because it relates an energy density (potential of driving force) to a capacity quantity (water content). The region which encompasses all possible $\theta(\psi_m)$ curves is limited by the desorption $\theta_d(\psi_m)$ and the adsorption curves $\theta_a(\psi_m)$ see Fig.3.1. The desorption curve results when water is slowly and monotonically removed from an initially water saturated soil until

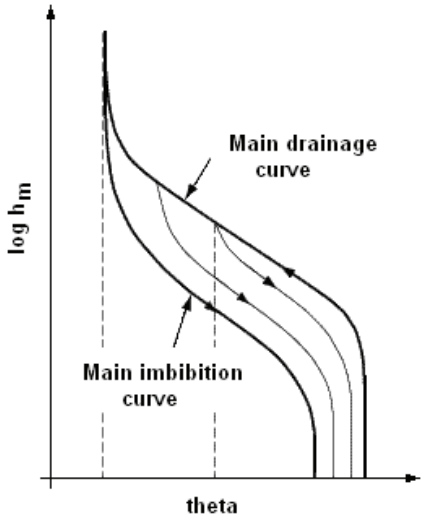

Fig.3.1.Adsorption and desorption characteristics with primary scanning curves

the soil is air saturated. The adsorption curve describes the reverse process. The air can only enter the porous medium after the matric potential has dropped below a certain value the so-called air-entry value. It is determined by the largest opening of the porous medium to the outside. After air has entered the porous medium, the water content, θ, decreases monotonically with increasingly negative matric potential ψ_m. This decrease consists of continuous stretches and of discontinuous jumps. The jumps are caused by cavities that are connected to the outside through small channels. In these channels, a process occurs which is similar to the air entry into the entire medium. The potential ψ_m must drop below a certain value before the cavity behind it can be emptied. These jumps therefore define local air entry values of narrows. The value of $\Delta\theta$ for such a jump at ψ_m indicates the volume fraction which is blocked by a narrow of radius $r = -2\sigma_{wa}/\psi_m$ where σ_{wa} is called the surface tension of water-air interface and at 20˚C has a value of 0.0725 J/m^2.

A common interpretation of the desorption curve is that the pore volume which is water filled at a certain potential ψ_m consist of structure with radii smaller then $-2\sigma_{wa}/\psi_m$. Nevertheless this interpretation is only correct for a non-hysteretic medium. Despite the difficulties associated with measuring the soil water characteristic it is one of the traditional soil physical laboratory methods. For these measurements a pressure difference $\Delta p = p_w - p_a$ is created across the water – air interface of a soil sample and the volumetric water content θ is measured as a function of Δp. To establish the pressure difference, the air phase is

connected to an air reservoir at pressure p_a and the water phase to a water reservoir at pressure p_w (Fig.3.2.).

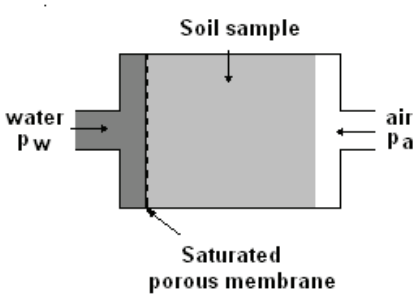

Fig.3.2.Idealized instrument for measuring soil water characteristic

The latter connection is done with a water saturated porous membrane which prevents the air phase from entering into the water reservoir. To prevent water evaporation into the air reservoir, the relative humidity is controlled such that the soil water potentials in the water and in the air phase are identical. The same methods may be used for measurements in multiphase systems. There, each phase α is connected to a reservoir at pressure p_α by a membrane that is only permeable for phase α. We only consider the case of two fluid phases, water and air, and note that the method may be used in two alternative variants:

Suction Method: Pressure p_a in the air phase is equal to atmospheric pressure p_0 and $p_w < p_0$ is varied [*Haines*, 1930]. The method has the major limitation that p_w cannot become smaller than the vapor pressure [*Klute,* 1986b]. The method is well suited for measuring the relation between the volumetric water content θ and the matric potential ψ_m as it exists in soils under natural conditions.

Pressure Method: The pressure p_w in the water phase is equal to the atmospheric pressure and $p_a > p_0$ is varied [*Richards and Fireman*, 1943]. It is generally used to roughly determine the texture of the pore space. Discrepancies between the methods can be expected for $\psi_m \approx -p_0$. The soil water characteristic has two main fields of application. First it is required for modeling the movement of water in soils and the second application is in the rough ecological assessment of a site. Here, typical quantities of interest are the storage capacity of the soil and the availability of the stored water for plants. The required precision is generally rather small because (i) large differences occur between different soil types and (ii) other important system parameters, like the water stress function of various plants, are not known sufficiently well.

3.3 Flow of water in soil

Water is present in every soil profile, but the amount varies with time and place as a result of a supply and demand by its environment. In a state of equilibrium the total soil water potential is constant at any given point of the system. However, in an open system it is unlikely to have this state of equilibrium, since processes like the infiltration of rain or the evapo – transpiration of soil water cause permanent disturbances. For example, the total soil water potential is raised by infiltrating rain and decreased by the extraction of soil water by plant roots, processes that lead to a gradient in the total soil water potential. This gradient is the driving force for water movement in soils. In case of existing potential gradients, soil water will flow from regions of higher potential to regions of lower potential [*Jury et al.*, 1991]. The relationship between the driving force and the ensuing flux density is called the flux density equation or Darcy law which describes the laminar water movement in saturated, rigid soils:

$$q = -K\frac{\partial H}{\partial z} \tag{3.4}$$

where q is the flux density (the volume of water passing the area unit per time unit); H is the hydraulic head (m); K is the hydraulic conductivity (m/s) (the coefficient that measures the ability of the soil to conduct a flow of water) and z is the vertical coordinate (m). The law of conservation of matter is expressed in the so called continuity equation. For one dimensional flow of water in soil the continuity equation can be written as follows, where θ is the volume fraction of water:

$$\frac{\partial \theta}{\partial t} = \frac{\partial q}{\partial z} \tag{3.5}$$

Due to this, many types of flow can be considered:

- steady flow in saturated soil:

  $\frac{\partial \theta}{\partial t} = 0$ and $\theta = \Phi$

  q, K and θ are constant in time and position.

- steady flow in unsaturated soil:

  $\frac{\partial \theta}{\partial t} = 0$ and $\theta < \Phi$

  q is constant in time and position but K and θ are constant only in time.

- nonsteady flow in unsaturated soil

  $\frac{\partial \theta}{\partial t} \neq 0$ and $\theta < \Phi$

q, K and θ vary with time and position.

- nonsteady flow in saturated soil

  $\frac{\partial\theta}{\partial t} \neq 0$ and $\theta = \Phi$

  θ *is* constant but q and K vary in time.

If a saturated soil begins to drain, part of the pore volume fills with air. As a consequence, the water conductive-part of the cross sectional area decreases, the tortuosity of the flow path increases, and the remaining soil water moves in relatively small pores where the flow resistance is increased. As a result, the hydraulic conductivity K decreases rapidly with decreasing water content. For this reason any description of water movement in variably saturated media has to consider K as a function of θ. According to Buckingham - Darcy law [*Buckingham*, 1907], the one-dimensional, vertical water movement in unsaturated soils can be written as [*Jury et al*., 1991]:

$$q = -K(\theta)\frac{\partial H}{\partial z} = -K(\theta)\left[\frac{\partial h_m}{\partial z} - 1\right] = -K(\theta)\frac{\partial h_m}{\partial z} + K(\theta) \tag{3.6}$$

where $K(\theta)$(m/s) is the hydraulic conductivity function and h_m is the matric head (m). *Richards*, [1931], linked the Buckingham-Darcy law with the water conservation equation. Accordingly, the governing equation for the one-dimensional, vertical and variably saturated water flow without sinks and sources is given by:

$$\frac{\partial\theta}{\partial t} = \frac{\partial}{\partial z}\left[K(\theta)\frac{\partial h_m}{\partial z} - K(\theta)\right] \tag{3.7}$$

Equation 3.7 is called the mixed form of the Richards equation. This equation contains two unknown variables (θ and h_m) and it can't be solved. This difficulty may be overcome by using the water retention characteristic $\theta(h_m)$, which relates the volumetric water content θ to the energy state of soil water, the matric head h_m. Due to the fact that for unsaturated soils h_m covers a wide range of negative values, it is conveniently plotted as the decaying logarithm of the absolute value of h_m given in centimeters ($\log \mid h_m \mid$). This expression is referred to as the pF-value. To eliminate θ from the left side of eq.3.7, the partial derivative may be reorganized using the chain rule [*Jury et al*., 1991]:

$$\frac{\partial\theta}{\partial t} = \frac{d\theta}{dh_m}\frac{\partial h_m}{\partial t} \equiv C(h_m)\frac{\partial h_m}{\partial t} \tag{3.8}$$

with $$C(h_m) = \frac{d\theta}{dh_m} \tag{3.9}$$

where $C(h_m)$ is the soil water capacity function, which is equal to the slope of $\theta(h_m)$. Note that $C(h_m)$ is defined only for a uniform wetting or drying process in which $\theta(h_m)$ is described uniquely by a single curve. Eliminating θ from the hydraulic conductivity function on the right side of eq.3.7 is straightforward. Since $K(\theta)$ is a function of θ and $\theta(h_m)$ is a function of h_m, K may be written directly as a function of h_m:

$$K(\theta) \equiv K\left[h_m(\theta)\right] \equiv K(h_m) \tag{3.10}$$

Inserting $C(h_m)$ into the mixed form of the Richards equation and substituting $K(\theta)$ by $K(h_m)$ finally yields:

$$C(h_m)\frac{\partial h_m}{\partial t} = \frac{\partial}{\partial z}\left[K(h_m)\frac{\partial h_m}{\partial z} - K(h_m)\right] \tag{3.11}$$

Equation 3.11 is called the matric head form of the Richards equation. It may be solved if boundary and initial conditions are specified and $C(h_m)$ and $K(h_m)$ are known.

3.4 Parametrization of the water retention curve

To solve the Richards equation, the water retention characteristic $\theta(h_m)$ and the hydraulic conductivity function $K(h_m)$ must be known. While $\theta(h_m)$ is an expression of the ability of a soil to store water, $K(h_m)$ is a measure of the ability to transmit water. Both are nonlinear functions, with h_m and K varying over many orders of magnitude. A very unfortunate characteristic of the water retention function is its hysteretic nature. Hysteresis implies, that the water content one is measuring for a given matric head value is not unambiguously defined. Rather it is depending on the history of drainage and wetting processes antecedent to the water content measurement.

In general, θ during drainage will be greater than during wetting for a given value of h_m (see also Fig.3.1.). Even though empirical hysteresis models exist, that can be implemented in numerical simulation schemes [*Kool and Parker*, 1987]; hysteresis is simply ignored in most applications. In those cases, the $\theta(h_m)$ relationship is given uniquely by the main drainage curve that is obtained by draining a soil sample from saturation. Most of the methods used to estimate the $K(\theta)$ [*Mualem*, 1976; *van Genuchten* 1980; *Kool at all*, 1985; *Parker et all*, 1985] require a parametric model for the hydraulic functions and they merely yield the values of the parameters which lead to an optimal agreement with the data. These methods are referred to us as ‘’parameters estimation’’.

In 1980, van Genuchten presented a now widely used class of functions for parametrizing measured soil water characteristics. To formulate the functions, he introduces the water saturation Θ:

$$\Theta = \frac{\theta - \theta_r}{\theta_s - \theta_r} \tag{3.12}$$

where θ_s is the volumetric water content at saturation and θ_r is the residual volumetric water content. From previous discussion one would expect that $\theta_s = \Phi$ and $\theta_r = 0$. However, it is experimentally often found that the maximal water content is smaller than the porosity Φ. This is in particular the case in field studies and is caused by: (i) entrapped air and (ii) very large pores which drain so rapidly that they cannot be saturated. The residual water content on the other hand is usually attributed to adsorbed water. Often however, θ_r is simply required to gain additional flexibility in the class of functions. The van Genuchten parametrization is traditionally written in terms of the matric head instead of the matric potential:

$$\Theta(h) = \left[1 + [\alpha h]^n\right]^{-m} \tag{3.13}$$

where a, n and m are positive parameters Given a set of N measured points from the soil water characteristic, these parameters are chosen such that the deviation between Θ(h) given by eq.3.13 above and the set of measured points is minimal. If the agreement between the function and the data is deemed acceptable, the set of N numbers is described by the five parameters θ_s, θ_r, α, n and m, thence the name parametrization. One often encounters a parametrization which is based on the subset of functions obtained by choosing m = 1 - 1 / n in eq.3.13. The aim of parametrizing the soil water characteristic is to obtain a simple description of a comprehensive set of measurements. In contrast, the aim of parametrizing the unsaturated (relative) hydraulic conductivity $K_r(\psi)$ is generally to interpolate and often also to extrapolate a small number of measurements. This is only feasible if the parametrization is based on a correct representation of the physical structure of the water filled pore space. The most common models assume that the pore space basically consists of a set of capillaries and that the soil water characteristic describes the distribution of their radii. From this distribution and presuming laminar flow in each capillary, the unsaturated hydraulic conductivity is then calculated. Between various models proposed [*Burdine,* 1953; *Mualem,* 1976; *Mualem and Dagan,* 1978] the most widely used parametrization of the unsaturated hydraulic conductivity is the Mualem-van Genuchten model [*van Genuchten*, 1980]:

$$K_r(\psi) = K_s \frac{\left[1 - (\alpha h)^{mn}\left\{1 + (\alpha h)^n\right\}^{-m}\right]^2}{\left[1 + (\alpha h)^n\right]^{\frac{m}{2}}} \tag{3.14}$$

where K_s is the saturated hydraulic conductivity. The theoretical information contained in this chapter is based on citations from several text books: *Koorevaar et al*., [1983]; *Jury et al*., [1991]; *Roth*, [1996]; *Jury and Horton*, [2004].

4. Characterization of porous media by high and low-field NMR relaxometry

In this first step a comparison study of NMR relaxometric behavior of model porous media at high and low magnetic field was performed to assess the effect of magnetic field strength on transversal relaxation time and signal amplitude at different degrees of saturation in order to determine how the magnetic field strength will influence the estimation of water content within the samples. As model systems four mixtures of medium sand and variable fraction of kaolin clay were used, whose relaxometric properties are investigated at a 300 MHz (7T) high field and a 4.2 MHz (0.1T) low field scanner. T_2 relaxation curves were monitored by the Carr-Purcell-Meiboom-Gill sequence (CPMG) and further analyzed by inverse Laplace transformation yielding T_2 distribution functions. Signal behavior with variation of saturation degree and clay composition was monitored to assess the influence of water and clay content.

4.1 Materials and Methods

4.1.1 Porous media

Four samples were prepared from pure sand (FH31, Quarzwerke Frechen, Germany) with a grain size distribution of: 2% (>0.72mm), 8%(0.71-0.5mm), 30%(0.5-0.355mm), 41%(0.36-0.25mm), 16%(0.25-0.18mm), 3%(<0.18mm) mixed with kaolin clay (Sigma-Aldrich, Germany) in a range of 0, 5, 10, and 15 mass percentages. In the following, these samples will be named as FH31, Mix5, Mix10, and Mix15, respectively. For more information about the structure of materials used in the experiments see Annex 2.

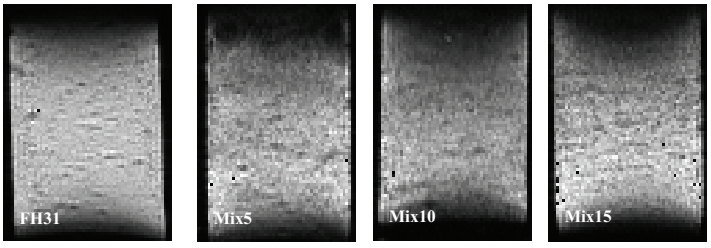

Fig.4.1.MRI images for the saturated samples recorded at T_E = 2ms and a resolution of 0.24mm^2 per pixel (FOV: 70 x 28 mm)

The sand/clay mixtures were carefully homogenized (MRI images of thin slices of the samples are presented in Fig.4.1 and they show homogeneous distribution of the water content in the saturated samples) and filled into glass tubes with an inner diameter of 24mm and a height of 46mm. The bottom of the tubes consists of a porous glass plate with a pore size between 40-90µm (RoBu, Germany). This allows saturating the system from the bottom which was carried out for all samples with degassed water for one day, after which the samples were sealed on both ends. Unsaturated conditions were obtained by removing the seal on the top of the samples to allow evaporation for a certain time and then the seal was replaced. Before measurement, each sealed sample was allowed to equilibrate at room temperature for one day. The characteristics for all samples: bulk density (g/cm^3); saturated water content θ_s (cm^3/cm^3) and the bulk water content after each evaporation step are summarized in Table 4.1.

Table 4.1. Characteristic data of the samples for each evaporation step. Note that the water contents were determined gravimetrically

Sample	Bulk density g/cm^3	θ_s cm^3/cm^3	Water content – evaporation steps θ_a, cm^3/cm^3				
			1	2	3	4	5
FH31	1,69	0.36	0.28	0.26	0.20	0.10	0.05
Mix5	1,57	0.39	0.30	0.26	0.17	0.11	0.06
Mix10	1,59	0.40	0.36	0.26	0.20	0.12	0.09
Mix15	1,60	0.39	0.27	0.19	0.15	0.08	0.05

4.1.2 NMR setup

For high field experiments a 7T (300MHz ^{1}H resonance frequency) vertical wide bore superconducting magnet (Oxford Instruments, UK) connected to a Varian console was used. The NMR RF-resonator is a 'birdcage - type' resonator with an internal diameter of 3.8cm and 7cm length. The low field experiments were conducted on a 0.1T (4.2MHz ^{1}H resonance frequency) Halbach magnet (ACT, Aachen-Germany) as described in *Raich et al*. [2004], connected to a KEA spectrometer (Magritek, New Zeeland). The resonator was a solenoid RF-coil of 3.5cm inner diameter and 5cm length. The temperature in the laboratories was regulated to 21°C.

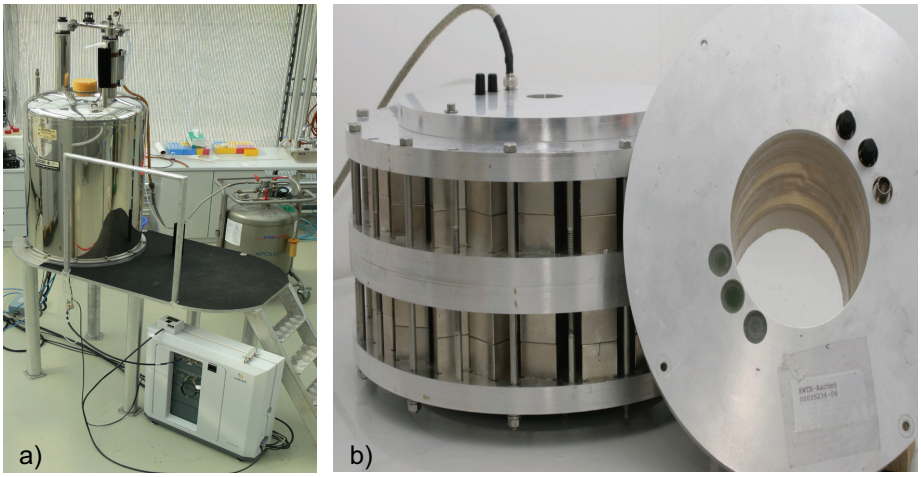

Fig.4.2.NMR setup: a) 7T superconducting magnet; b) Halbach 0.1T magnet.
Pictures not to scale

For the determination of signal amplitude and T_2 relaxation time the CPMG (*Carr-Purcell-Meiboom-Gill)* pulse sequence was employed [*Carr and Purcell*, 1954; *Meiboom and Gill*, 1958]. This multiple pulse sequence consists of the application of a 90° RF excitation pulse followed after duration of $T_E/2$ by a series of 180° RF pulses of distance T_E in order to refocus the net magnetization. After the i^{th} 180° pulse, a spin-echo is formed of which only the central point is acquired with a delay of i T_E (i = 1…*n*) referred to the initial 90° RF pulse (Fig.4.3.).

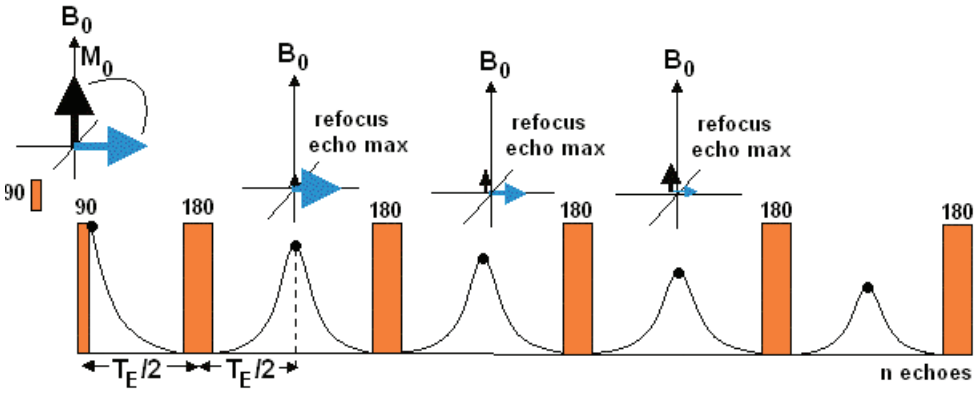

Fig.4.3.CPMG pulse sequence: after application of the 90° RF pulse the magnetization M_0 (black arrow) is inverted in transversal magnetization (blue arrow) and slowly recovered after relaxation as explained in chapter 2.3.

Parameters used for the high field measurements are: T_E = 0.4ms (the minimum possible with this setup), number of echoes n = 10000, repetition time, T_R = 6s for a number of 2 signal accumulations. For low field experiments the parameters were: T_E = 0.2ms (the smallest echo times which do not produce truncated information), n = 12000 and T_R = 6s for a number of 64 accumulations. The number of acquisition points was in all cases sufficiently high so that the CPMG curves decreased completely into the noise. High field images of the saturated samples have been recorded with T_E = 2ms and a resolution of 0.24mm^2 per pixel (128 x 64 pixels for a field of view of 70 x 28mm).

4.1.3 Numerical simulations

In general, evaporation will change the water content distribution within the sample, with lower values at the top end and increasing water contents towards the bottom end. This water content distribution may potentially influence the NMR results. To evaluate the uncertainty in the assumed homogeneity of the sample the water content distribution within the different samples after each evaporation step was analyzed using numerical simulations. Therefore, the software package HYDRUS-1D [*Šimůnek et al*., 1998] was used which solves numerically Richards's equation (eq.3.7). The hydraulic properties for the sand/clay mixture were estimated using the program Rosetta [*Schaap et al*., 2001] and are listed in Table 4.2.

The effect of evaporation on the soil water content distribution was simulated for a soil profile of 46 mm non-equidistantly discretised with 300 nodes. The system was initialized in pressure head h = 0 (full saturation). The upper boundary was set to variable flux which represents the actual evaporation rate over time calculated from mass (water) loss of each substrate between two consecutive evaporation steps. The evaporation steps and the bulk water loss of the laboratory experiment are listed above in Table 4.1.

Table 4.2. Soil hydraulic parameters used for the numerical simulations

Sample	θ_r cm^3/cm^3	θ_s cm^3/cm^3	α cm^{-1}	n -	K_S cm /h	I -
FH31	0.0507	0.36	0.0308	4.2464	46.43	0.5
Mix5	0.0565	0.39	0.029	3.2157	24.53	0.5
Mix10	0.0594	0.40	0.029	2.2707	8.83	0.5
Mix15	0.0627	0.39	0.0256	1.7511	3.46	0.5

4.2 Results and Discussions

4.2.1 Relaxation behavior of saturated systems

Figure 4.1. shows MRI images of the investigated samples. Displayed is the central part (50 x 28mm) of the columns; the concave curvatures of the upper and lower boundaries are due to the limit of the RF field. However, the following relaxometric investigations are also performed within these boundaries, so the images represent the investigated volume of the samples. From Fig.4.1. it is clear that the heterogeneity is in all cases quite similar, the medium sand and the mixtures look identical, no large scale separation of clay and sand is observed. However, some microscopic heterogeneity remains, especially some air inclusions appear, and the signal intensity varies by about ±3%. So we can conclude that the following relaxometric investigations average over these mm-scale inhomogeneities.

In order to check if the decay of the curves might be additionally affected by diffusion in magnetic field gradients according to eq.2.10, the influence of T_E on the apparent average T_2 was tested at high and low field.

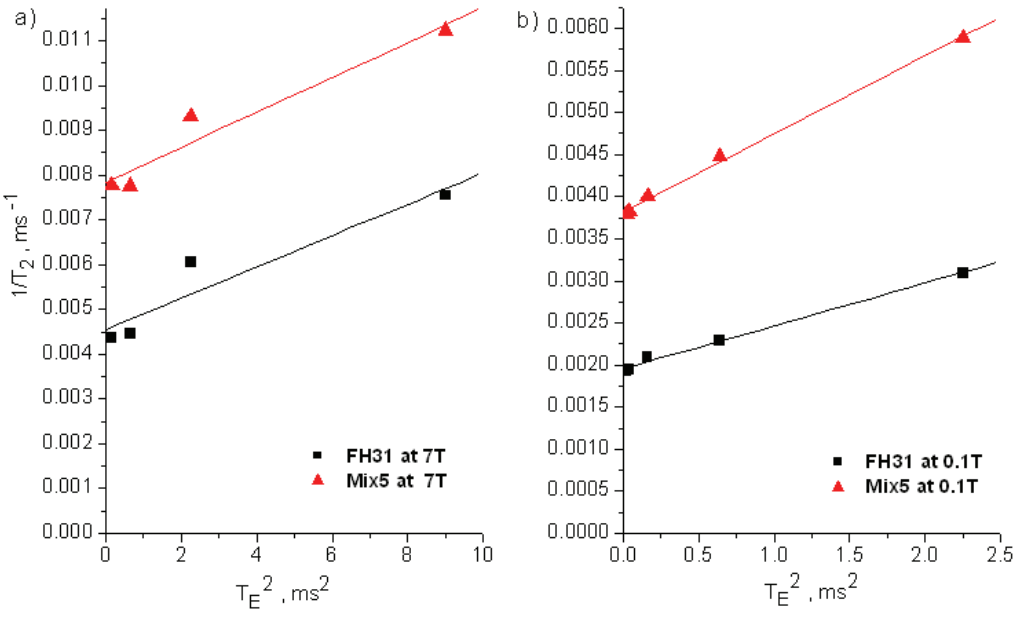

Fig.4.4.Estimation of diffusion influence: $1/T_{2,\,average}$ as a function of T_E^2 at a) 7T and b) 0.1T for two samples: FH31 saturated and Mix5 saturated. The field gradients were estimated using eq.2.11 to be 1.28 T/m for FH31 and 1.78 T/m for Mix5 in low magnetic field (right) and 1.089 T/m for FH31 and 1.13 T/m for Mix5 in high magnetic field (left)

Figure 4.4. shows that for saturated FH31 as well as for Mix5 the expected behavior described with eq.2.10 is observed, indicating that diffusion in internal magnetic field gradients accelerates T_2 relaxation at higher values of T_E. Nevertheless for lower values of T_E (0.15ms and 0.2ms in low field and 0.4ms in high field) the variations in T_2 are insignificant. Therefore, T_E was set to 0.2ms (the smallest echo times which do not produce truncated information) for low field measurements and 0.4ms in high field measurements, assuming that $1/T_2$ data obtained with this setting are very close to those obtained with $T_E = 0$ so that the influence of diffusion in residual field gradients is minimal and can be neglected for further evaluation. This is in agreement with those of *Keating and Knight* [2007], who found no significant contribution of diffusional relaxation rates for several fine sands. It should be noted that with decreasing water content larger deviations occur.

Figure 4.5. shows four exemplary CPMG relaxation curves of saturated samples FH31, Mix5, Mix10 and Mix15, measured in high and low field (with $T_E = 0.4$ms for $B_0 = 7$T and $T_E = 0.2$ms for $B_0 = 0.1$T). Generally, the relaxation curves decay faster with increasing clay content at both field strengths. The most obvious difference is that at low field the relaxation decays are slower compared to high field.

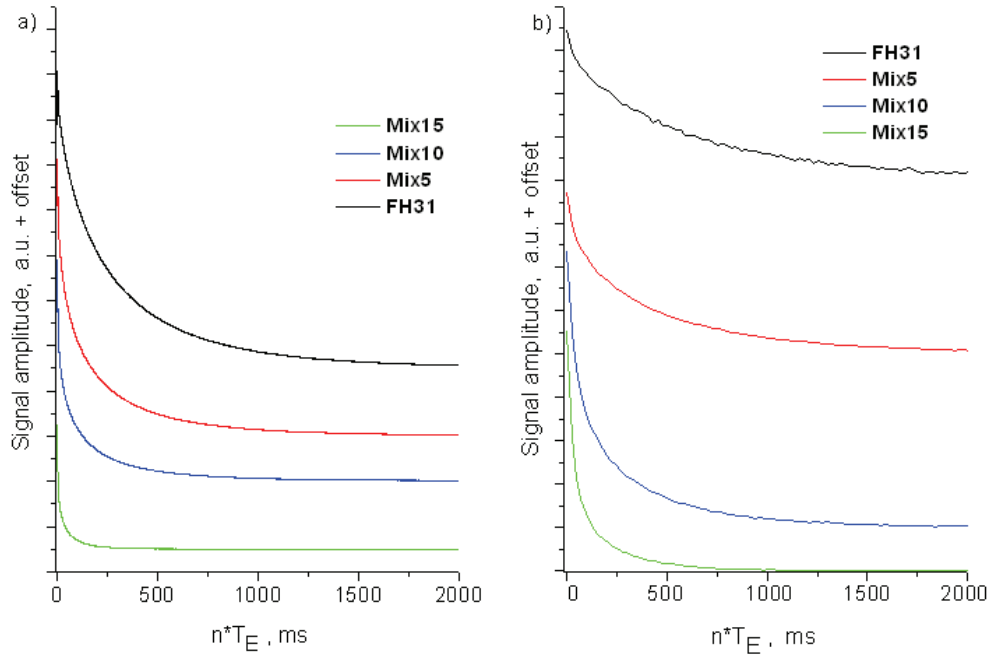

Fig.4.5.CPMG relaxation curves for all saturated samples at a) high field: $B_0 = 7$ T (300MHz), $T_E = 0.4$ms and b) low field: $B_0 = 0.1$T (4.2MHz), $T_E = 0.2$ms. For better inspection the curves are offset along the ordinate

All curves were analyzed using inverse Laplace transformation according to eq.2.7. Figure 4.6. shows the relaxation time distribution functions as obtained by inverse Laplace transformation of the curves in Fig.4.5. using the program of *Song et al.*, [2002]. At both fields strengths bimodal distributions are observed for FH31 and all sand/clay mixtures although the fast mode is hardly resolved for FH31 and Mix5. Nevertheless, these patterns allow one to distinguish between a slow mode at about 300ms and a fast mode at about 20ms for FH31 at 7T (300MHz, Fig.4.6.a). With increasing clay content the fast mode becomes more pronounced and both modes are shifted toward smaller T_2 values. The explanation for this pattern is the reduction of the pore sizes as a consequence of adding clay to the sand. The bimodality at higher clay contents reflects most probably the existence of clay aggregates (relaxation time around 30ms) beneath larger pores like in pure sand, i.e. the clay tends to aggregate around the sand grains resulting in the redistribution of pore size classes. A complete filling of the pores has not been observed, since the slow mode principally persists. The fact that the overall maximum water content (θ_{max}, Table 4.2) does not decrease with increasing clay content, but in contrary slightly increases supports this interpretation, that the clay particles do not fill completely the present pores.

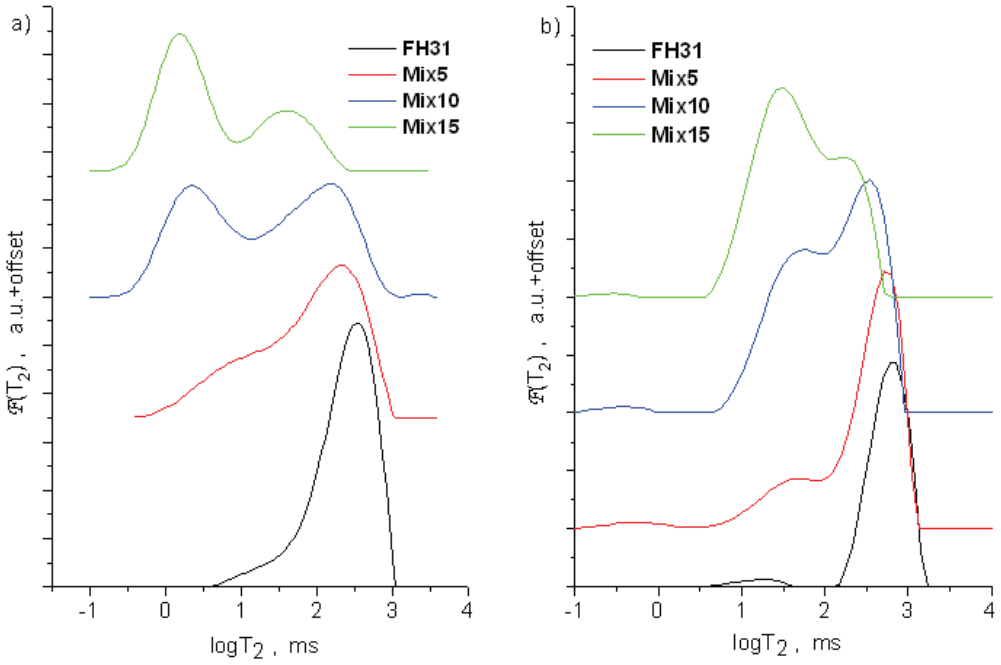

Fig.4.6.Distribution function $\mathcal{F}(T_2)$ for saturated samples at a) B_0 = 7T and b) B_0 = 0.1T Data fitted according to eq.2.7 using 100 exponentially spaced T_2 values

At 0.1T (4.2MHz, Fig.4.6.b), FH31 is characterized by a dominant slow mode at 550ms and a small, fast mode at 15ms, which contributes less then 2% to the total area. Bimodal behavior is observed for all clay mixtures; however, both modes overlap significantly and are not as well resolved as for high field. This can be due to the regularization procedure as well as to the detection of water from pore throats (connections between pores), water that in high field relaxes to fast to be detected. Again the relaxation times are shifted, for instance for Mix15 the peaks are shifted to 200ms (slow mode) and 30ms (fast mode). The same trend is observed as at high field, with an increase of the fast modes on the expense of the slow ones due to the reduction of the pore sizes by adding clay to the sand.

4.2.2 Relaxivity as a function of water content

One of the main motivations of this research is the detection of the dependence of the relaxation parameters on the water content in different magnetic field strengths. Therefore, the measurements were repeated for all samples at different degrees of water saturation. Figure 4.7. shows the obtained distribution functions at 7T and 0.1T for FH31 at different water contents, θ.

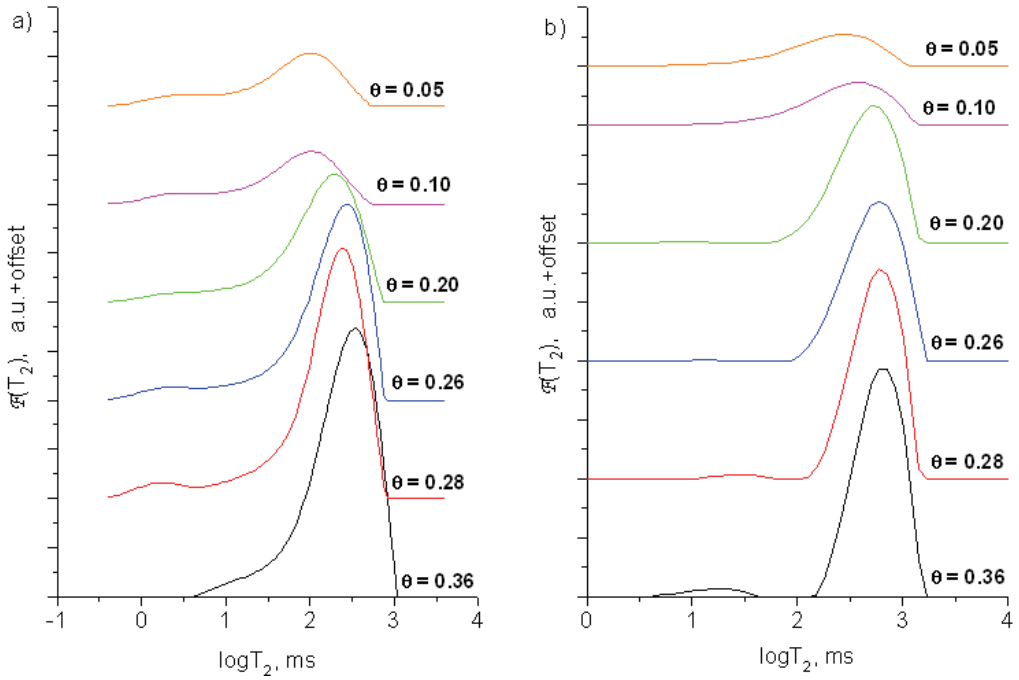

Fig.4.7.Distribution function $\mathcal{F}(T_2)$ for sample FH31 at different water contents. a) B_0 = 7T and b) B_0 = 0.1T. Data fitted according to eq.2.7 using 100 exponentially spaced T_2 values

For high field (Fig.4.7.a), the distribution is relatively broad and has a bimodal trend with unresolved peaks (shoulder) for higher water contents which broadens with decreasing saturation. It should be noted that the broadening of the distribution with decreasing saturation can also be an effect of the regularization procedure since the first term of the regularization condition (eq.2.9) is increased by the noise level and the loss of signal amplitude due to the loss of water leads to a smaller signal-to-noise-ratio. The total area of the distribution function is also decreasing due to the increasing of desaturation.

The mean relaxation time shifts from 300ms at highest water contents to 30ms for the lowest. For low field (Fig.4.7.b), the distribution functions of FH31 are monomodal with a negligible contribution of a fast mode. This trend is observed only for higher saturations. The relaxation accelerates from $T_{2,\ \text{average}}$ = 550ms to 250ms with decreasing water contents ranging from θ = 0.36 to 0.05 cm^3/cm^3. The distribution functions for Mix5 are bimodal (Fig. 4.8.) in both magnetic fields. With decreasing water saturation the slow and fast mode decreases by a factor of 2 at both field strengths. It is obvious that the relative contribution of the fast mode increases at the expense of the slow mode. This pattern can be explained by the water retention of the porous material where the water loss will begin in the largest pores and successively smaller pores will be desaturated.

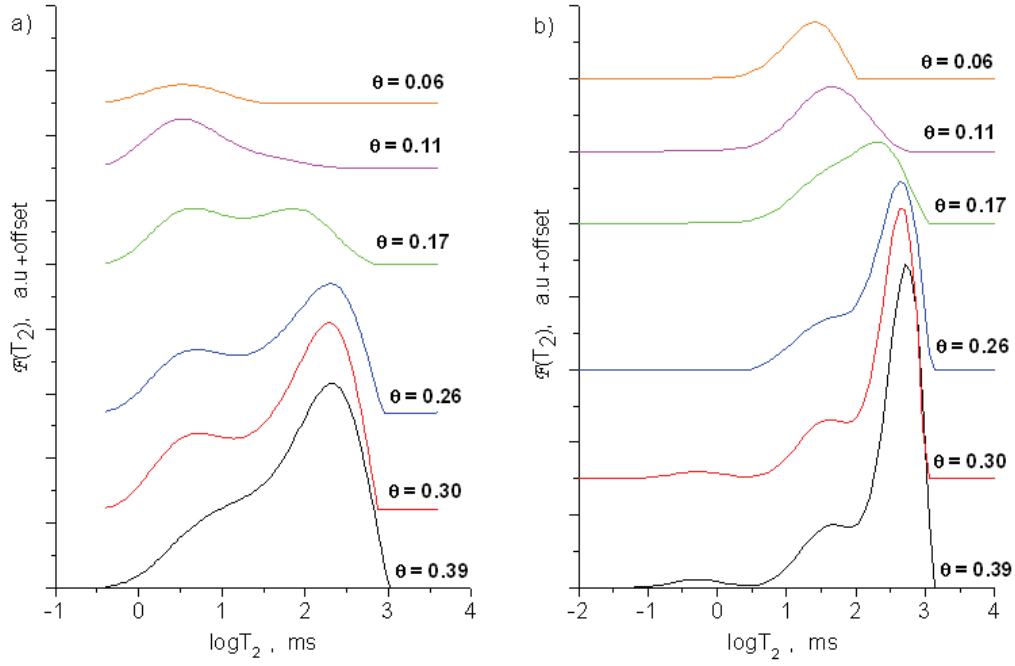

Fig.4.8.Distribution function $\mathcal{F}(T_2)$ for sample Mix5 at different water contents. a) B_0 = 7T and b) B_0 = 0.1T. Data fitted according to eq.2.7 using 100 exponentially spaced T_2 values

Finally, water will remain in the finest pores only. This results in more frequent wall collisions and therefore shorter relaxation times. As a consequence, at very low water content only the fast mode remains. *Bird et al.* [2005] attribute those effects also to a redistribution of water within the soil due to entrapped air within smaller intra-aggregate pores. However, this effect should be taken into account only for very low saturations since at higher saturation the evaporation model (Fig.4.10) shows an even distribution of the water within the sample. This trend is reproducible for all clay mixtures (see Annex 3).

The remaining question is to what extent the extrapolated signal amplitude is proportional to the water content as suggested by eq.2.5. The total signal amplitudes for all samples in high and low field are displayed in Fig.4.9. as function of the water content. In general, at high field (Fig.4.9.a) the relation shows a stronger scattering and clear dependence on the clay content for all samples. With increasing clay content the deviation from linear proportionality is more pronounced.

One possible explanation for this non-linearity between signal amplitude and integral water content, which was determined gravimetrically, can be the non-uniformity of the water content within the sample due to evaporation at the surface.

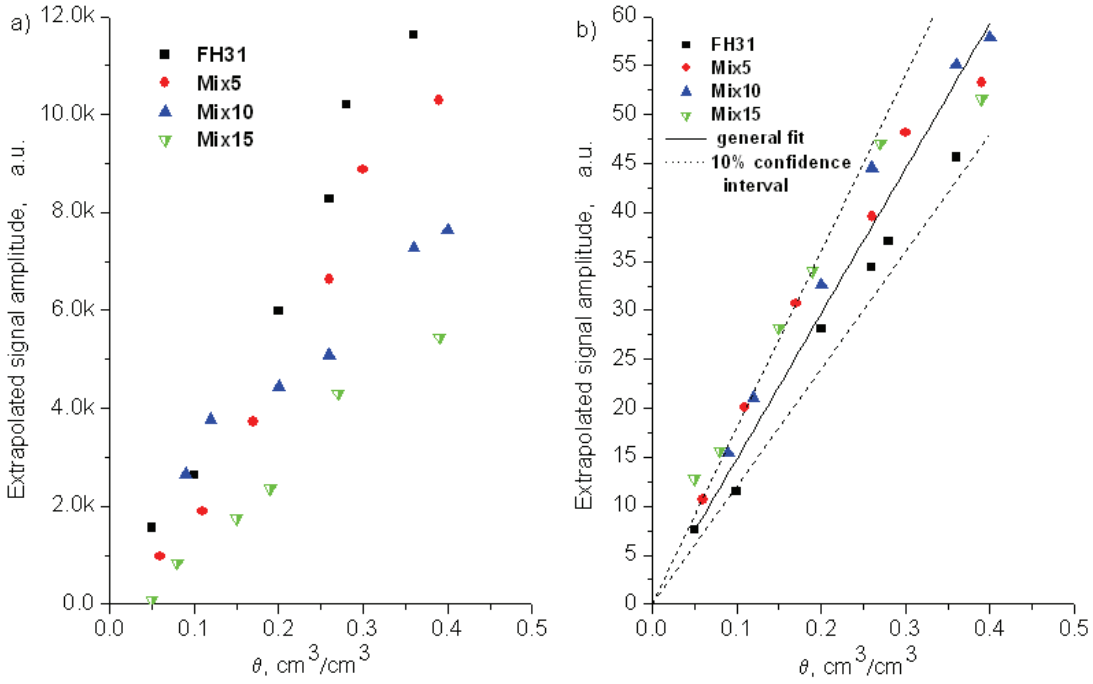

Fig.4.9.Extrapolated signal amplitudes at different mean volumetric water contents for all samples. a) B_0 = 7T and b) B_0 = 0.1T

To check this hypothesis numerical simulations have been performed to check whether large water content gradients will occur during evaporation. Therefore, the simulations were carried out analogously to the sample preparation. The corresponding actual water contents for the four samples over depth are plotted in Fig.4.10. From these results one may conclude that the water content does not change much with depth for each evaporation step. Only the final step, with smallest water content indicates a steep decline close to the soil surface which is most intense for the mixture with the largest clay fraction (Mix15).

A further reason for the observed non-linearity between signal amplitude and the water content (Fig.4.9.a) might be the loss of signal during the first T_E period, which is 0.4ms at high field, i.e. fast relaxing components are present. Shorter echo times were technically not possible, so this effect could not be corrected for with the fitting procedure. The consequence is a CPMG echo train amplitude close to zero at non-zero water content, in other words, a part of the water present in the Mix15 sample at $\theta = 0.05$ relaxes faster than about 1ms.

In contrast to the results at high field, the measurements at low field show a clear linear relation between the extrapolated signal amplitude and the water contents for all samples (Fig. 4.9.b). The observed relation has been quantified for all sampled values using linear regression with $M = c\,\theta$ with c as the slope and M as signal amplitude resulting in a coefficient of determination of $R^2 = 0.91$. Because these values were determined by extrapolation to time = 0 it is difficult to obtain a realistic error for them. Therefore, the quality of the experiment was estimated using a 10% confidence interval as displayed in Fig. 4.9.b which contain more then 95% of the measured values. Hence, an error of 10% seems to be a realistic estimate for the determination of water content from low field NMR measurements. With respect to magnetic resonance imaging (MRI) these results suggest that in principle a single point calibration will be sufficient to determine water content of soil; however the underlying linear relation must first be confirmed for more realistic samples.

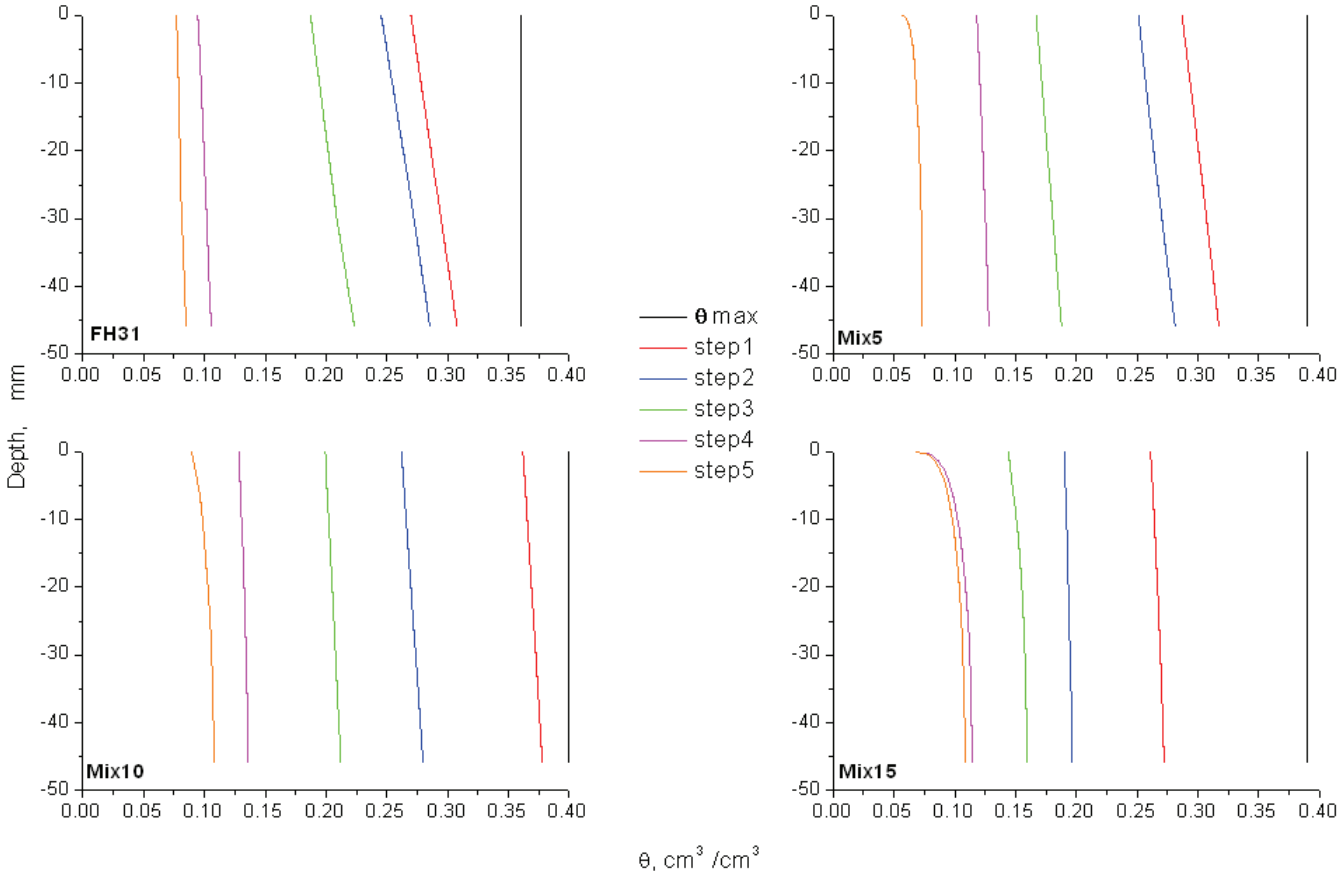

Fig. 4.10.Hydrus-1D model results for the actual water content (cm^3/cm^3) with depth after five evaporation steps for all samples. The soil surface is at depth = 0

4.3 Conclusions

We have investigated the transversal relaxivity of water in medium sand and different sand/kaolin mixtures at high (7T) and low (0.1T) magnetic fields, by means of the CPMG pulse sequence as a function of water contents and composition. The data were analyzed by inverse Laplace transformation. Before starting the conclusions, the major trends observed at both field strengths are summarized:

i) The dispersion of the relaxation times, i.e. their dependence on the main magnetic field is similarly weak, e.g. for medium sand a factor of about 2 is found while the field strength increases by a factor of 70; for Mix5 the slow and fast modes are accelerated by factors of 2 and 5, respectively, while the magnetic field strength increases from 0.l to 7T. The acceleration due to internal magnetic field gradients is most probably not the reason for this dispersion since the gradient strengths are comparable (values are presented in the caption of Fig.4.4.).

ii) Pure sand: At 7T a broad bimodal distribution function was observed. The main mode (≈ 95% of the amplitude) is accompanied by a broad shoulder at shorter T_2. Both modes shift to faster relaxation with decreasing water content.

iii) Pure sand: At 0.1T a medium broad (one order of magnitude) bimodal distribution function was observed. At saturated state a fast mode which contributes less then 2 % to the total area is present. With decreasing water content the main mode shifts slightly to faster relaxation while the fast mode remains approximately at constant relaxation time.

iv) Mixtures: At 7T bimodal broad distribution functions ranging over three orders of magnitude have been observed, which shift to shorter relaxation times with increasing content of kaolin by one order of magnitude between 5% and 15% kaolin.

v) Mixtures: At 0.1T also bimodal distributions functions occur, with a smaller width than at high field. The shift to shorter relaxation times is much less pronounced: a factor of three for the slow mode and no shift of the fast mode.

vi) Absolute amplitudes: At low field all measured amplitudes of the relaxation curve are proportional to the absolute water content. At high field the relation shows a stronger scattering of the extrapolated amplitudes with water contents and their slopes decrease with increasing kaolin content in the sample.

These measurements show conclusively that the transverse relaxation time, T_2, is affected by both the variation of clay content and the variation of water content in the samples.

At low magnetic field, by increasing the clay content the dominant effect is an increase of the total signal amplitude and relaxation rate. This phenomenon is strongly related to the porosity of the samples and the pore size distribution. By increasing the clay content in the sample the relaxation time distribution functions are shifted towards smaller values due to redistribution of pore size classes. Since the bulk relaxation rate is not significantly enhanced, the apparent relaxation recorded at sufficiently short echo time so that the diffusion influence can be neglected, is best discussed in terms of the surface relaxation according to eq.2.10. ρ_2 is a factor that comprises several properties of the surface: surface concentration of paramagnetic centers, diffusivity at the surface, local magnetic field gradients around these centers, local topology of the surface etc. For natural systems these factors are hard to control, so the most convenient (and most taken) way is to define an average value of ρ_2 in order to derive the pore size distribution (see further research presented in chapter 5). Overlapping and unresolved distribution functions are mainly due to the detection of water from pore throats water that in high field relaxes to fast to be detected.

At high field, some fractions of water located in very fine pores might have relaxed during the first echo period and this information is lost resulting in a decrease of the signal amplitude with increasing clay content,. The same pattern observed as at low field, e.g. shifting of the relaxation time distribution functions toward smaller T_2 values with increasing clay content, strengthen the assumption of the reduction in pore sizes as a consequence of adding clay to the sand when the diffusion in internal magnetic field gradients is neglected. With increasing clay content we find higher percentage of water into narrow confinements.

With decreasing water content, in both magnetic fields, a shift of the apparent relaxation time to smaller values is observed; this is expected, if again the surface term in eq.2.10 dominates transversal relaxivity: $1/T_2$ scales approximately with S/V which is inverse proportional to the degree of saturation θ.

5. Determination of the pore size distribution and hydraulic properties using NMR relaxometry

Known pore size distributions can be directly linked to the water retention characteristic which is essential for the prognosis of water and solute movement through the material. In the second part of this study, it was evaluated the feasibility to use Nuclear Magnetic Resonance (NMR) relaxometry measurements for the characterization of pore size distribution in four porous samples with different texture and composition. Therefore, NMR T_2 and T_1 relaxation measurements at 6.47MHz were carried out for three model samples (medium sand; fine sand; and a homogenous sand / kaolin clay mixture) and a natural soil. To quantify the goodness of the approach, the NMR measurements were compared in terms of cumulated pore size distribution functions and mean pore diameter with the two classical techniques based on water retention and mercury porosimetry measurements. Based on these comparison further study was performed to evaluate the influence of the variations observed in the pore diameter distributions on the hydraulic properties of the samples: θ_s, α, and n.

5.1 Materials and methods

5.1.1 Soil Samples

Four different soil samples where used in the study, whereby three samples are artificial substrates: medium sand (FH31) with a grain size distribution between 0.72 mm and 0.18 mm, Milisil fine sand (W3), and a mixture (Mix8) of FH31 and 8% mass percentage of kaolin clay (FH31 and W3 were provided by Quarzwerke Frechen, Germany, kaolin clay from Sigma-Aldrich, Germany). Additionally, a natural soil from Merzenhausen, Germany (MZ) (50°54´N, 6°24´E) was used. The Merzenhausen soil is characterized as an Orthic Luvisol, with 80%, mass percent silt and 18%, mass percent, clay [*Kasteel et al.*, 2007]. More information upon the materials used can be found in Annex 2. For NMR measurements and the determination of the water retention curve (except the MZ sample for which the retention curve was determined for undisturbed soil column), the samples were homogenized, sieved, and packed at the same packing density. For mercury intrusion porosimetry, both sieved and conglomerate structures have been used.

5.1.2 NMR setup

In our study, H-NMR- relaxometry measurements were performed on saturated samples in order to determine the transversal and longitudinal relaxation times and on the soil solutions extracted by centrifugation for the characterization of the bulk relaxation. The substrates were filled into glass tubes with an inner diameter of 24 mm and a height of 46 mm. The experiments were conducted on a Halbach magnet (Fig.5.1.) of 0.15T magnetic field strength [*Raich and Blümler*, 2004] connected to a STELAR spectrometer (Stelar, Mede, Italy).

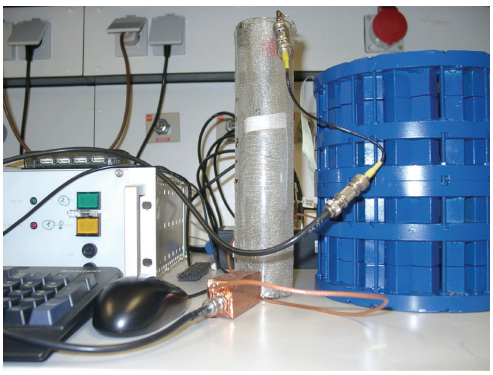

Fig.5.1.Halbach magnet of 0.15T together with RF coil and STELAR spectrometer

The resonator was a solenoid RF-coil of 4cm inner diameter and 6cm length. For the determination of T_2 relaxation time the CPMG (*Carr-Purcell-Meiboom-Gill)* pulse sequence described in 4.1.2 was employed [*Carr and Purcell*, 1954; *Meiboom and Gill*, 1958]:

$$90^\circ \text{ Rf pulse} - (T_E/2 - 180^\circ \text{ Rf pulse} - T_E/2 - \text{echo acquisition})_n$$

with n = 15000 echoes and T_E = 150µs. For the determination of T_1 relaxation time a standard inversion recovery pulse sequence was used:

$$180^\circ \text{ Rf inversion pulse} - \tau - 90^\circ \text{ Rf pulse} - \text{FID acquisition}$$

were τ was varied in 32 logarithmically spaced steps between $0.01 \cdot T_{1max}$ and $4 \cdot T_{1max}$ ms.

As stated in 2.3.2 for a porous media the dimensions of the pores are related to relaxation times by the Brownstein - Tarr equation [*Brownstein*, 1977; 1979] in which the diffusion term was neglected and only relaxation due to the surface interaction was considered. Assuming cylindrical pores with diameter D the pore size can then be calculated according to eq.2.13 by:

$$\frac{1}{T_{1,2,app}} = \frac{1}{T_{1,2bulk}} + \rho_{1,2} \cdot \frac{4}{D} \qquad (5.1)$$

In our study homogeneous distributions of the pore centres (e.g. of the surface relaxivity) and cylindrical pore geometry were assumed to provide a consistency of the assumptions when

pore diameters calculated from all methods were compared (Washburn equation applied for mercury intrusion measurements and Young-Laplace equation applied to retention function data also assume a cylindrical capillary geometry of the pores).

5.1.3 Mercury intrusion porosimetry

The mercury porosimetry method characterizes the porosity of the observed material by applying various levels of pressure to a sample immersed in mercury. Mercury intrusion porosimetry is one of only a few analytical techniques that permit an analyst to acquire data over a broad dynamic range using a single theoretical model. It is routinely applied over a capillary diameter range from 0.003µm to 360µm. Mercury porosimetry is applicable over a wide range of pore sizes, and the fundamental data it produces (the volume of mercury intruded into the sample as a function of applied pressure) is an indicative of various characteristics like pore size distribution, pore geometry, wettability, connectivity of the pore spaces, etc., and is used to reveal a variety of physical properties of the solid material itself. Detailed explanation on the characterization of materials by mercury intrusion is given by Paul Webb [*Micromeritics*, 2001].

In 1921 Washburn [*Washburn,* 1921] derived an equation that describes the equilibrium of the internal and external forces on the liquid-solid-vapour system in terms of surface tension, contact angle, and the geometry of the line of contact at the solid-liquid-vapour boundary. It states concisely that the pressure required to force a non-wetting liquid to enter a capillary of circular cross-section is inversely proportional to the diameter of the capillary and directly proportional to the surface tension of the liquid and the angle of contact with the solid surface.

$$D_i = \frac{-4 \cdot \sigma_{Hg} \cdot \cos \gamma_{Hg}}{P_i} \tag{5.2}$$

For a given liquid-solid system, the numerator of eq.5.2 is constant, providing a simple relationship of inverse proportionality between the size of the pore into which mercury can intrude and the applied intrusion pressure. In other words, mercury under external pressure P can resist entry into pores smaller than D, but cannot resist entry into pores of sizes larger than D. So, for any pressure, it can be determined which pore sizes have been invaded with mercury and which sizes have not. These values and the associated pressure (pore size) values yield a table of pore size intervals and incremental volumes associated with each interval presented as the Annex 4.

In the case been we are interested in the pore volume distribution and characterization of the pore size distribution. This is normally determined by achieving maximum pressure by a series of small pressure steps. The pressure and volume are measured after the intrusion equilibration is achieved. In the great majority of cases and in the form of Washburn's equation presented as eq.5.2, the pore is considered to be a right circular cylinder. The cumulative intrusion volume of mercury at each measured pressure is determined by subtracting the volume of mercury remaining in the stem from the original volume. For a continuous curve plot of pore volume versus size class, only a single size value is required to represent the size class. This value may be the upper or lower size boundary or some representative size between the two boundaries (the average size, for example).

The system used in our measurements is a standard porosimeter (Fig.5.2) in which the sample is placed into a container, evacuating the container to remove contaminant gases and vapours (usually water) and, while still evacuated, mercury is allowed to fill the container. This creates an environment consisting of a solid, a non-wetting liquid (mercury), and mercury vapours. Next, pressure is increased toward ambient while the volume of mercury entering larger openings in the sample bulk is monitored. A pressure between 48.26hPa and 31.7MPa was applied and this pressure will force mercury into pores between 400 and 0.05 micrometers in diameter according to Annex 4 and technical description of the instrument. The volume of mercury that intrudes into the sample due to an increase in pressure from P_i to P_{i+1} is equal to the volume of the pores in the associated size range D_i to D_{i+1}, sizes being determined by substituting pressure values into Washburn's equation (eq.5.2).

a) 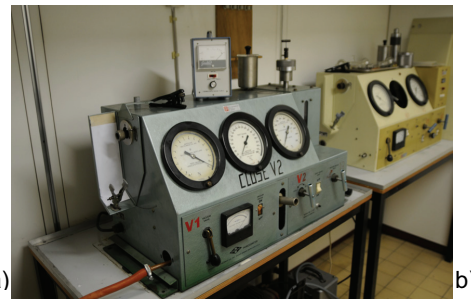 b) 

Fig.5.2. Porosimeter unit used for mercury intrusion measurements.
a) Pressure station and b) Penetrometer

5.1.4 Water retention measurements

The water retention curves were determined using standard sand bed / pressure cell or multi-step-outflow, methods based on suction and pressure application as previously described in 3.2. Only for the Mix8 sample no measured retention curve data were available, and therefore, a pedotransfer function, ROSETTA [*Schaap et al*., 2001] was used to predict the hydraulic properties. For the parameterization of the water retention curves the Mualem-van Genuchten approach [*Mualem*, 1976; *van Genuchten*, 1980] was used, whereby the effective volumetric water content S_e is defined as:

$$S_e = \frac{\theta - \theta_r}{\theta_s - \theta_r} \begin{cases} 1 & h \geq 0 \\ (1 + |\alpha h|^n)^{-m} & h < 0, \ \alpha, m > 0 \quad n > 1 \end{cases} \tag{5.3}$$

where θ_r and θ_s (cm^3/cm^3) are the residual and saturated volumetric water contents, and α (cm^{-1}), n (-), and m (-) ($m = 1\text{-}1/n$) are shape parameters. The hydraulic properties of the reference materials as well as the measurement source are summarized in Table 5.1. In general, retention curves are usually interpreted as cumulative distribution functions in comparison to pore size distribution functions which are mostly plotted as a function of frequency.

Table 5.1. Hydraulic properties for the four substrates FH31, W3, Mix8, and Merzenhausen soil (MZ). Parameters of FH31 and MZ are based on pressure plate measurements. W3 was determined using multi-step outflow (MSO) and Mix8 using ROSETTA software [*Schaap et al.*, 2001].

* for a better correlation between the measurements in the further calculations θ_r was set to 0

Sample	Method	Bulk density g/cm^3	θ_r^* cm^3/cm^3	θ_s cm^3/cm^3	α cm^{-1}	n -
FH31	pressure plates	1.58	0.020	0.384	0.0133	12.72
W3	MSO	1.42	0.058	0.333	0.0089	2.78
Mix8	Rosetta	1.45	0.061	0.410	0.0283	2.66
MZ	pressure plates	1.60	0	0.438	0.0195	1.21

Using retention characteristics the pore size distribution can be extracted for a given porous medium based on an empirical law that relates the pore suction with the effective pore radius [*D'Hollander*, 1979; *Kosugi*, 1994; 1996; *Jury and Horton*, 2004]. Assuming the pore system as a model consisting of cylindrical capillary tubes with a random distribution of radii, the capillary pressure can be related to the pore dimension according to the Young-Laplace equation:

$$h = \frac{2\sigma \cos\varphi}{rg\rho} \tag{5.4}$$

where h is the pressure head or capillary rise (m), σ is the surface tension (N/m), φ is the contact angle between liquid and solid phase, r is the pore radius (m), g is the standard gravitational acceleration (9.80665m/s^2), and ρ is the fluid density (kg/m^3).

5.2 Results and Discussions

5.2.1 NMR results

The transversal relaxation time distribution functions obtained using inverse Laplace transformation [*Song et al.*, 2002] for each of the four samples is plotted in Fig. 5.3.a). The distribution functions are mono-modal for sandy samples FH31 and W3 with an average relaxation time of 560ms for FH31 and 175ms for W3. The Mix8 and MZ samples present wide (over three orders of magnitude) bimodal T_2 relaxation distribution functions with average values of 30ms for Mix8 and 0.60ms for MZ sample. The natural soil sample MZ has a very fast relaxation in comparison to all others, where the relaxation might be enhanced by the magnetic susceptibility of some of the soil components. Fig.5.3.b) shows the longitudinal relaxation time, T_1, distribution functions for each sample.

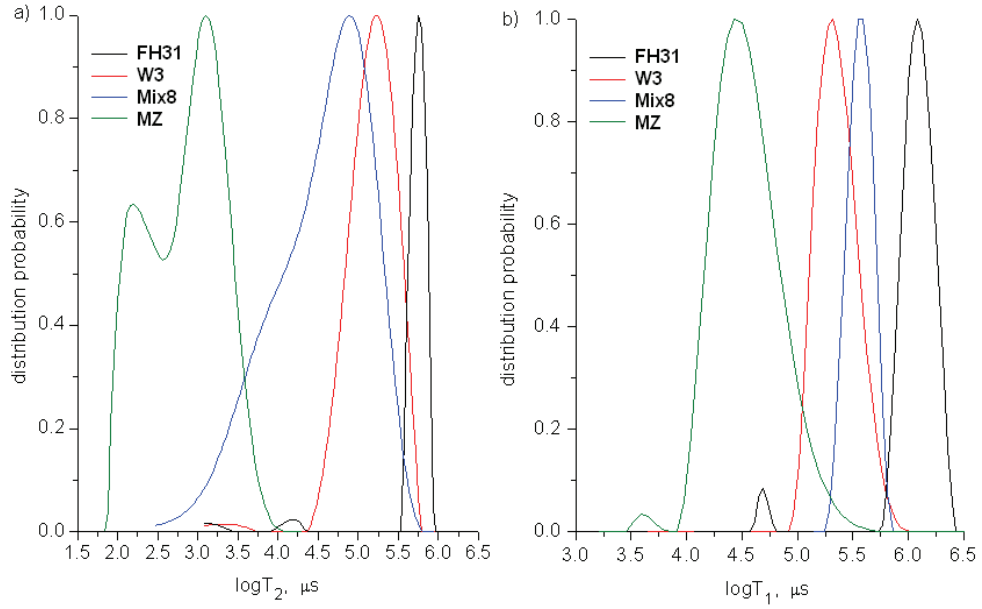

Fig.5.3. a) T_2 and b) T_1 relaxation time distribution functions for the four substrates.

The distributions can be described as mono-modal for all samples with average relaxation times of 1300ms for FH31, 200ms for W3, 400ms for Mix8, and 30ms for the MZ sample, whereas the MZ sample present a wide distribution in which the unresolved shoulder that appear in the slow relaxation time regime (150ms) may be considered as the relaxation in large pore structures.

Instead of analyzing only the classical T_1 and T_2 relaxation distribution functions as plotted in Fig.5.3., cumulative pore size distributions functions were calculated according to eq.5.1. The normalized cumulated functions are displayed in Fig.5.4. where 1 is the sum of all pore sizes equivalent to 100%. The surface relaxivity parameters $\rho_{1,2}$ were estimated as a mean value for each sample according to eq.2.13:

$$\rho_{1,2} = \frac{T_{1,2,bulk} - T_{1,2,app}}{T_{1,2,bulk} \cdot T_{1,2,app}} \cdot \left(\frac{S}{V}\right)^{-1} \tag{5.5}$$

in which the surface to volume ratio (S/V) value was supplied from BET measurements and the bulk relaxation times were measured for each soil solution extracted from the samples by centrifugation. The average surface relaxivity parameters ρ_1 and ρ_2, bulk relaxation times, S/V ratio, and the obtained average pore diameters for all samples are listed in Table 5.2.

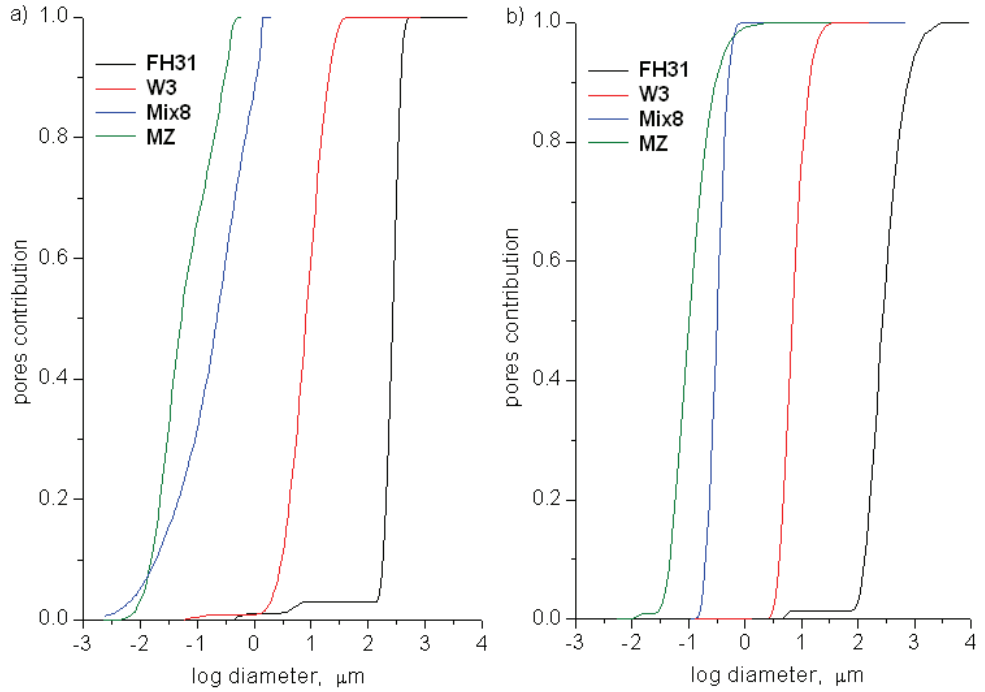

Fig.5.4.Cumulative pore size distribution calculated according to eq.5.1. a) PSD-T_2 and b) PSD- T_1 for the four substrates

Table 5.2. Calculated surface relaxivity parameters and average pore diameters from NMR relaxation measurements.

Sample	ρ_2, surface relaxivity μm/ms	ρ_1, surface relaxivity μm/ms	$T_{2,bulk}$ ms	$T_{1,bulk}$ ms	Specific area cm^2/g	S/V cm^{-1}	D_{2av} μm	D_{1av} μm
FH31	$96 \cdot 10^{-3}$	$30 \cdot 10^{-3}$	2280	2786	68	108	260	260
W3	$12 \cdot 10^{-3}$	$8 \cdot 10^{-3}$	1683	2279	3600	5112	8	7
Mix8	$2 \cdot 10^{-3}$	$0.2 \cdot 10^{-3}$	1012	1469	15950	23128	0.2	0.3
MZ	$7 \cdot 10^{-3}$	$0.7 \cdot 10^{-3}$	578	787	96400	154304	0.05	0.1

In general, the pore size distributions obtained from T_2 measurements (PSD-T_2), Fig.5.4.a, indicate a narrow distribution of pores for the sandy samples FH31 and W3 with values ranging between 250 - 500μm for FH31 and between 1.5 - 30μm for W3. A larger spectrum of pore sizes was obtained for Mix8 and MZ samples with values ranging from 0.002μm to 2μm for Mix8 and 0.002 to 0.5μm for MZ, which are a result of the mix of finer and coarser grains within the samples. For rocks and soils the ρ_2/ρ_1 ratio, which generally is equal with T_1/T_2, has values between 1 and 4 ($1< T_1/T_2 <3$) [*Kleinberg,* 1999 *in PO-Z. Wong*]. In our case ρ_2/ρ_1 ratio has been found: 3.2 for FH31; 1.5 for W3; 10 for Mix8 and 10 for MZ sample. For the sample FH31 even if the ρ_2/ρ_1 ratio has a reasonable value, 3.2, the surface relaxivity parameter, ρ_2, is quite large. This could point to an error in estimating the S/V ratio. Since for this medium sand was impossible to determine the specific surface using BET (the specific area is to small for the possibilities of the BET technique) its value used in the calculation of S/V was provided by the producer with no other specifications. The odd ρ_2/ρ_1 value for Mix8 and MZ sample might be due to the diffusion in internal magnetic field gradients been well known that the diffusion will affect the T_2 distribution and diffusion effects are enhanced in fine grain materials, [*Kleinberg,* 1999 *in PO-Z. Wong*]. Therefore, the influence of diffusion was checked for the two fine samples Mix8 and MZ by varying the echo spacing in the CPMG train and observing the shift of the distribution functions. For the Mix8 sample weak acceleration due to diffusion in internal gradients was observed for low T_E values (80, 100, 150 and 250μs). This is sustained also by a previous study [*Stingaciu et al*., 2009] presented in chapter 4 who showed that for 0.1T magnetic field strength the choice of T_E = 150μs for a similar clay sample will produce no truncated information and will minimize the diffusion effects allowing us to further neglect the diffusion in eq.2.12.b. For the MZ sample a steeper gradient was observed; nevertheless for lower T_E values (80, 150 and 200μs) the $1/T_2$ data obtained with these settings are very close to those extrapolated to $T_E = 0$ so that

the influence of diffusion in residual field gradients is minimal and can not be the cause of the observed variations. As a result diffusion can be again neglected in further evaluation of the pore diameters. More on this matter is yet to be published in *Stingaciu et al*., [2010] accepted by Water Resources Research journal.

Figure 5.4.b shows the pore size distributions obtained from T_1 measurements (PSD-T_1). Also here it is seen the well sorted sandy materials W3 and FH31 are characterized by a narrow pore size distribution. For fine samples with medium clay content, like our Mix8 and MZ samples, it is well known the fact that BET method measures a huge surface that is rather controlled by the surface area of the clay then by the pore size. Those relaxivity parameters calculated this way will have very low values (few micrometers per second) and represent in most of the cases the relaxivity of clay-trapped water (water in the interlayer spaces of clay packets), [*Kleinberg,* 1999 *in PO-Z. Wong*], which according to published neutron diffraction measurements exchanges to surrounding bulk water in thousands of seconds [*Cebula et al*., 1980; *Adams et al*., 1979]; therefore will give no information about the pore water. On the other hand, if the clay particles disperse, the water on the surface of clay, even if exchanges efficiently with pore water, it relaxes very fast. Therefore the PSD-T_1 of such materials can be a poor estimator of the real pore size distribution.

5.2.2 Retention functions results

As already mentioned above the water retention curves and corresponding hydraulic parameters for the four samples are based on different sources such as multistep outflow (MSO) (W3), pressure cells (FH31 and MZ), and the use of a pedotransfer function (Mix8). The measured hydraulic properties of the samples are listed in Table 5.1 and the retention curves are plotted in Fig.5.5.a). Since the retention curves are also plotted as cumulative functions, a direct comparison of the NMR measurements with water retention functions is possible. Nevertheless, pressure head as plotted in the abscissa has to be transformed also into pore size diameter using the Young-Laplace equation (eq.5.4). Additionally, the ordinate has to be normalized to 1 (100 %) which equals full saturation θ_s. The pore size distributions obtained (PSD-pF) are displayed in Fig.5.5.b). It can be easily seen that the pore sizes are narrowly distributed for the well sorted sandy samples FH31 and W3. In contrast Mix8 and MZ indicate a wider pore spectrum. From these curves the mean pore size diameter can be easily estimated. One obtains for the FH31, W3, Mix8, and MZ mean pore size diameters of 38.90, 20.41, 0.64, and 0.25μm, respectively.

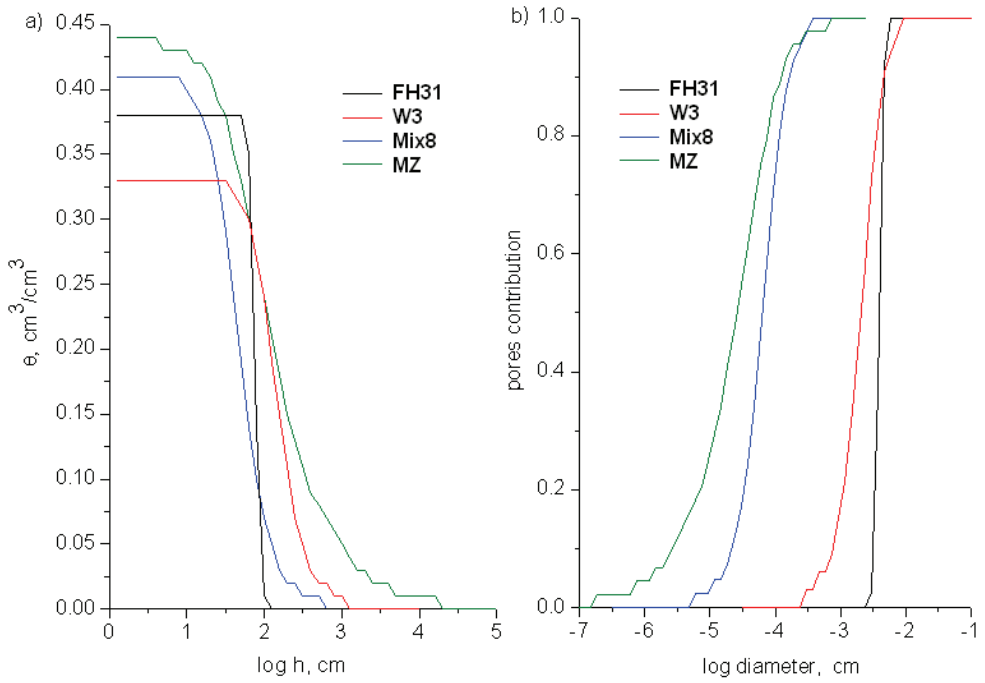

Fig.5.5.a) Water retention curves b) Normalized pore size diameter functions

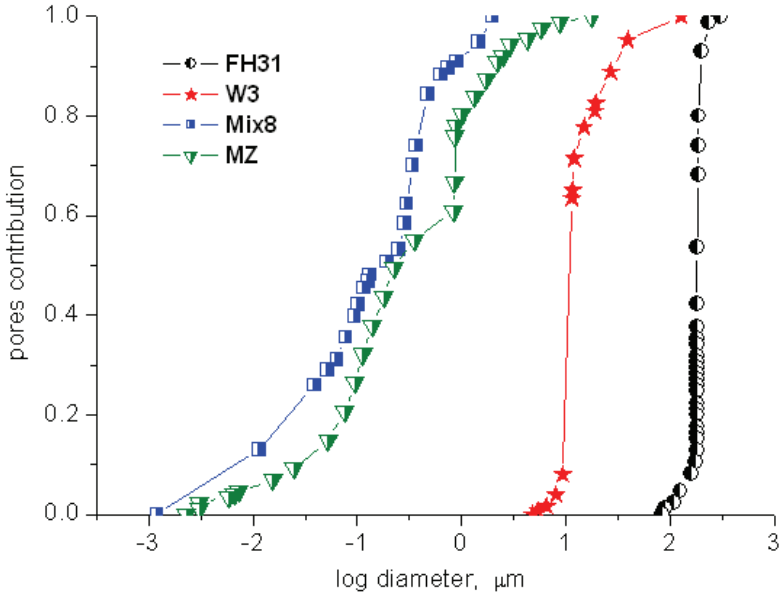

Fig.5.6.Cumulative pore size distribution based on mercury intrusion (PSD-Hg)

5.2.3 Mercury intrusion results

The pore size distribution from mercury intrusion measurements (PSD-Hg) were also obtained as cumulative functions in which the equivalent pore diameter was calculated according to eq.5.2 from experimental data collected for various numbers of mercury pressure steps. The cumulative pore size distribution functions presented in Fig.5.6 show a mono-modal distribution of pores for samples FH31 and W3 with average values of the pore diameter of 178µm for FH31 and 10µm for W3. These distributions indicate that more than 80% of the total volume corresponds to pores with a diameter smaller than 180µm in the case of FH31 sample and less than 18µm in the case of W3. The pore diameter distributions for MZ and Mix8 samples show wide multimodal distributions with average values of 0.20µm for MZ and 0.1µm for Mix8, respectively. Nevertheless, 80% of the pore volume of Mix8 is below 0.40 µm and 80% of MZ are below 3µm.

5.2.4 Comparison of the different measurements

For a better comparison of all three methods used for PSD determination, the calculated average pore diameters are presented in Table 5.3. together with some assumed uncertainty estimated from various sources as follows: i) for the NMR derived average diameter errors in the estimation were assumed to be in a 10% interval as previously shown in Fig.4.9. chapter 4.2.2; ii) for the retention function derived diameter estimation errors were assumed to be in a 2.5% interval as *Scharnagl*, [2006] showed in his diploma thesis (the estimated hydraulic properties for three W3 sand samples were deviating from each other in this interval range); iii) lacking a realistic experimental estimation of the errors that can occur from Hg intrusion measurements, the errors were assumed to be maximal, e.g. 50%, as a technical note from Micromeritics company [*Micromeritics*, 2010] suggests (see later in the chapter). The average pore diameters obtained from all measurements are the same order of magnitude for each of the four samples used for investigation. Nevertheless, large differences can be observed for mean pore diameter obtained from pF function in comparison with the other measurement for the well sorted sandy samples FH31 and W3. On the other hand, the MZ and Mix8 average diameters obtained from NMR relaxation measurements and mercury intrusion are slightly smaller compared to the retention curve (pF) derived diameters. An attempt to explain possible reasons for this difference will be given below. To gain a better understanding of the mismatch observed in the mean pore size diameter we displayed the cumulative PSD functions from all measurements in Fig.5.7.

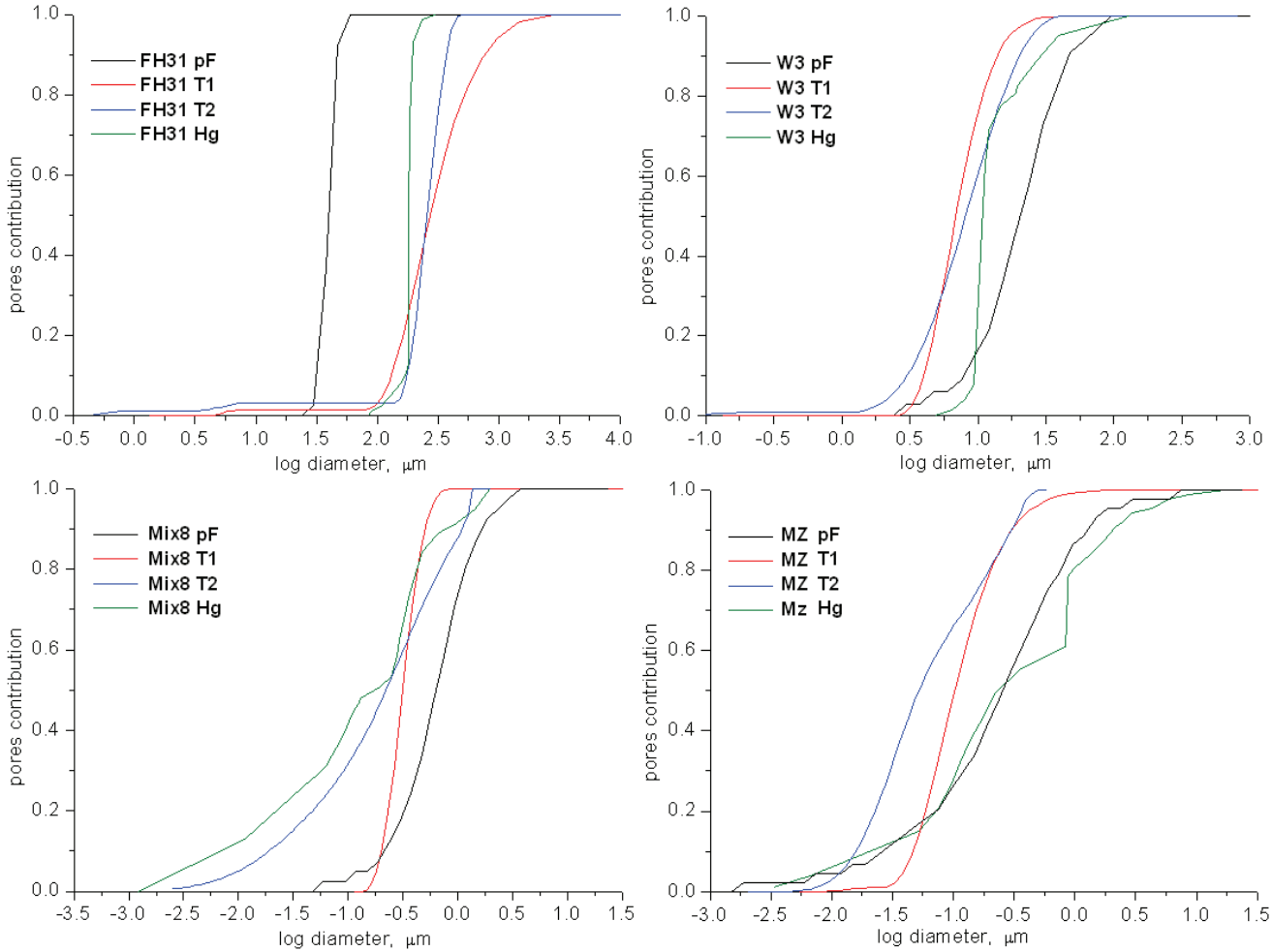

Fig.5.7.Cumulative pore size distribution (PSD) functions for all measurements and for all four samples.
Note that the abscissas are not in the same range for all plots.

In the following, the discussion of the obtained results is made as a comparison between methods with respect to the type of sample used for investigation.

Table 5.3. Average pore diameter for all samples calculated according to eq.5.1 for T_1 and T_2 - NMR relaxation measurements; eq.5.2 for Hg intrusion and eq.5.4 for water retention function.

Sample	D_{av}- Hg μm	D_{av}-T_2 μm	D_{av}- T_1 μm	D_{av}-pF μm
FH31	170 ± 85	260 ± 26	260 ± 26	39 ± 0.9
W3	10 ± 5	8 ± 0.8	7 ± 0.7	20 ± 0.5
Mix8	0.2 ± 0.1	0.2 ± 0.02	0.3 ± 0.03	0.6 ± 0.01
MZ	0.2 ± 0.1	0.05 ± 0.005	0.10 ± 0.01	0.2 ± 0.005

The NMR T_1 and T_2 relaxation measurements provide nearly identical distribution of the pore diameters for all samples. In all cases PSD-T_2 measures slightly smaller pore values compared to PSD-T_1, whereby the larger difference were observed for Mix8 and MZ samples. On the other hand, it is observable that the pore size distribution functions from T_1 and T_2 measurements cross each other at a certain point so their centroids coincide systematically due to the ρ_2 and ρ_1 constants. The less steep function of T_2 indicates not only a systematical overestimation of smaller pores by T_2 but also an overestimation of larger pores. These differences can be, on one side, due to the fact that relaxation in inhomogeneous fields leads to a signal decay that is in general non-exponential with an initial decay rate that is a weighted sum of T_1 and T_2 relaxation times as *Hürlimann and Griffin*, [1999] and *Chelcea et al*., [2009] suggested. Nevertheless, since macroscopic (centimeter scale) magnetic field gradients are unlikely to be present in a Halbach magnet and the magnetic field gradients are more likely on the grain scale, the overall variation of B_0 and B_1 field are not large enough to produce the effect described by those authors. On the other side, the large T_1 / T_2 ratio observed for the fine samples Mix8 and MZ can be due to diffusion in internal magnetic field gradients. It is well known that the presence of diffusion influence the T_2 relaxation and according to eq.2.12b will shift the pore size distribution function to smaller, unrealistic values of the pore diameter. Checking the diffusion induced by internal field gradients for the two fine samples that are more susceptible to be influenced by diffusion shows that for both, the Mix8 and MZ samples minimum diffusion influence was observed for our specific echo time [*Stingaciu et*

al., 2010]. Therefore, we can conclude that the small observed deviations come from inevitable small errors in the transformation of relaxation distribution functions in PSD cumulative functions. Moreover these samples present medium clay content and, as stated above, BET method measures a huge surface that is rather controlled by the surface area of the clay then by the pore size; therefore T_1 measurements for these types of samples give almost no information about the pore water (see chapter 5.2.1).

Comparison of the NMR pore size distribution with the pore size distribution function obtained from mercury intrusion (PSD-Hg) shows a similar shape for FH31, W3, and Mix8. Only for the natural soil of Merzenhausen (MZ sample) larger differences are observable, whereby the NMR based pore size distributions are shifted to smaller pore sizes. The Hg-intrusion measurements provide values of the pore diameters very close to the NMR measurements for sandy samples FH31 and W3 most probably due to the fact that these samples have been used as sieved material packed at the same packing density for both methods. Nevertheless, for loose materials like sand, the mercury intrusion method is quite limited by the pressure application. Micromeritics company [*Micromeritics*, 2010] gives an example about the errors that can be made in estimation of pore diameter by Hg intrusion:

''In the assumption that pores of 360μm or larger can be filled with mercury intrusion at a contact angle of 135^{o}, this claim implies that the sample is located in a volume of the sample cup (penetrometer) that is less than 3mm below the top of the sample cup (the top surface of the mercury, see Fig.5.8.). Otherwise some quantity of the 360μm pores will already be filled and their volumes accounted for during the next pressure step when the remaining pores of 360μm are filled. The result will be an underestimation of pore volume for the given size class. As an example of the error this potentially causes, assume that 50% of the sample mass is located greater than 3mm below the top of the sample cup.

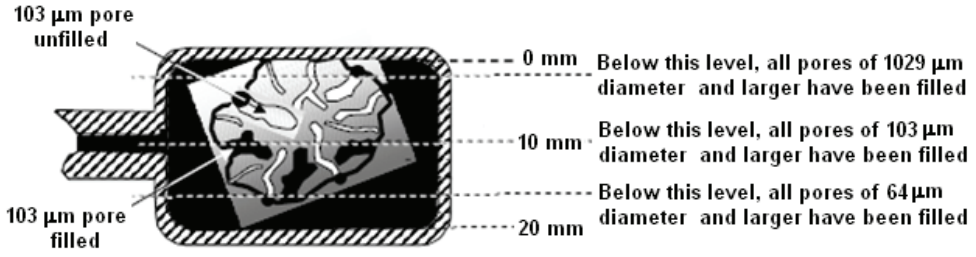

Fig.5.8.The effect of head pressure on pore filling; the pores of same size are not filled toward the top of the sample cup (penetrometer), but are filled when at deeper position (picture not to scale)

This means that 50% of all pores larger than 360μm have been filled. During the next pressure step when only pores of, say, 350 to 360μm are assumed to have been filled; the intrusion volume will be in error by about 50%. ‘’

For the sieved materials the mercury pressure cannot be extensively increased since high pressure will push the material on the sides of the sample cup, overestimating the small pores. Mix8 and MZ samples have been used as a conglomerate for determination of the PSD-Hg which allows us to apply higher mercury pressure leading to a better estimation of the fine pore contribution. Therefore, for the Mix8 sample this contribution is similar to PSD-T_2 as expected in the case of no diffusion in internal magnetic field gradients. Nevertheless, for the MZ sample differences between PSD-NMR and PSD-Hg can be observed and those differences are twofold. First, the samples for NMR measurements were sieved and packed, whereby the samples for mercury intrusion were still in natural state with smaller aggregates. Therefore, large pore structures within the aggregates can be still detectable with mercury intrusion. Secondly, it can be due to the fact that the chemical composition of the sample (e.g. the paramagnetic ions present in the natural MZ soil) might enhance the relaxation, thus preventing a reliable estimation of the NMR pore size distribution.

Comparison of NMR pore size distributions with the pore size distribution from retention curves (PSD-pF) shows a large difference for the sand sample FH31. We assume that the differences may occur from measurement errors using pressure plate method for the determination of water retention curve. It has been previously reported that pressure plates are susceptible to substantial errors at low water potential [*Campbell*, 1988; *Gee et al.*, 2002; *Cresswell et al.,* 2008]. *Bittelli and Flury* [2009] suggested that for potentials less than -10 m H_2O, pressure plates provide considerable errors that can seriously affect the fitted hydraulic functions and their parameters.

Additionally, maintaining exact pressure at low steps is crucial for probes with a steep water release curve such as our coarse sand FH31. Therefore, we tend to conclude that the pF function of this material is not reliable. The difference in the Mix8 sample is due to the fact that the retention curve was estimated based on a pedotransfer function with its known uncertainties, especially for artificial fine grained soils. Due to the fact that for the determination of the pF curve, the MZ sample has been used as an undisturbed column and due also to the similarity between the PSD-pF and PSD-Hg for this sample, (these measurements provide similar pore size distributions and the errors in pressure plates determination of the MZ pF curve can be then considered minimal), on can only speculate which of the two reasons described above influence more the observed differences between

the PSD-NMR and PSD-pF for MZ soil: the presence of the paramagnetic ions that enhanced the relaxation and shift the NMR pore size distributions to smaller values or the large pore structures within the natural aggregates that shift the PSD-pF to larger pore diameters.

Assuming a homogenous distribution of the paramagnetic centers, the surface relaxivity parameter for both T_1 and T_2 measurements will be increased, and one may obtain approximately correct pore sizes. In conclusion, the observed differences are mainly due to the large pore structures that may exist in the undisturbed soil sample. Nevertheless, a recent study [*Jaeger et al*., 2009] suggested that for natural soils the assumption of a homogeneous distribution of a mean value of the surface relaxivity parameter is somehow an ideal case, since the shape of T_2 distribution function is strongly affected by the soil texture and two surface relaxivity parameters (one for micro-pores and one for meso-pores) obtained from NMR data after calibration at different matric potentials are more convenient when transforming the relaxation time distribution in pore size distribution.

5.2.5 Hydraulic properties estimation

Finally, we analyzed the differences in the calculated retention curves for the four samples and the various measurement techniques because retention characteristics are the main input parameter for numerical simulations for the prognosis of water and solute transport. To do so, the PSD curves were transformed in pF curves based on eq.5.4. Additionally, we fitted the hydraulic parameters of the Mulaem van Genuchten parameterization [*van Genuchten*, 1980] using RETC software. Due to the fact that the residual water content, θ_r, will often be fixed to 0, only the saturated water content θ_s, and the shape parameters α and n were fitted.

The calculated retention curves are plotted in Fig.5.9. and the fitted hydraulic parameters are listed in Table 5.4. Again, we can clearly identify the large difference for retention curve of the sand sample FH31, whereby only the point of first drainage (air entrance) is delayed but the overall shape of the curve is not affected. As stated above, retention curve measurements are often biased and imprecise, especially at low pressures applied. More or less the same feature, but less pronounced, is visible for the Mix 8 sample. The curvature itself is only slightly steeper as the Hg and T_2 curve but first drainage occurs now earlier. This might be an artifact of the pedotransfer function which assumes that natural soils exhibit macro-aggregates when a certain percentage of small fractions (silt or clay) are available. The influence of soil structure can be additionally seen in the MZ sample.

Table 5.4. Soil hydraulic properties extracted using RETC software in a 95% confidence interval

Sample	Method	θ_s cm^3/cm^3	α cm^{-1}	n -
FH31	pressure plates	0.384	0.0133	12.72
	T1	0.370	0.4985	3.19
	T2	0.385	0.1582	7.28
	Hg intrusion	0.372	0.0661	12.14
W3	MSO	0.333	0.0089	2.78
	T1	0.310	0.0016	2.73
	T2	0.340	0.0027	2.93
	Hg intrusion	0.320	0.0030	4.79
Mix8	Rosetta	0.410	0.0283	2.66
	T1	0.410	0.0113	6.59
	T2	0.397	0.0266	1.56
	Hg intrusion	0.43	0.0201	1.53
MZ	pressure plates	0.438	0.0195	1.21
	T1	0.434	0.0045	2.95
	T2	0.412	0.0031	1.75
	Hg intrusion	0.430	0.0218	2.58

Largest divergence between T_2, Hg and pF curves occurs in the wet range, where the pores between macro- and micro-aggregates were drained. At larger pressures, where only soil texture is the dominant factor in water retention, less divergence is detectable.

Looking at the hydraulic parameters we see that the saturated water content, θ_s, has been estimated with less than 7 % relative error for all measurements. The α parameter shows consistent variations between different methods. Nevertheless the values are in the range of values reported in literature for similar types of samples [*Schaap et al*., 2001]. The most pronounced differences can be observed in the *n* parameter which describes the slope of the water retention curve. From Table 5.4 and Fig.5.9 it is easily observable that even for large variation of *n* (*n* ranges from 3.19 to 12.72 within FH31 sample) the slope of the calculated pF curves is nearly identical within the same sample most probably due to the insensitivity of the water retention function to high values of *n*. This leads to the conclusion that slight errors in estimation of the slope by the measurements will lead to extremely large changes in the resulting *n* parameter.

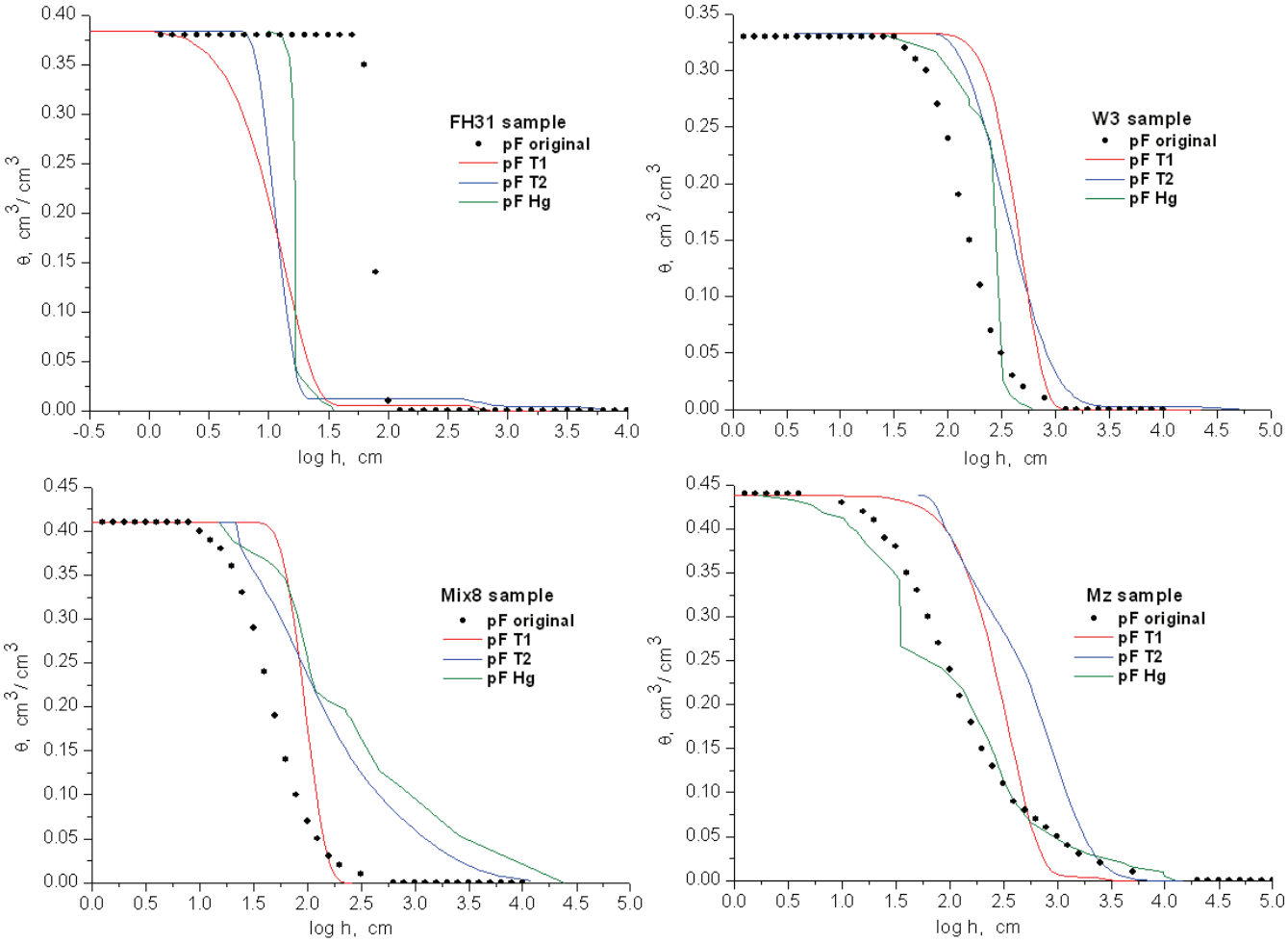

Fig.5.9.Retention curves (pF) extracted from the different pore size distributions displayed in Fig.5.7. Retention curve fitting is based on Mualem-van Genuchten parametrization [*van Genuchten*, 1980]

5.3 Conclusions

Summarizing the findings reported above we see that each measurement technique agrees to the others satisfactorily, within one order of magnitude. We also observed smaller or larger differences between the techniques irrespectively if we will look at the mean pore diameter, pore size distribution, retention curve, or hydraulic parameters. The most interesting finding is that the result from each method itself does not consequently over- or underestimates the results from the other methods. Therefore, it seems that each method within its own limitation is appropriate for determination of pore size distribution with a strong dependence on the sample characteristics.

If mercury intrusion is applied to loose materials then the mercury pressure has to be carefully limited so that the material is not pushed aside the sample walls giving unrealistic small values of the pore diameters. Hysteresis effects are always present and might have a major influence when retention data (which basically are drainage curves) are compared with mercury-intrusion data (which are mostly imbibitions curves). Even the repetition of a measurement on the same sample will not lead to the same result in retention curve (pressure plate or multistep outflow data) as *Mous*, [1993]; *Hollenbeck and Jensen*, [1998]; and *Weihermüller et al*., [2009] have shown in their work. Additionally, for both mercury intrusion and retention function measurements, the sample preparation (sieving and packing) and the maintaining of intrusion/extrusion equilibration after each pressure application are crucial factors.

The determination of pore size distribution by NMR relaxometry has its own drawbacks. Firstly, the diffusion in induced magnetic field gradients can shorten transverse relaxation times (T_2). This must be checked and can be minimized by the choice of sufficient small echo time or by measuring longitudinal relaxation (T_1). Secondly, diffusion in internal gradients may affect different modes of a multimodal relaxation times distribution function in a different way. The detailed investigation of such phenomena exceeds the frame of this work but is an important topic in future. Thirdly, one must be aware that the derivation of PSD is always a scaling procedure which requires independent determination of the average specific surface area. This is in most cases done by the BET method. Here, large clay contents of a sample can lead to huge S/V ratios and the derived surface relaxivity parameters when combined with the average relaxation rates will have very low values. The reason is that the relaxation times are controlled by the pore sizes and the surface relaxivity, but the average S/V is controlled by the internal surface area of the clay. Fourthly, the assumption over homogeneous distribution of the pores and paramagnetic centers and calculation of an average

surface relaxivity parameter, especially for a multi-modal relaxation time distribution function, leads to an overestimation of the large pores. All these issues together with the necessary simplification over the pore shape and geometry can deviate the calculated pore size distribution from the real one.

Nevertheless, our study showed that NMR relaxometry is a quick alternative for the estimation of pore size distribution, retention curve and also hydraulic properties. The major advantage of NMR in comparison with classical methods is the short measurement time which allows the analysis of large quantities of samples necessary to characterize field – or catchment scale hydraulic properties necessary for risk assessment (e.g. flood forecasting) or management (e.g. fertilization and pest control).

6. Determination of hydraulic properties using combined magnetic resonance imaging and multi-step-outflow experiments

In this part of the study it was aimed to an accurate and reliable determination of soil hydraulic properties from a procedure that involves multi-step-outflow (MSO) experiments and MRI based soil water content measurements on the laboratory scale using a heterogeneous model soil sample. First, a synthetic case study (virtual experiment) was performed in order to check the feasibility of combining MRI with MSO data. Due to the encouraging results obtained from the virtual experiment, MSO experiments were performed on a model coaxial sample filled with sand and a sandy-clay material. MRI images at 4.7T (200 MHz) were recorded during each pressure step in order to provide additional information about soil water distribution at specific locations within the soil sample. Finally, recorded cumulative outflow and water content data were used as input parameters in the inversion. For the inversion the hydrological model HYDRUS-2D was coupled with a global-optimization algorithm, namely the shuffled complex evolution (SCE-UA) algorithm of *Duan et al*., [1992] was used to overcome the problem of multiple local minima of the solution and improve the estimation of the parameters.

6.1 Materials and methods

6.1.1 Inverse simulation

By definition, inverse modeling is a general mathematical method to determine unknown parameters or state variables on the basis of observation of the system. Hence, the solution of the inverse problem is in contrast to direct or forward modeling that involves the analysis of the system response based on predefined parameters or state variable [*Hopmans and Šimůnek*, 1999; *Hopmans et al*., 2002]. In soil physics, *Zachmann et al*., [1981; 1982] were among the first who applied the inverse method to simultaneously determine the retention, $\theta(h)$, and hydraulic conductivity $K(h)$ functions from a hypothetical outflow experiment, in which an initially saturated soil column was allowed to drain by gravity. They showed that the cumulative discharge or other auxiliary data such as volumetric water content

or matric head at a fixed location can be used to generate reasonable estimates of the soil hydraulic parameters. Later, the application of the inverse modeling to one-step-outflow was introduced by *Kool et al*., [1985a and b] and *Kool and Parker* [1987], whereby a simultaneous determination of $\theta(h)$ and $K(\theta)$ was obtained by minimizing the deviation between predicted and measured outflow.

Van Dam et al., [1990] proposed the multi-step-outflow as a valid replacement for one-step-outflow experiments. Nevertheless, problem with the uniqueness of the estimated parameters have been often encountered. *Van Dam et al*., [1990] and [1992] came up with the solution to this problem by supplementing the outflow data with the soil water retention $\theta(h)$ data. Further investigation showed that the outflow data recorded from a MSO experiment can contain sufficient information for a unique estimation of the hydraulic properties [*Mous*, 1993; *Van Dam et al*., 1994]. Despite these investigations, *Eching and Hopmans*, [1993] suggested the need for additional measurements when MSO experiments are performed for a more accurate prediction. Similar to the one-step-outflow experiment these additional measurements can be tensiometric data recorded at different depth inside the sample [*Toorman et al*., 1992; *Eching and Hopmans*, 1993] or information about water content from different regions of the sample during the MSO experiment [*Weihermüller et al*., 2009].

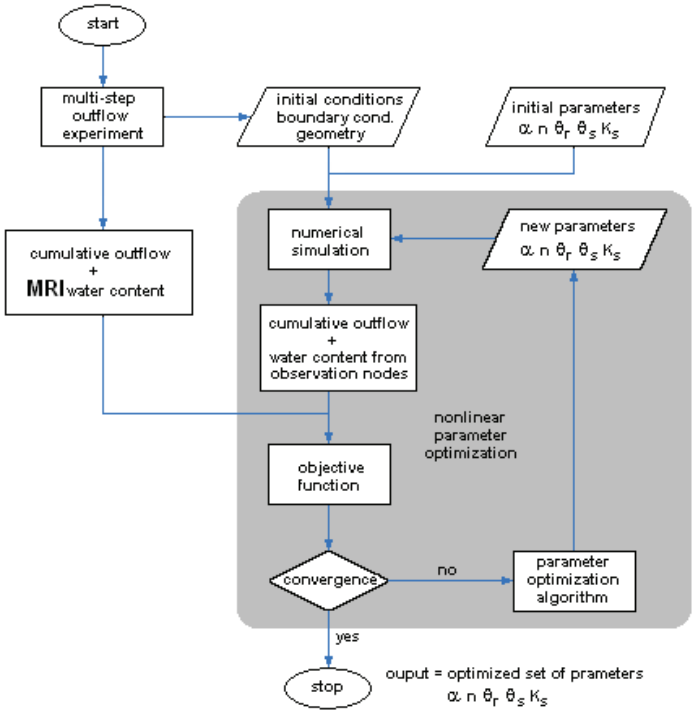

Fig.6.1. Flow chart of the inverse modeling procedure of a combined MSO – MRI experiment

Therefore, inverse modeling of MSO experiments has evolved to be a powerful tool for determining both *θ(h)* and *K(h)* from one single experiment. An illustration of the inverse method procedure adapted to our MRI experiments is shown in Fig.6.1. Following *Hopmans et al*., [2002], the method integrates three functional parts:

- the realization of an MSO experiment for which the initial and boundary conditions are known and the cumulative outflow together with MRI derived water content data are measured;
- the numerical solution of the direct problem of variably saturated flow, given a model for the soil hydraulic properties and an initial estimate of its parameters;
- nonlinear parameter optimization.

6.1.2 Parameter estimation

The soil hydraulic parameters can be estimated by numerically solving the Richards equation (eq.3.7) and iteratively minimizing the deviations between simulated and measured data. A commonly used expression for the objective function to be minimized is the approach of weighted least squares [*van Dam*, 1994]:

$$O(\mathbf{b}) = \sum_{i=1}^{N} \left\{ w_i \left[Q_m(t_i) - Q_{sim}(t_i, \mathbf{b}) \right] \right\}^2 \tag{6.1}$$

where **b** is the estimation of the parameter vector, w_i is the weighting factor (eq.6.2); N is the number of observed data in time t_i, and Q_m and Q_{sim} are the measured and simulated response data. Hereby, the weighting factor will be expressed by:

$$w_i = \frac{1}{\sigma_i^2} \tag{6.2}$$

where σ_i is the standard deviation (and thus σ_i^2 is the variance) of the measurement of the i^{th} data type. By adding water content data to the outflow data, the objective function to optimize from eq.6.1 can then be rewritten as:

$$O(\mathbf{b}) = \sum_{i=1}^{N} \left\{ w_i \left[Q_m(t_i) - Q_{sim}(t_i, \mathbf{b}) \right] \right\}^2 + \sum_{i=1}^{N} \left\{ v_i \left[\theta_m(h_i) - \theta_{sim}(h_i, \mathbf{b}) \right] \right\}^2 \tag{6.3}$$

where θ_m and θ_{sim} are the measured and simulated volumetric water content during the pressure steps h_i and v_i is the weighting factor. In general, there are different ways to minimize the objective function, whereby one of the most known and widely used algorithm is the Levenberg-Marquardt algorithm [*Marquardt*, 1963], which is already implemented within the HYDRUS software package.

6.1.3 SCE optimization algorithm

The Levenberg-Marquardt algorithm is only a locally convergent algorithm which is not always suitable for complex parameter estimation, especially if more than one minimum exists in the multi-parameter-space. To overcome the limitations of being trapped into local minima without finding the global solution global optimization methods are required. Therefore, the Hydrus 2D code was coupled with the global optimization algorithm SCE-UA (shuffled complex evolution–University of Arizona) introduced by *Duan et al*., [1992] within a Matlab environment. In the following, a short description of the SCE algorithm is given. For more details see *Duan et al*., [1992] or *Mertens et al*., [2005].

In general, the SCE algorithm comprises four steps:

(1) *Initialization*: an initial sample of parameter sets is randomly generated from the feasible parameter space. For each parameter set, the objective function, O, presented in eq.6.1 or 6.3 is calculated. The initial sample size $s = p$ x m, where p is the number of complexes and m is the number of points in each complex.

(2) *Partitioning into complexes*: the s points are ranked in order of increasing objective function value. The s points are then partitioned into p complexes each containing m points, such that points corresponding to function values $\{O_1, O_{p+1}, \ldots, O_{s-p+1}\}$ form the first complex, points corresponding to function $\{O_2, O_{p+2}, \ldots, O_{s-p+2}\}$ values form the second complex, etc.

(3) *Evolution*: a subcomplex of size q is formed from the complex by randomly choosing q points from the m points in the complex. A triangular probability distribution is used for assigning the probability of a point to be included in the subcomplex (i.e. larger probability for points with smaller objective function value). The subcomplex is evolved (offspring generation) according to the Simplex algorithm [*Nelder and Mead*, 1965] and evolution steps are taken by each complex.

(4) *Complex shuffling*: the new sample of s points is shuffled and new complexes are formed, conform to step 2. Steps 2 – 4 are repeated until a stopping criterion is met. *Duan et al*., [1994] recommendations were followed in choosing the algorithmic parameters.

The most important algorithmic parameter is the number of complexes p. *Kuczera,* [1997] suggested that the number of complexes should be larger then 3 and equal to the number of model parameters that needs to be estimated in the optimization routine, on the expense, of course, of the computing time. In our study the number of complexes was set to 5, which we found to be a good compromise between search efficiency and computation time.

The algorithm was considered to converge when the objective function changed less then 0.01% in 10 consecutive loops of the algorithm.

6.1.4 Numerical feasibility study

To test the feasibility of combining conventional outflow data from MSO experiments with water content data derived from MRI for a two domain system, here a coaxial phantom, a synthetic case study was performed. The HYDRUS-2D [*Šimůnek et al*., 2006] model was used to predict and optimize the MSO experiment of a coaxial sample using the Mualem – van Genuchten parameterization of the retention function [*van Genuchten*, 1980] (see also 3.4. and 4.1.3.). The initial guess of the soil hydraulic parameters required for the hydraulic model was derived from the Rosetta database [*Schaap et al*., 2001] for each material (Table 6.1). The MSO was simulated for a 2D axis-symmetrical soil profile of 38mm width and 145mm length non-equidistantly discretised with 4014 nodes. The material of the soil profile was separated in two domains: fine domain from 0 to 17.5mm and coarse domain to 17.5 to 38mm from the rotation axis. The model was initialized in pressure head by setting h to 0 which corresponds to full saturation. The lower boundary was set to variable head representing measured pressure applied during the experiment. All remaining boundaries were set to zero flux. Ten observation nodes were inserted in the model domain at predefined position, whereby 5 were located in the fine and 5 in the coarse material in order to gain information about water content changes inside the sample during each pressure application.

In the first step, the cumulative outflow with respect to the applied suction and the water content measurements from the ten observation nodes inserted into the model were used as input data in the inversion routine for minimization of eq. 6.3 and estimation the hydraulic properties of both materials.

In the second step, Gaussian noise was added to the input data and the inversion was performed again. The reason of adding noise to input data was to simulate a case close to reality in which the MRI amplitude data are collected within 10% deviation from linearity, especially for low saturations and high clay content, [*Stingaciu et al*., 2009]. In general, we tested the fitting of 8 hydraulic parameters, namely θ_s, α, n, and K_S while θ_r was set fixed to 0 for each material domain. Constraining θ_r to zero is a well established procedure in MSO experiments because no information about the residual water content will be archived by the measurement itself, and therefore, estimating θ_r will be associated with a high uncertainty for the parameter.

6.1.5 Sample preparation

For the experimental study a coaxial sample based on the geometry shown in Fig.6.2. was constructed from sand and a sand clay mixture to ensure variability of the hydraulic properties between the inner and the outer core of the sample. The sample, further referred as *S2fine*, was constructed from fine sand FH32 for the outer core and kaolin-FH32 homogeneous mixture, 15% mass percents of kaolin, for the inner core. The quartz sand FH32 (Quarzwerke Frechen, Germany) has a particle size distribution between 0.1 – 0.4mm and an iron content <0.05%. The kaolin used in the clay mixture was pure hydrated aluminum silicate powder (Sigma-Aldrich, Germany) with particle size distribution between 0.1 and 4 µm and an iron content <0.58%. Detailed information about the two materials can be looked up in Annex 2.

The sample was filled into a teflon tube with an inner diameter of 76mm and a height of 145mm. The inner core diameter was 35mm. The bottom of the tube consists of a porous glass plate with a pore size between 40-90µm (RoBu, Germany) to allow saturation of the system from the bottom. In order to maintain a constant pressure inside the sample during the MSO experiment and to avoid air to leave the sample a porous nylon tissue (Whatman filters, USA) with high conductivity and a bubble point of 2bar was placed above the lower glass plate.

6.1.6 MSO experiment

In our study MSO experiments were performed by applying an overpressure by compressed air to the soil column from the top end of the setup shown in Fig.6.2. Using overpressure greatly facilitates the experimental setup compared to the classical approach of applying an under pressure at the lower end of the soil column. Various MSO experiments starting from complete saturation were repeated several times followed by re-saturation and subsequent equilibration to settle down the material within the column. The last drainage curve was performed for pressure steps: 20, 35, 50, 70, 350, and 850mbar. In the following, only the last drainage curve, which was used in the inverse modeling procedure, will be discussed. During the last drainage cycle MRI images were recorded. The pressure applied to the soil column was monitored on top of the sample using a digital pressure sensor and the cumulative outflow at the lower end of the column was collected on a balance and weighted automatically at constant time intervals of one minute.

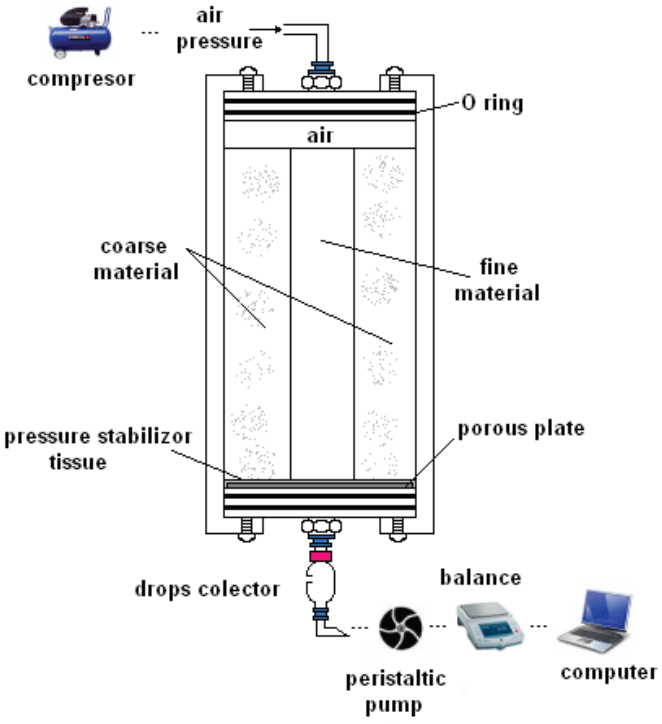

Fig.6.2.Sketch of the MSO experimental setup

6.1.7 MRI experiments

The water content in different regions inside a sample can be estimated with a variety of methods. Among these methods, ^{1}H magnetic resonance imaging (MRI) has proved to be a reliable method to predict accurately the water content within a soil sample because the recorded MRI signal amplitude can be directly and linearly related to the water content of the sample [*Hall et al*., 1997; *Stingaciu et al*., 2009]. Prior studies [*Amin et al*., 1996; *Hall et al*., 1997; *Stingaciu et al*., 2009; *Pohlmeier et al*., 2009] recommended that low field MRI is preferable for investigating soils. Due to the fact that low field MRI scanners are still under development, in this study high field MRI (4.7T) was used. Nevertheless, there are several limitations in using high field MRI for determination of the water content in natural porous media. First, paramagnetic impurities such as Fe^{3+} and Mn^{2+} ions can seriously reduce the signal by acceleration of the relaxation processes [*Hall et al.,* 1997; *Keating and Knight*, 2007]. This problem was overcome in our study by using pure samples based on sand and pure kaolin clay for which the paramagnetic content is less then 0.5%.

Another problem encountered in high magnetic field measurements is the fast decay of the MRI signal due to the diffusion in internal magnetic field gradients. By a comparison study between high and low magnetic field measurements, *Stingaciu et al*., [2009] showed that for sufficiently short echo time the high magnetic field measurements of natural porous media are not influenced by the diffusion in internal gradients. Nevertheless, the classical multi-echo MRI sequences proposed by *Edzes and van Dusschoten* [1998] do not always allow the use of a very short echo time and only a truncated signal is recorded due to the very fast relaxation in small pores or to very low water content (dry sample). This was regarded as a serious problem in our study because water content drops dramatically inside the sample at high pressure steps.

Therefore, a phase-encoding 3D-MRI sequence named ''*ct*3D'' was employed (Fig.6.3.), for the determination of signal amplitude, e.g., of the water content inside the sample. This pulse sequence is basically a single-point-imaging sequence and consists of a nonselective excitation pulse, followed by phase encoding in all three directions and acquisition of only a single data point. The *ct* term refers to the *constant time* between the excitation and acquisition. In this sequence *k-space* is addressed point by point and filled rectangulary. This sequence ensures the linearity between the measured signal and the water content even at very low saturation as a consequence of a very short time lap between excitation and acquisition.

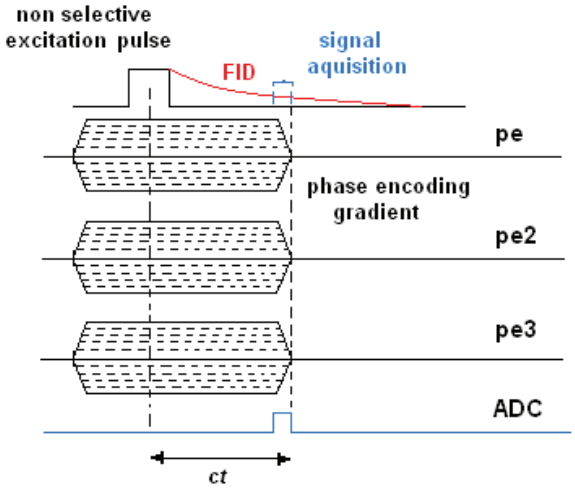

Fig.6.3. *ct*3D pulse sequence

The MRI experiments were performed on a 4.7T (200MHz ^{1}H resonance frequency) vertical wide bore superconducting magnet (Magnex Scientific, UK) connected to a Varian console The NMR RF-resonator is a 'birdcage'- type resonator with an internal diameter of 170mm and 180mm length. Images were recorded using the following parameters: constant time, ct = 0.050ms, repetition time, T_R = 65ms, flip angle of 6 degrees with a resolution of 5.31mm per pixel (matrix size 32 x 32 x 32 pixels for 170 x 170 x 170 mm). This resolution was set with respect to the experimental setup of the MSO with relatively short times between pressure steps and fast outflow at the lower end of the soil column, especially at low pressure applied, and the required data points measured with MRI.

6.2 Results and Discussions

6.2.1 Numerical study

In general, the feasibility study was performed in three steps. First, we estimated hydraulic properties from outflow and water content data taken from a forward model with known hydraulic properties for each material domain. The hydraulic properties for this forward run are listed in Table 6.1. In a second step, Gaussian noise was added to the input data for a second optimization. The estimated parameters from the inversion using no noisy data are listed in Table 6.1. The total SSR (sum of square residuals) was 0.0159 and was achieved after 1859 model runs. Convergence was achieved after 3285 model runs. The estimated parameters from the inversion using noisy data are also listed in Table 6.1. The total SSR was 0.02 and was achieved after 1719 model runs. Convergence was achieved after 3115 model runs.

Table 6.1. Hydraulic parameters used in the forward simulation of the feasibility study and estimated ones for the inversion based on no noise and noisy data from outflow and water content at predefined observation nodes.

Material domain		θ_r mm^3/mm^3	θ_s mm^3/mm^3	α mm^{-1}	n -	K_S mm /min
forward model	coarse	0	0.43	0.015	2.7	4.95
	fine	0	0.36	0.003	2.6	2.29
no noise	coarse	0	0.4338	0.0156	2.7387	4.3228
	fine	0	0.3603	0.003	2.5943	2.3132
with noise	coarse	0	0.4238	0.0154	2.7251	4.3422
	fine	0	0.3711	0.003	2.6325	2.3826

Comparing the fitted hydraulic parameters with the initial values with respect also to the total SSR values, we can conclude that all 8 parameters have been successfully estimated.

In a final step, it was analyzed whether the parameters were uniquely determined and investigated potential trade-offs between the optimized parameters using a grid search algorithm. Therefore, the parameters were stepwise changed within given intervals. An overview of all parameter combinations and corresponding ranges for the grid search is listed in Table 6.2.

Table 6.2. Combinations and parameter ranges for the grid search algorithm and calculation of parameters spaces

Parameters combinations	variable 1 (min – max)	variable 2 (min – max)
α - K_S	0.005 – 0.025	1.95 – 7.95
α - n	0.005 – 0.025	1.70 – 3.70
n - K_S	1.70 – 3.70	1.95 – 7.95
θ_s - n	0.33 – 0.53	1.70 – 3.70
θ_s - α	0.33 – 0.53	0.005 – 0.025
θ_s - K_S	0.33 – 0.53	1.95 – 7.95
α - K_S	0.001 – 0.005	0.29 - 4.29
α - n	0.001 – 0.005	1.70 – 3.70
n - K_S	1.70 – 3.70	0.29 - 4.29
θ_s - n	0.26 – 0.46	1.70 – 3.70
θ_s - α	0.26 – 0.46	0.001 – 0.005
θ_s - K_S	0.26 – 0.46	0.29 - 4.29
α1 - α2	0.005 – 0.025	0.001 – 0.005
α1 – n2	0.005 – 0.025	1.70 – 3.70
α1 - K_S2	0.005 – 0.025	0.29 - 4.29
α1 - θ_s2	0.005 – 0.025	0.26 – 0.46
n1 - α2	1.70 – 3.70	0.001 – 0.005
n1 - n2	1.70 – 3.70	1.70 – 3.70
n1 - K_S2	1.70 – 3.70	0.29 - 4.29
n1 - θ_s2	1.70 – 3.70	0.26 – 0.46
θ_s1 - α2	0.33 – 0.53	0.001 – 0.005
θ_s1 - n2	0.33 – 0.53	1.70 – 3.70
θ_s1 - K_S2	0.33 – 0.53	0.29 - 4.29
θ_s1 - θ_s2	0.33 – 0.53	0.26 – 0.46
K_S1 - α2	1.95 – 7.95	0.001 – 0.005
K_S1 - n2	1.95 – 7.95	1.70 – 3.70
K_S1 - K_S2	1.95 – 7.95	0.29 - 4.29
K_S1 - θ_s2	1.95 – 7.95	0.26 – 0.46

Overall 40 steps were performed for each parameter resulting in 1600 model runs. Within each model run, the same weighting as stated above was chosen. The calculated response functions or parameter spaces from the inversion of the noisy data for selected parameter combinations are plotted in Fig.6.4. All remaining combinations are appended as Annex 5. Note that the scale of the SSR is expressed in $\log_{10}$ to facilitate interpretation of the parameter spaces.

In general, all parameter spaces indicate a clear single optimum. For the coarse domain (upper row Fig.6.4.) the parameter space shows a weak correlation for all parameters while α and n parameters are slightly correlated. Additionally, some numerical instability caused discontinuities in the parameters space ''n versus α''. It can also be seen that K_S can be varied within a certain range without affecting the SSR too much (right plot upper row).

For the fine domain the parameter space ''K_S versus α'' and ''n versus α'' show no correlation between parameters at all. Again K_S and n are slightly correlated. Nevertheless, the indication that only one minimum is detectable in all parameter spaces and that the correlation is weak between parameters leads to the conclusion that a combination of classical outflow data and MRI derived water contents is sufficient information for the estimation of hydraulic properties in a two domain setup as analyzed here.

6.2.2 Real – case study results

Encouraged by the results of the feasibility study shown above a real-case experimental MSO was performed on the coaxial sample *S2fine* described in chapter 6.1.5, sample preparation. A full description of the experimental setup of the MSO experiment is given in chapter 6.1.6. The observed cumulative outflow at the lower end of the soil column versus time as well as the applied pressure steps are plotted in Fig.6.5. The experimental drainage curve for the *S2fine* sample shows that approximately 95% of the total outflow was extracted by the 20-70mbar pressure steps, and therefore, only 5% at larger ones (350 and 850mbar). With respect to the sample setup with two material domains, this leads to the assumption that the sand (coarse domain) was drained during the low pressure range; higher pressures steps are necessary to drain the water from the inner core with high clay content, and therefore, smaller pores. This observation is also supported by the MRI images of the sample (see Fig.6.6.). The 4.7T MRI system was used to record images of the *S2fine* sample during each pressure step application.

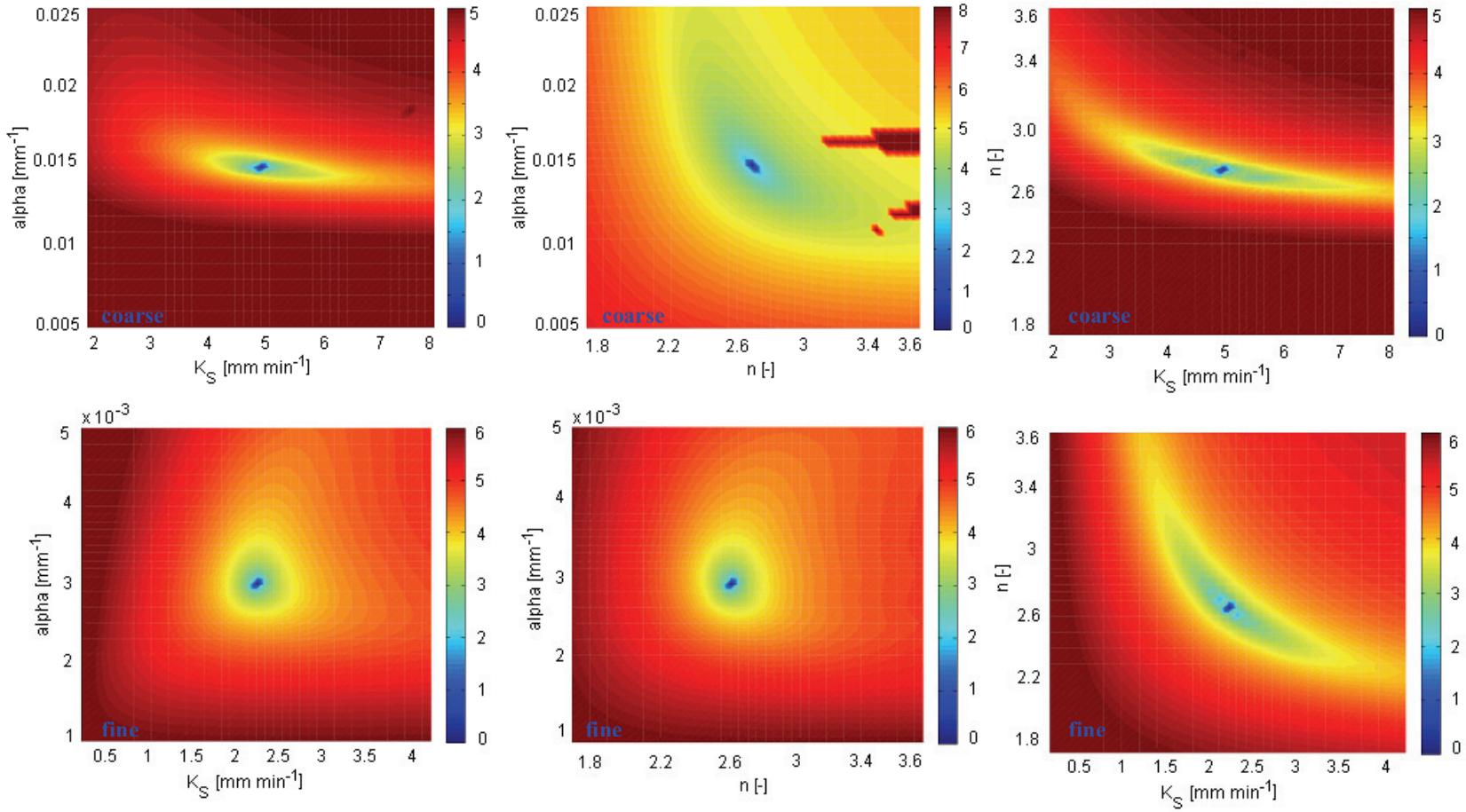

Fig.6.4. Parameter space for coarse (upper row) and fine (lower row) domain: K_S versus α; n versus α, and K_S versus n for the parameters estimated from inversion of the noisy data. Note that the scale is expressed in $\log_{10}$ of SSR

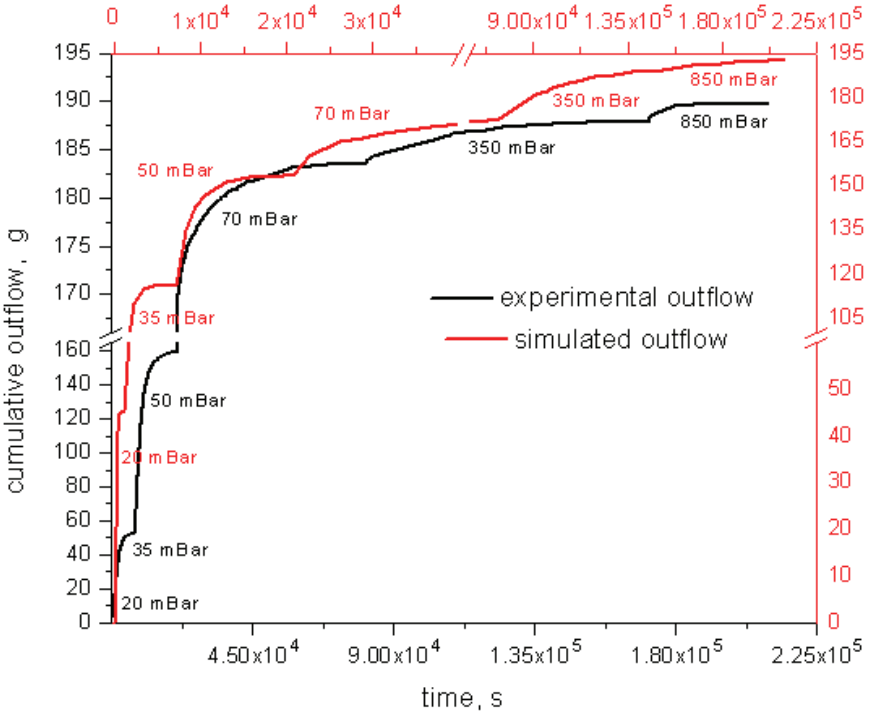

Fig.6.5.Cumulative outflow as a function of time with indication over pressure steps. Note that for the Hydrus2D3D outflow simulation Rosetta hydraulic properties were used

Overall 42 MRI snapshots were taken during the experiment as follows: 3 experiments during the 20mbar pressure step; 6 during 35 mbar; 7 during 50mbar; 10 during 70mbar; 11 during 350mbar and 5 experiments during the 850mbar pressure steps. The idea was to record as many as possible MRI images for each pressure step whereby the unequal distribution of the MRI data could not be avoided due to different time windows of each pressure step and according drainage. Nevertheless, being time restricted by the length of the MRI sequence this distribution was set to best describe the shape of the outflow curve. The time points at which the MRI images were recorded were used as printing times in the simulation and further in the inversion of the MSO experiment. Figure 6.6. shows the MRI images of the *S2fine* sample for different pressure steps.

Qualitatively speaking, the images for each pressure step clearly show the changes in the water content as observed from analyzing the cumulative outflow curve. For the first pressure steps the signal intensity variations (which are proportional to water content changes within the sample) are larger in the sand core that is nearly dry (the signal intensity becomes close to zero) after the 70mbar pressure. The inner core is slowly drained during each pressure

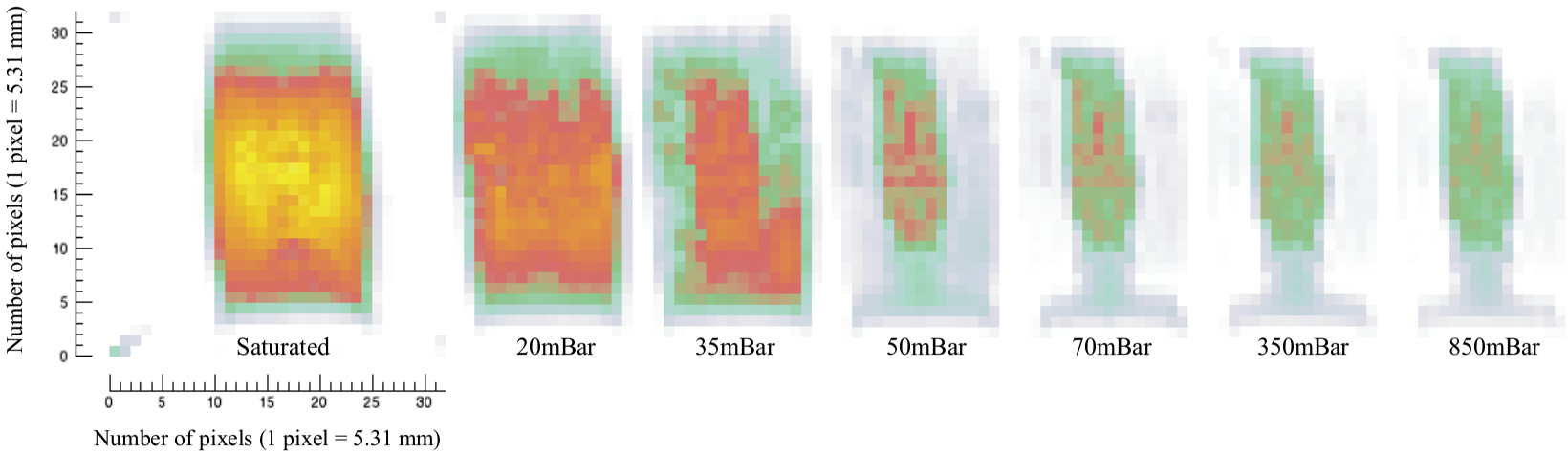

Fig.6.6.MRI images of a centered vertical slice of the *S2fine* sample; one image for each pressure step applied in the MSO experiment

application and even after the largest pressure step (850mbar) a significant amount of water is still present in the sample core sustaining the idea that higher pressure values are required, values that could not be achieved with our setup.

Quantitatively, the water content and the variations in water content within the sample were observed for 10 regions of interest (ROI) in a middle slice of the sample: namely 5 in the inner and 5 in the outer core. The coordinates of the observation regions correspond to the position of the observation nodes used later in the numerical simulation. The water content over a ROI was interpolated between calibration values based on the assumption of linearity between MRI signal amplitude and water saturation. The validity of this concept was already proven by *Stingaciu et al.*, [2009] (see chapter 4.2). Therefore 4 calibration samples from sand FH32 with similar packing density and known volumetric water content (0.36; 0.21; 0.12 and 0.07) were constructed and measured with the same MRI protocol (Fig.6.7.a) and the signal amplitudes obtained were used as reference amplitudes in the interpolation of the ROI signal (Fig.6.7.b). The water content from the investigated ROI-s and its variation in time with respect to pressure application is shown in Fig.6.8.b. The ROI-s situated in coarse domain(outer core) show a steep decrease in water content from 0.38 to 0.05volumetric water content within the low pressure range (first 400min.). Later, during the high pressure steps no significant changes are visible in the sand which is nearly dry (the volumetric water content changes from 0.05 - 0.02).

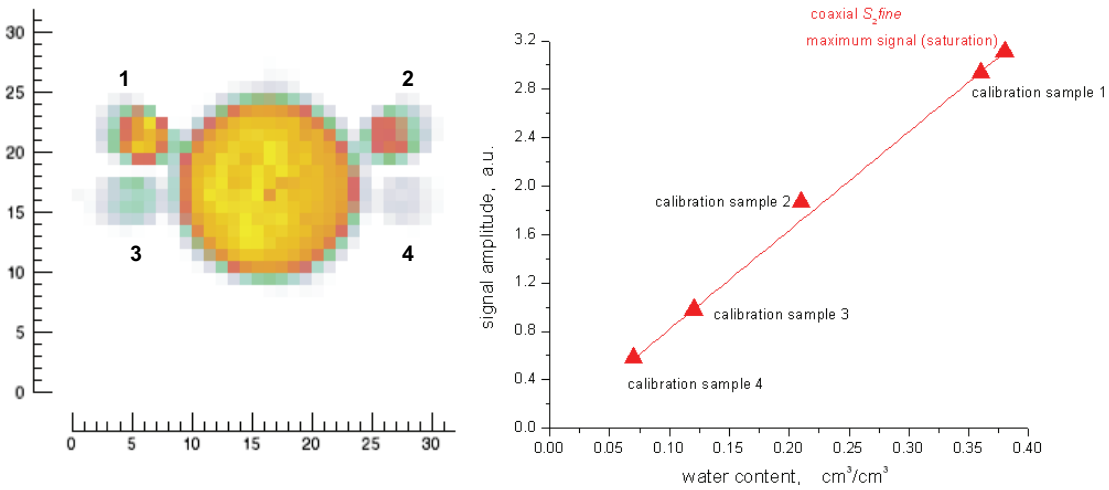

Fig.6.7.a) Reference image for the interpolation of the signal amplitude; axial central slice of the coaxial sample *S2fine* and calibration samples and b) Linear interpolation of the maximum MRI signal

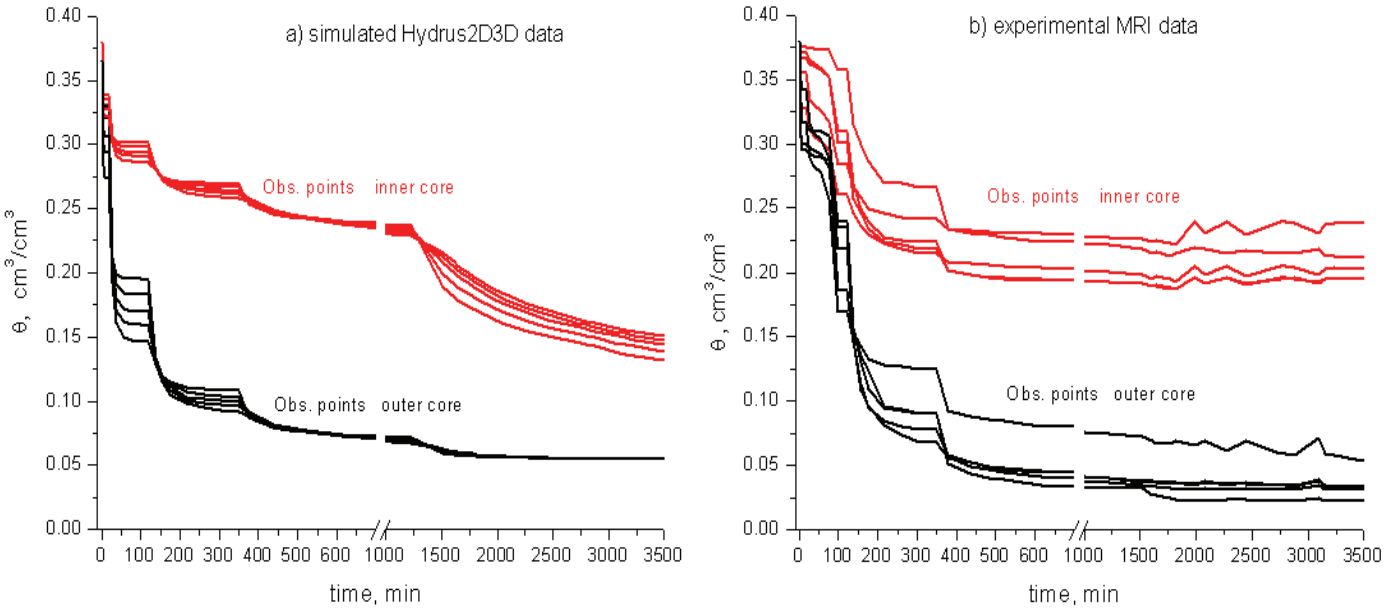

Fig.6.8.Water content from ten observation nodes at a precise position inside the sample during the multi-step-outflow experiment. a) Simulated observation nodes and b) average water content over ten region of interest (ROI) from MRI experimental data. Note that ROI were selected at the same coordinates as simulated observation nodes

The ROI-s situated in fine domain(inner core) which is clay based material show a very slow decrease of water content and at the end of the experiment there is an important amount of water remained within the core (0.19 - 0.20 volumetric water content). The level of noise increases for high pressure steps (350 and 850mbar) most probably due to the increasing noise level in the MRI signal amplitude recorded at very low saturations.

Further, the cumulative outflow and the water content from ROI-s were used as input data in Hydrus2D3D code coupled with the global optimization algorithm SCE-UA to simultaneously estimate the hydraulic parameters for both materials of the coaxial sample *S2fine*. In the first steps a forward MSO model with known hydraulic properties for each material domain (Table 6.3) was simulated to describe the experimental MSO presented above. The simulated cumulative outflow at the lower end of the soil column versus time as well as the applied pressure steps is plotted also in Fig.6.5. In comparison with the experimental results, the numerical simulation of the MSO experiment for *S2fine* sample shows slightly higher value for the cumulative outflow with no visible distinction between the high pressure (350 and 850mbar) steps. Nevertheless, the outflow trend is identical, e.g. 95% of the total outflow was collected during the low-pressure steps (0 to 70mbar). The differences observed can be due to differences in saturated conductivity values as well as due to sample heterogeneity that is not taken into account in simulation of the MSO experiment.

The simulated changes in water content within the sample for the entire simulation time were picked at 10 observation nodes and are shown in Fig.6.8.a. It can be clearly seen that the drainage started from saturation for each of the two materials immediately after pressure was applied. Water content dropped from saturation, θ_s = 0.36cm^3 cm^{-3} to a water content of 0.05cm^3 cm^{-3} in the sandy outer core at 70mbar pressure applied. With higher pressure steps (350 and 850mbar) no significant water volume could further be extracted from the sand. In contrast, the inner core (clay based material) shows a slow decrease in the water content from θ_s = 0.38cm^3 cm^{-3} to a water content of 0.12cm^3 cm^{-3} over the entire pressure range. Therefore, much higher values of pressure are necessary for full drainage of this fine material.

By comparing the simulated water content from observation nodes with the experimental one from ROI-s (Fig.6.8. a and b) it is interesting to note that the MRI data show scatter while the simulated do not – a natural consequence of the heterogeneities in the sample that have not been taken into account in the simulations. Nevertheless, the average values of the water content for the coarse and fine regions are comparable. Due to the sequence used for investigation (single point imaging sequence in which the signal is acquired directly after

excitation with no relaxation time) the possibly of underestimating the water content within the sample by MRI was eliminated, fact proved also by Fig.6.8.b in which for the inner core the water content from ROI is higher then the simulated one. In comparison, the ROI-s from outer core show stronger drainage then the simulated observation nodes from the same side of the sample. These differences can be due to the hydraulic properties, especially wrong value of the hydraulic conductivity assumed by the Rosetta software in the simulation of the MSO experiment.

Therefore, in the second step the hydraulic parameters have been estimated from the inversion using the cumulative outflow and the water content as input data. For the inversion the numerical model was set up in terms of boundary conditions in the same way as the real experiment (full saturation, h = 0 as initial condition; variable head as the lower boundary representing measured pressure applied during the experiment and no flux for all remaining boundaries). The printing times in the simulation and further in the inversion of the MSO experiment, were chosen the time points at which the MRI images were recorded. For the inversion, the data were weighted by standard deviation (SD = 0 for both data set) for a number of 5000 iterations. 6 parameters have been fitted: α, n and K_S while θ_r parameter was set to 0 for each material domain and θ_s parameter was fixed to the value determined experimentally by MRI. The number of complexes was set to 5. The estimated parameters from the inversion using real case experimental data are listed in Table 6.3.

Table 6.3. Hydraulic parameters used in the forward simulation of the MSO experiment and estimated ones for the inversion using outflow and water content data

Material domain		θ_r mm^3/mm^3	θ_s mm^3/mm^3	α mm^{-1}	n -	K_S mm /min
forward simulation	coarse(FH32)	0.0534	0.3656	0.00301	4.6323	10.097
	fine(clay mix)	0.0638	0.3797	0.00254	1.7797	0.6469
inversion	coarse(FH32)	0	0.38	0.0024	7.1	1.1357
	fine(clay mix)	0	0.38	0.0029	1.82	0.0390

The total SSR was 0.018 and was achieved after 2017 model runs. Convergence was achieved after 4002 model runs. The parameters were slightly correlated (the highest value is the correlation matrix shows negative correlation, - 0.53, between α and K_S for sand FH32). Comparing with the initial input it can be seen that for the coarse domain (FH32) the point of first drainage (air entrance) comes earlier. Some differences are visible in the n parameter,

which describes the slope of the water retention curve. However it is well known the insensitivity of the water retention function to high values of n. The most pronounced differences can be observed in the K_S parameter with values one order of magnitude lower for the experimental data. A decreasing of K_S indicates lower values of the unsaturated hydraulic conductivity, K_r, as eq.3.14 shown (parameterization of the hydraulic conductivity function, chapter 3.4). This will lead to the conclusion that for real-case experiment less water can be extracted by drainage in comparison with simulation. This is consistent with the Fig.6.5. The difference was expected and is also consistent with MRI measurements from ROI-s (Fig.6.8.) for the inner core material (clay mixture).

Nevertheless, the hydraulic conductivity of sand is not consistent with MRI measurements from ROI-s in the outer core material at low water content, which overestimate the drainage showing higher K_S values. These differences, as stated before, are most probably small errors in the estimation of the water content by interpolation due to the increasing noise level in the MRI signal amplitude recorded at very low saturations.

6.3 Conclusions

Summarizing the findings reported above we see that the feasibility experiment proved that magnetic resonance imaging can be efficiently combined with classical soil physics method like multi-step-outflow for supplementing cumulative outflow data with water content, at different depth inside a sample, in the objective function use to optimize the estimation by inversion of hydraulic properties of two different materials simultaneously.

Consequently, MSO experiments can be performed on a real-case sample and during each pressure application MRI images can be recorded with an appropriate pulse sequence, that will overcome or minimize the problems encountered when natural porous media are investigated with magnetic resonance methods (fast relaxation due to paramagnetic ions or diffusion processes, that will underestimate the water content), and will ensure a side to side correlation of the MRI water content with weighted outflow. From the combination of the two experiments it was shown that the convergence of the objective function occurred quite fast and the hydraulic parameters can be successfully estimated with no strong correlation between the parameters.

This is an important finding considering the well-known problems of estimating the hydraulic properties of a natural porous system based on two different materials (sand with clay inclusions, imbedded lignite in sand, etc.) which normally are treated as single materials

or separated in two materials for the estimation of the retention function. Additionally, MRI can be used for the delineation of the two materials within the bulk sample (e.g. Kopecky-ring). Nevertheless, it should be tested in future studies if natural heterogeneous structures such as clay inclusions imbedded in coarser material or imbedded lignite in sand originated from mining pits can be also analyzed in the same way as presented here.

7. General conclusions and Outlook

Summarizing, the water content of natural porous media can be successfully determined by multi-echo sampling and extrapolation to amplitudes at $t \to 0$. When characterizing the water content in mixed systems with varying texture and saturation, the employment of low magnetic field strength gives more reliable results. It can be stated that relaxation in unsaturated clay based porous media is major surface influenced. The apparent relaxation, recorded at sufficiently short echo time so that the diffusion influence can be neglected, is best discussed in terms of the surface relaxation that further can be transformed to characterize the pore size distribution of the soil matrix.

The NMR T_1 and T_2 relaxometry measurements can be a quick alternative to classical methods (pressure plates, mercury intrusion, and multi-step-outflow) for the estimation of pore size distribution, retention curve and the hydraulic properties of a porous media. The NMR does not exclude the other classical methods; each method, within its one limitation, is appropriate for determination of pore size distribution with a strong dependence on the sample characteristics, sample preparation and experimental conditions. The major advantage of NMR is the short measurement time which allows the analysis of large quantities of samples necessary to characterize field – or catchments scale hydraulic properties.

Due to the fact that water content can be reliable estimated from magnetic resonance imaging measurements, MRI experiments over a heterogeneous sample can be efficiently combined with classical soil physics method like multi-step-outflow for estimation, by inversion, of hydraulic properties of two or more different materials simultaneously, supplementing cumulative outflow data with water content inside the sample in the objective function. Local and global optimization procedure can be used further to optimize this kind of objective function and uniquely determine the hydraulic parameters.

The results presented in this thesis showed that MRI is capable of providing quantitative, isotope-specific, volumetrically averaged information about fluids imbibed in natural porous media and implicitly about pore size distribution and hydraulic properties. Nevertheless, further detailed investigations upon diffusion process, pore geometry, pore connectivity, interactions at the fluid-solid interface with the use of low-field-MRI will greatly contribute to understand the hydraulic properties of soils and improve their management.

Acknowledgements

Many thanks to:

- Dr. Andreas Pohlmeier for supervising, NMR training, constant motivation and support
- Dr. Lutz Weihermüller for soil physics and modeling training
- Prof. dr. Siegfried Stapf for interesting e-mail discussions and support as well as for official supervising
- Dr. Dagmar van Dusschoten for help with high field setup
- The DFG (projects PO 746/2-1) for two years financial support
- Y. Q. Song (Schlumberger-Doll Research, Connecticut) for access to inverse Laplace transform software
- Dr. Norbert Klitzsch and dr. Oliver Mohnke (Applied Geophysics, RWTH Aachen University) for their 0.1T Halbach setup
- Dr. Peter Blümler and Normen Hermes for help with building the 0.15T Halbach setup
- Prof. dr. Mathieu Javaux and Guido Rentmeesters from UCL - Belgium for the access and help with Hg-intrusion measurements
- Dr. Sabina Haber-Pohlmeier for the T_1 measurements
- Anke Langen and Benedikt Scharnagl for providing various retention function measurements
- Claudia Walraf for BET measurements
- Jürgen Höltkemeier for help with pressure setup
- All my colleagues from Agrosphere Institute for the excellent collaboration and friendly work atmosphere

and…

- Prof. dr. Ioan Ardelean and Prof. dr. Harry Vereecken for making all this possible.

References

Adams, J.M., Breen, C., and C. Riekel (1979), *J. Colloid Interface Sci.*, *68*, 214-220.

Amin, M.H.G., Richards, K.S., Chorley, R.J., Gibbs, S.J., Carpenter, T.A., and L.D. Hall (1996), Studies of soil-water transport by MRI, *Magnetic Resonance Imaging, 14*, 879-882.

Barrie, P.J. (2000), Characterization of porous media using NMR methods, *Annual Reports on NMR Spectroscopy, 41*, 265-278.

Bird, N.R.A., Preston, A.R., Randall, E.W., Whalley, W.R., and A.P. Whitmore (2005), Measurement of the size distribution of water-filled pores at different matrix potentials by stray field nuclear magnetic resonance, *Eur. J. of Soil Sci.*, *56,* 135 – 143.

Bittelli, M., and M. Flury (2009), Errors in water retention curves determined with pressure plates, *Soil Sci. Soc. Am. J., 73*, 1453-1460.

Blümich, B. (2000), NMR Imaging of Materials, *Oxford University Press,* Oxford, UK.

Blümich, B. (2004), Essential NMR, Springer *Science,* Berlin, Germany.

Blümich, B., Mauler, J., Haber, A., Perlo, J., Danieli, E., and F. Casanova (2009), Mobile NMR for geophysical analysis and materials testing, *Pet. Sci., 6,* 1-7.

Brownstein, K.R., and C.E. Tarr (1977), Spin-lattice relaxation in a system governed by diffusion, *Journal of Magnetic Resonance, 26,* 17-24.

Brownstein, K.R., and C.E. Tarr (1979), Importance of classical diffusion in NMR studies of water in biological cells, *Physical Review A, 6,* 2446-2453.

Brunauer, S., Emmett, P.H., and E. Teller (1938), Adsorption of gases in multimolecular layers, *Journal of the American Chemical Society*, *60*, 309-319.

Bolt, G.H (1976), Soil physics terminology, *Bulletin of the International Society of Soil Science*, *49*, 26–36.

Buckingham, E. (1907), Studies on the Movement of Soil Moisture, *Bulletin No. 38, U. S. Department of Agriculture, Bureau of Soils*, Washington, D.C.

Burdine, N.T. (1953), Relative permeability calculation from pore size distribution data, *Petr.Trans., Am. Inst. Mining Metall. Eng.*, *198*, 71-77.

Callaghan, P.T., MacGowan, D., Packer, K.J., and F.O. Zelaya (1991), Influence of field gradient strength in NMR studies of diffusion in porous media, *Magnetic Resonance Imaging*, 9, 663-671.

Callaghan, P.T. (1991), Principles of nuclear magnetic resonance microscopy*, Oxford University Press*, Oxford, UK.

Campbell, G.S. (1988), Soil water potential measurement: An overview, *Irrig. Sci., 9*, 265–273.

Carr, H.Y., and E.M. Purcell (1954), *Phys*. *Rev., 94*, 630.

Cebula, D.J., Thomas, R.K., and J.W. White (1980), *J. Chem. Soc. Faraday I*, *76*, 314-321.

Chelcea, R.I., Fechete, R., Culea, E., Demco, D.E., and B. Blümich (2009), Distributions of transverse relaxation times for soft-solids measured in strongly inhomogeneous magnetic fields, *Journal of Magnetic Resonance, 196*, 178-190.

Cresswell, H.P., Green T.W., and N.J. McKenzie (2008), The adequacy of pressure plate apparatus for determining soil water retention, *Soil Sci. Soc. Am. J.*, *72*, 41-49.

D'Hollander, E.H. (1979), Estimation of the Pore Size Distribution from the moisture characteristic, *Water Resources Research*, *15*, 107-112.

Duan, Q.Y., Gupta, V.K., and S. Sorooshian (1992), Effective and efficient global minimization for conceptual rainfall-runoff models, *Water Res. Research*, *82(4)*, 1015–1031.

Duan, Q., Sorooshian, S., and V.K. Gupta (1994), Optimal use of the SCEUA global optimization method for calibrating watershed models, *Journal of Hydrology, 158*, 265–284.

Dunn, K.J., Bergman, D.J., and G.A. Latorraca (2002), Nuclear magnetic resonance: petro physical and logging applications, *Handbook of Geophysical Exploration, 32*, Pergamon, Amsterdam.

Eching, S.O., and J.W. Hopmans (1993), Optimization of hydraulic functions from transient outflow and soil water pressure data, *Soil Sci. Soc. Am. Journal, 57*, 1167–1175.

Edzes, H.T., Dusschoten, v. D., and H. Van As (1998), Quantitative T_2 imaging of plant tissues by means of multi-echo MRI microscopy, *Magnetic Resonance Imaging, 16*, 185-196.

Farrher, G., Ardelean, I., and R. Kimmich (2007), The heterogeneous distribution of the liquid phase in partially filled porous glasses and its effect on self-diffusion, *Magnetic Resonance Imaging*, *25*, 453-456.

Gee, G.W., Ward, A.L., Zhang, Z.F., Campbell G.S., and J. Mathison (2002), The influence of hydraulic nonequilibrium on pressure plate data, *Vadose Zone J.*, *1*, 172–178.

Gladkikh, M., D. Jacobi, and F. Mendez (2007), Pore geometric modeling for petrophysical interpretation of down hole formation evaluation data, *Water Resources Research, 43*, W12S08.

Godefroy, S., Korb, J.P., Fleury, M. and R.G. Bryant (2001), Surface nuclear magnetic relaxation and dynamics of water and oil in macroporous media, *Physical Review E: Statistical, Nonlinear, and Soft Matter Physics*, *64*, 021605/01–021605/13.

Haines, W.B. (1930), Studies in the physical properties of soils, *J. Agric. Sci*., *20*, 97-116.

Hall, L.D., Amin, M.H.G., Dougherty, E., Sanda, M., Votrubova, J., Richards, K.S., Chorley, R.J., and M. Cislerova (1997), MR properties of water in saturated soils and resulting loss of MRI signal in water content detection at 2 tesla, *Geoderma*, *80*, 431-448.

Hashemi, R.H., Bradley, W.G., and C.G. Lisanti (2004), MRI The Basics, *LWW* Philadelphia, USA.

Hedberg, S.A., Knight, R.J., MacKay, A.L. and K.P. Whittall (1993), The use of nuclear magnetic resonance for studying and detecting hydrocarbon contaminants in porous rocks, *Water Resources Research*, *29*, 1163-1170.

Herrmann, K.H., Pohlmeier, A., Wiese, A., Shah, N.J., Nitzsche, O., and H. Vereecken (2002), Three-dimensional nickel ion transport through porous media using magnetic resonance imaging, *Journal of Environmental Quality, 31*, 506-514.

Hinedi, Z.R., Kabala, Z.Y., Skaggs, T.H., Borchard, D.B., Lee, R.W.K., and A.C. Chang (1993), Probing soil and aquifer porosity with nuclear magnetic resonance, *Water Resources Research*, *29(12)*, 3861-3866.

Hinedi, Z.R., Chang, A.C., and M.A. Anderson (1997), Quantification of microporosity by nuclear magnetic resonance relaxation of water imbibed in porous media, *Water Resources Research,* 33(*12)*, 2697-2704.

Hollenbeck, K.J., and K.H. Jensen (1998), Experimental evidence of randomness and nonuniqueness in unsaturated outflow experiments designed for hydraulic parameter estimation, *Water Resources Research*, *34 (4)*, 595-602.

Hopmans, J.W. and J. Simunek (1999), Review of inverse estimation of soil hydraulic properties, *in M.T. van Genuchten, F.J. Leij and L. Wu (eds), Proceedings of the International*

Workshop on Characterization and Measurement of the Hydraulic Properties of Unsaturated Porous Media, University of California, Riverside, CA, 643–659.

Hopmans, J.W., Simunek, J., Romano, N. and W.Durner (2002), Simultaneous determination of water transmission and retention properties, Inverse methods, *in J.H. Dane and G.C. Topp (eds), Methods of Soil Analysis, Part 4, Physical Methods, 3rd edition, Soil Science Society of America*, Madison, WI, chapter 3.6.2, 963–1008.

Hornak, J.P. (1996), Basics of MRI, *http://www.cis.rit.edu/htbooks/nmr/bnmr.htm.*, Verified February 2010.

Hürlimann, M.D., and D.D. Griffin (2000), Spin dynamics of Carr–Purcell–Meiboom–Gill-like sequences in grossly inhomogeneous B_0 and B_1 fields and application to NMR well logging, *Journal of Magnetic Resonance, 143*, 120–135.

Ioannidis, M.A., I. Chatzis, C. Lemaire, and R. Perunarkilli (2006), Unsaturated hydraulic conductivity from nuclear magnetic resonance measurements, *Water Resources Research*, *42*, W07201.

Jaeger, F., Bowe, S., van As, H., and G.E. Schaumann (2009), Evaluation of ^{1}H NMR relaxometry for the assessment of pore-size distribution in soil samples, *European Journal of Soil Science, 60*, 1052-1064.

Jury, W.A., Gardner, W.R., and W.H. Gardner (1991), Soil Physics, *5th edition, John Wiley & Sons*, New York.

Jury, W.A., and R. Horton (2004), Soil Physics, 6*th edition, John Wiley and Sons Inc.,* Hoboken, New Jersey.

Kasteel, R., Pütz, T., and H. Vereecken (2007), An experimental and numerical study on flow and transport in a field soil using zero-tension lysimeters and suction plates, *European Journal of Soil Science, 58 (3)*, 632-645.

Keating, K., and R. Knight (2007), A laboratory study to determine the effect of iron oxides on proton NMR measurements, *Geophysics*, *1*, E27-E32.

Kögel-Knabner, I. (1997), ^{13}C and ^{15}N NMR spectroscopy as a tool in soil organic matter studies, *Geoderma*, *80*, 243-270.

Kleinberg, R.L. (1994), Pore size distributions, pore coupling, and transverse relaxation spectra of porous rocks*, Magnetic Resonance Imaging*, *12*, 271-274.

Kleinberg, R.L. (1996), Utility of NMR T_2 distributions, connection with capillary pressure, clay effect, and determination of the surface relaxivity parameter ρ_2, *Magnetic Resonance Imaging*, *14*, 761-767.

Kleinberg, R.L. (1999), *Nuclear Magnetic Resonance, in P.-z. Wong, ed., Experimental Methods in the Physical Sciences*, Volume 35: Methods in the Physics of Porous Media.

Kleinberg, R.L., and M. A. Horsfield (1990), Transverse relaxation processes in porous sedimentary rock, *Journal of Magnetic Resonance*, *88*, 9-19.

Klute, A., and C. Dirksen (1986), Hydraulic conductivity and diffusivity: Laboratory methods, *in A. Klute (ed.), Methods of Soil Analysis, Part 1, Physical and Mineralogical Methods, 2nd edition, American Society of Agronomy and Soil Science Society of America*, *28*, Madison, WI, 687–734.

Kool, J.B., and J.C. Parker (1987), Development and evaluation of closed-form expressions for hysteretic soil hydraulic properties, *Water Resources Research*, *23*, 105–114.

Kool, J.B., Parker, J.C., and M.T. van Genuchten (1985), Determining soil hydraulic properties from one-step outflow experiments by parameter estimation: I. Theory and numerical studies, *Soil Science Society of America Journal*, *49*, 1348–1354.

Koorevaar, P., Menelik, G., and C. Dirksen (1983), Elements of soil physics, *Elsevier Science Publishing Company Inc*.

Kosugi, K. (1994), Three-parameter lognormal distribution model for soil water retention, *Water Resources Research, 30*, 891-901.

Kosugi, K. (1996), Lognormal distribution model for unsaturated soil hydraulic properties, *Water Resources Research, 32*, 2697-2703.

Kuczera G. (1997), Efficient subspace probabilistic parameter optimization for catchment models, *Water Resources Research,* 33, 177–185.

Latour, L.L., Kleinberg, R.L., Mitra, P.P., and C.H. Sotak (1995), Pore-size distributions and tortuosity in heterogeneous porous media, *J. of Mag. Res.*, *112*, 83-91.

Levitt, M.H. (2008), Spin Dynamics, *John Wiley & Sons Ltd.*, West Sussex, England.

Lundberg, P., Ekblad, A., and M. Nilsson (2001), ^{13}C NMR spectroscopy studies of forest soil microbial activity: glucose uptake and fatty acid biosynthesis, *Soil Biology and Biochemistry*, *33*, 621-632.

Marquardt, D.W. (1963), An algorithm for least-squares estimation of nonlinear parameters, *Journal of the Society for Industrial and Applied Mathematics, 11(2)*, 431–441.

Matzkanin, G.A., and R.F. Paetzold (1982), Mesuring soil water content using pulse nuclear magnetic resonance, Am. *Society of Agricultural Engineering Meeting*, *82*, 2619.

Meiboom, S., and D. Gill (1958), *Rev. Sci. Instrum*, *29*, 688.

Mertens, J., Madsen, H., Kristensen, M., Jacques, D., and J. Feyen (2005), Sensitivity of soil parameters in unsaturated zone modeling and the relation between effective, laboratory and *in situ* estimates, *Hydrological Processes, 19*, 1611–1633.

http://www.micromeritics.com, A Few Facts Pertaining to the Low Pressure Performance, *Technical Note*, Verified February 2010.

Mous, S.L. J. (1993), Identification of the movement of water in unsaturated soils: The problem of identifiability of the model, *Journal of Hydrology*, *143*, 153-167.

Mualem, Y. (1976), A new model for predicting the hydraulic conductivity of unsaturated porous media, *Water Resources Research*, *12*, 593-622.

Mualem, Y., and G. Dagan (1978), Hydraulic conductivity of soils: Unified approach to the statistical models, *Soil Sci. Soc. Am. J.*, *42*, 392-395.

Nelder, J.A., and R. Mead (1965), A simplex method for function minimization, *Computer Journal, 7*, 308–313.

Paetzold, R.F., and G.A. Matzkanin (1984), NMR measurements of water in clay, *Bouma, J., Raats, P.A.C. (eds.), Water and solute movement in heavy clay soils, ILRL Publ.37, Proc.ISSS Symp.*, Wageningen, 27-31.

Paetzold, R.F., and G.A. Matzkanin (1985), Surface soil water content measurements using pulsed nuclear magnetic resonance techniques, *Soil sci. Soc. Am. J.*, *49(3)*, 537-540.

Parker, J.C., Kool, J.B., and M.T. van Genuchten (1985), Determining soil hydraulic properties from one-step outflow experiments by parameter estimation: II. Experimental studies, *Soil Science Society of America Journal*, *49*, 1354–1359.

Pohlmeier, A., S. Haber-Pohlmeier and S. Stapf (2009), A Fast Field Cycling Nuclear Magnetic Resonance Relaxometry Study of Natural Soils, *Vadose Zone J.*, *8*, 735-742.

Pohlmeier, A., van Dusschoten, D., Weihermüller, L., Schurr, U., and H. Vereecken (2008), Monitoring water fluxes in porous media by magnetic resonance imaging using D_2O as a tracer, *Magnetic Resonance Imaging*, *27*, 285-292.

Raich, H., and P. Blümler (2004), Design and construction of a dipolar Halbach array with a homogeneous field from identical bar magnets: NMR Mandhalas, *Conc. Magn. Reson. B : Magn. Reson. Eng., 23B*, 16-25.

Randall, E.W., Mathieu, N., and G.I. Ivanova (1997), NMR studies of soil, soil organic matter and nutrients: spectroscopy and imaging, *Geoderma*, *80*, 307-325.

Richards, L.A. (1931), Capillary conduction of liquids through porous media, *Physics*, *1*, 318–333.

Richards, L.A., and M. Fireman (1943), Pressure plate apparatus for measuring moisture sorption and transmission by soils, *Soil Sci*., *56*, 395-404.

Ritter, H.L., and L.C. Drake (1948), Pore-Size Distribution in Porous Materials, *Industrial and Engineering Chemistry*, *17*, 782.

Roth, K. 1996, Lecture notes in soil physics, *http://www.iup.uni-heidelberg.de/institut/ forschung/ groups/ts/soil_physics*, Verified February 2010.

Schaap, M.G., Leij, F.J., and M.Th. van Genuchten (2001), Rosetta: A computer program for estimating soil hydraulic parameters with hierarchical pedotransfer functions, *Journal of Hydrology, 251*, 163-176.

Šimůnek, J., Sejna, M., and M.Th. van Genuchten (1998), The HYDRUS-1D software package for simulating the one-dimensional movement of water, heat, and multiple solutes in variably-saturated media, Version 2.0., *U.S. Salinity Laboratory*, *Agric. Res. Service*, Riverside California.

Scharnagl, B. (2006), Determination of Soil Hydraulic Properties from Multi-Step Outflow Experiments on the Laboratory and Lysimeter Scale, *Diploma Thesis*.

Schaumann, G.E., Hobley, E., Hurraß, J., and W. Rotard (2005), H-NMR relaxometry to monitor wetting and swelling kinetics in high-organic matter soils, *Plant and Soil*, *275*, 1-20.

Song, Y.Q., Venkataramanan, L., Hürlimann, M.D., Flaum, M., Frulla, P., and C. Straley (2002), T_1–T_2 Correlation spectra obtained using a fast two-dimensional Laplace inversion, *Journal of Magnetic Resonance, 154*, 261-268.

Stingaciu, L.R., Pohlmeier, A., Blümler, P., Weihermüller, L., van Dusschoten, D., Stapf, S. and H. Vereecken (2009), Characterization of unsaturated porous media by high-field and low-field NMR relaxometry, *Water Resources Research*, in press.

Stingaciu, L. R., Weihermüller, L., Haber-Pohlmeier, S., Stapf, S., Vereecken, H., and A. Pohlmeier (2010), Determination of pore size distribution and hydraulic properties from Nuclear Magnetic Resonance (NMR) relaxometry: a comparison study of laboratory methods, *Water Resources Research*, accepted.

Straley, C., Rossini, D., Vinegar, H., Tutunjian, P., and C. Morriss (1997), Core Analysis by Low-Field NMR, *Log Analyst*, *38*, 43-56.

Tollner, E.V., and W.L. Rollwitz (1988), Nuclear magnetic resonance for moisture analysis of meals and soils, *Trans. ASAE*, *31(5)*, 1608-1615.

Toormann, A.F., Wierenga, P.J., and R.G. Hills (1992), Parameter estimation of soil hydraulic properties from one-step outflow data, *Water Resources Research, 28*, 3021–3028.

van Dam, J.C., Stricker, J.N.M., and P. Droogers (1990), From One-Step to Multi-Step: Determination of Soil Hydraulic Functions by Outflow Experimens, *Report 7, Agricultural University Wageningen*, Wageningen.

van Dam, J.C., Stricker, J.N.M. and P. Droogers (1992), Inverse method for determining soil hydraulic functions from one-step outflow experiments, *Soil Science Society of America Journal, 56*, 1042–1050.

van Dam, J.C., Stricker, J.N.M. and P. Droogers (1994), Inverse method to determine soil hydraulic functions from multistep outflow experiments, *Soil Science Society of America Journal, 58*, 647–652.

Van Genuchten, M. Th. (1980), A closed-form equation for predicting the hydraulic conductivity of unsaturated soils, *Soil Science Society of America Journal*, *44*, 892-898.

Votrubová, J., Šanda, M., Císlerová, M., Amin, M. H. G., and L. D. Hall (2000), The relationships between MR parameters and the content of water in packed samples of two soils, *Geoderma*, *95*, 267-282.

Washburn, E.W. (1921), The dynamics of capillary flow, *Physical Review*, *17*, 273 - 283.

Webb, A.P. (2001), An introduction to the physical characterization of materials by mercury intrusion porosimetry with emphasis on reduction and presentation of experimental data, *Micromeritics Instrument Corp.*, Georgia, USA.

Weihermüller, L., Huisman, J.A., Graf, A., Herbst, M., and J-M. Sequaris (2009), Multistep outflow experiments to determine soil physical and carbon dioxide production parameters, *Vadose Zone Journal*, *8*, 772-782.

Zachmann, D.W., DuChateau, P.C. and A. Klute (1981), The calibration of the Richards flow equation for a draining column by parameter identification, *Soil Science Society of America Journal, 45*, 1012–1015.

Zachmann, D.W., DuChateau, P.C. and A. Klute (1982), Simultaneous approximation of water capacity and soil hydraulic conductivity by parameter identification, *Soil Science, 134*, 157–163.

Annex 1

Gyromagnetic ratio of the most important spins and their natural abundance

Isotope	Spin	γ (10^6 $s^{-1}T^{-1}$)	Frequency at 4.7T (MHz)	Natural abundance
^{1}H	1/2	42.57	200.05	99.98
^{2}H	1	6.53	30.71	0.01
^{13}C	1/2	10.70	50.30	1.10
^{14}N	1	3.07	14.45	99.63
^{15}N	-1/2	-4.31	20.27	0.37
^{17}O	-5/2	-5.77	27.12	0.037
^{19}F	1/2	40.05	188.24	100
^{23}Na	3/2	11.26	52.91	100
^{31}P	1/2	17.23	80.98	100
^{35}Cl	3/2	4.17	19.60	75.5

Annex 2

Sample	Composition (particle size distribution, %)			Average grain size	Iron content %	Other observations
	sand	silt	clay			
FH31 Medium sand	10 coarse 71 medium 19 fine	0	0	0.36 mm	0.02	<0.005% Mn
W3 Very fine sand	60 fine 7 medium	20 coarse 8 medium 3 fine	2	0.09 mm	0.05	<0.005% Mn
MZ Merzenhausen soil	8	82	10	-	2.8	Orthic Luvisol
Mix5 Clay mixture	95	0	5	-	0.05	FH31+Kaolin
Mix8 Clay mixture	92	0	8	-	0.06	FH31+Kaolin
Mix10 Clay mixture	90	0	10	-	0.08	FH31+Kaolin
Mix15 Clay mixture	85	0	15	-	0.10	FH31+Kaolin
FH32 Fine sand	100	0	0	0.21 mm	0.02	<0.005% Mn
Mix15 fine Clay mixture	85	0	15	-	0.10	FH32+Kaolin
Kaolin	0	0	100	0.1 - 4 µm	0.58	<0.005% Mn

Sediment Classification based on Grain Size (according to USDA, United States Department of Agriculture):

Clay < 0.002 mm; Silt: 0.002 – 0.05 mm; Very fine sand: 0.05 – 0.10; Fine sand: 0.10 – 0.25; Medium sand: 0.25 – 0.50; Coarse sand: 0.50 – 1.00; Very coarse sand: 1.00 – 2.00 mm.

Annex 3

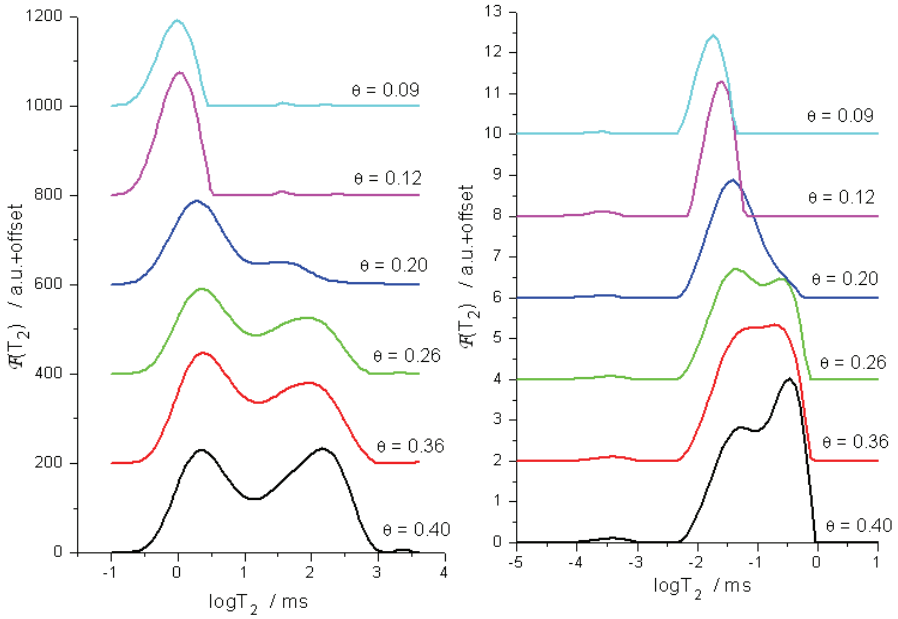

Distribution function F (T_2) for sample Mix10 at different water contents. a) B_0 = 7 T and b) B_0 = 0.1 T. Data fitted according to eq.2.7 using 100 exponentially spaced T_2 values

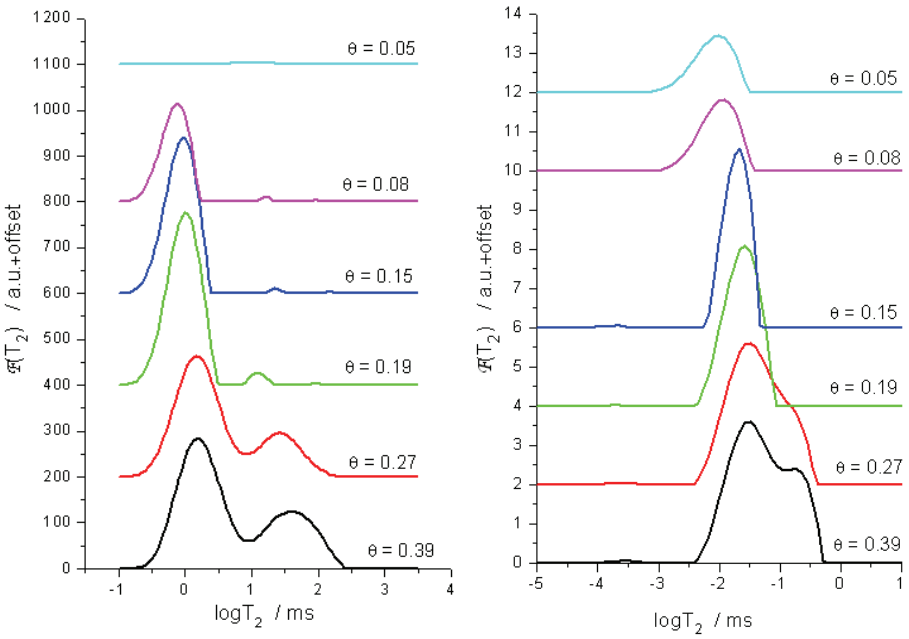

Distribution function F (T_2) for sample Mix15 at different water contents. a) B_0 = 7 T and b) B_0 = 0.1 T. Data fitted according to eq.2.7 using 100 exponentially spaced T_2 values

Annex 4

TABLE 1. Mercury Head Pressure and Pore Sizes Filled at These Pressures								
Pressure Produced as a Function of Depth				Mercury-to-Solid Contact Angle (degrees)				
Pressure	Pressure	Pressure	Pressure	125	130	135	140	145
mmHg	(psi)	dyne/cm^2	Pascals	Maximum Size Pore (µm) Unfilled at Current Pressure				
1	0.019	1.33E+03	133	8346	9353	10289	11147	11920
2	0.039	2.67E+03	267	4173	4677	5145	5573	5960
3	0.058	4.00E+03	400	2782	3118	3430	3716	3973
4	0.077	5.33E+03	533	2087	2338	2572	2787	2980
5	0.097	6.67E+03	667	1669	1871	2058	2229	2384
6	0.116	8.00E+03	800	1391	1559	1715	1858	1987
7	0.135	9.33E+03	933	1192	1336	1470	1592	1703
8	0.155	1.07E+04	1067	1043	1169	1286	1393	1490
9	0.174	1.20E+04	1200	927	1039	1143	1239	1324
10	0.193	1.33E+04	1333	835	935	1029	1115	1192
11	0.213	1.47E+04	1467	759	850	935	1013	1084
12	0.232	1.60E+04	1600	696	779	857	929	993
13	0.251	1.73E+04	1733	642	719	791	857	917
14	0.271	1.87E+04	1867	596	668	735	796	851
15	0.290	2.00E+04	2000	556	624	686	743	795
16	0.309	2.13E+04	2133	522	585	643	697	745
17	0.329	2.27E+04	2266	491	550	605	656	701
18	0.348	2.40E+04	2400	464	520	572	619	662
19	0.367	2.53E+04	2533	439	492	542	587	627
20	0.387	2.67E+04	2666	417	468	514	557	596
21	0.406	2.80E+04	2800	397	445	490	531	568
22	0.425	2.93E+04	2933	379	425	468	507	542
23	0.445	3.07E+04	3066	363	407	447	485	518
24	0.464	3.20E+04	3200	348	390	429	464	497
25	0.483	3.33E+04	3333	334	374	412	446	477
26	0.503	3.47E+04	3466	321	360	396	429	458
27	0.522	3.60E+04	3600	309	346	381	413	441
28	0.541	3.73E+04	3733	298	334	367	398	426
29	0.561	3.87E+04	3866	288	323	355	384	411
30	0.580	4.00E+04	4000	278	312	343	372	397
:	:	:	:	:	:	:	:	:
1.55E+06	30,000.	2.07E+09	2. 07E+08	0.0054	0.0060	0.0066	0.0072	0.0077
3.10E+06	60,000.	4.14E+09	4. 14E+08	0.0027	0.0030	0.0033	0.0036	0.0039
For the pressures shown in the left four columns, all pores larger than the sizes shown in right five columns are filled.								

When one is using mercury intrusion measurements for the characterization of pore size distribution this table, (normally provided together with the technical note of the instrument), shows the pore diameters that can be filled at a certain mercury pressure. Note that the calculation of pore diameters is based on Washburn equation (eq.5.2).

Annex 5

Parameters spaces from the feasibility study MRI-MSO: with index 1- parameters for coarse domain; with index 2- parameters for fine domain

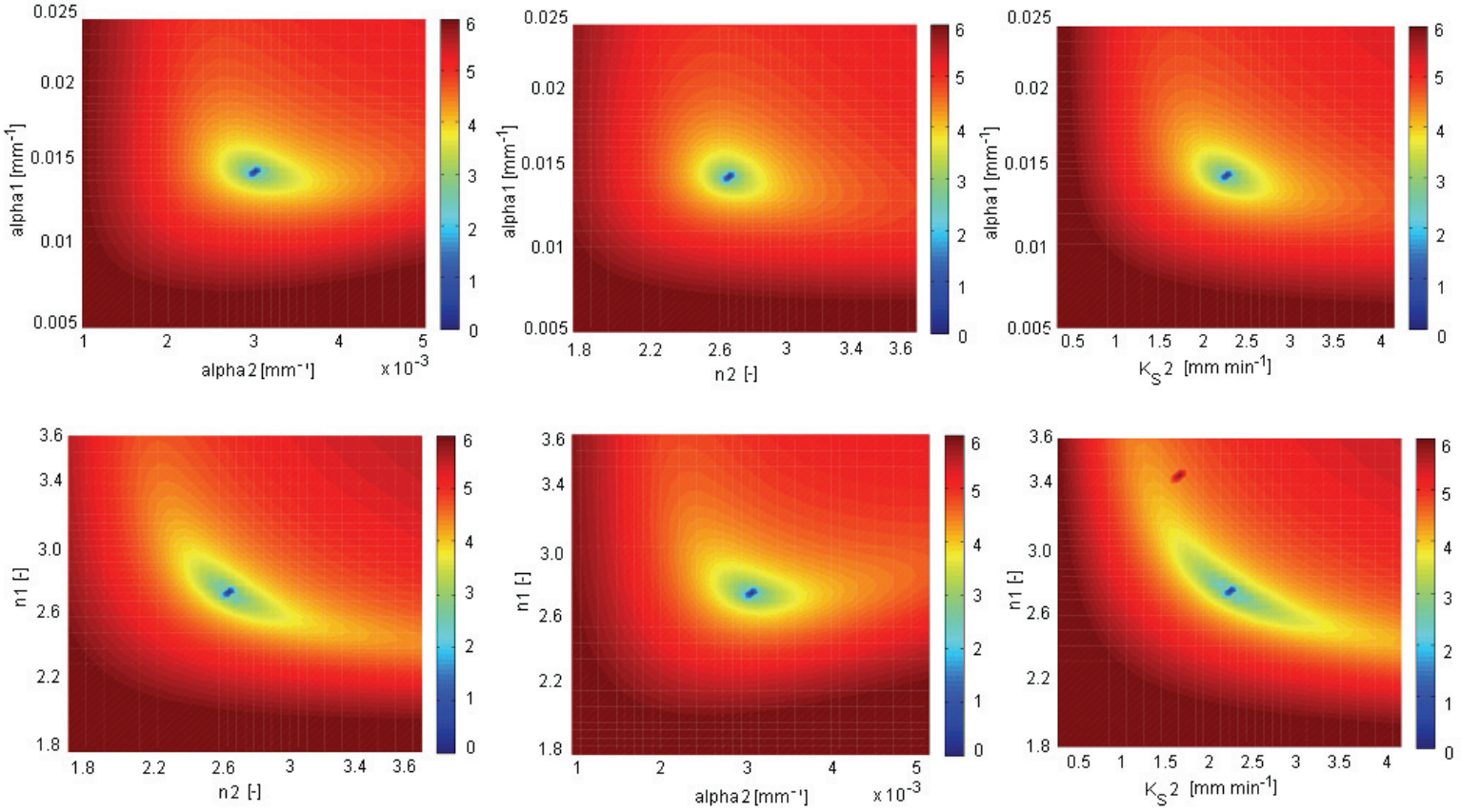

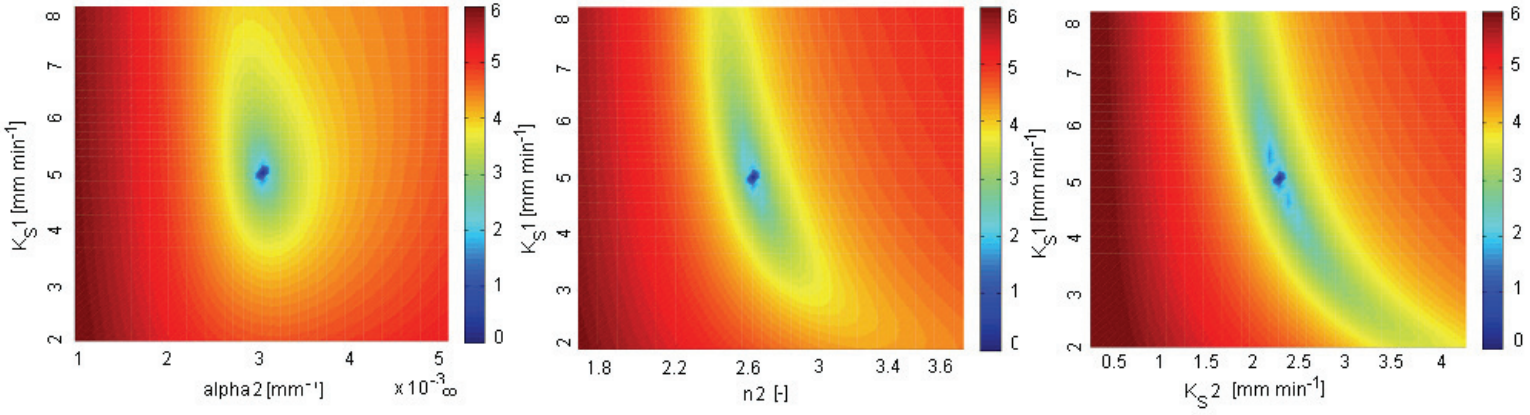

Parameters are not correlated and a unique solution can be distinguished in all plots.

Curriculum Vitae

Personal data

Name: Laura-Roxana Stingaciu

Date of birth: 27 April 1978

Place of birth: Tg-Jiu, Romania

Education

High School:	1984-1992, Elementary & Gymnasium School, Câlceşti, Romania
	1992-1996, Spiru-Haret High School, Tg-Jiu, Romania
	1996, Baccalaureate in sciences
University:	1998-2003, Technical University of Cluj-Napoca Romania, Applied Physics Engineering graduated with diploma & licentiate degree
Master:	2003-2004, master in Processing Materials Engineering graduated with master degree
Current position:	2007 – up to present, PhD Student in FZJ, Jülich, Germany
	2004 – up to present, PhD Student at UTCN, Cluj-Napoca, Romania

Other trainings and academic experiences

November 2007, IDL training course in Research Center Jülich

October 2007 - January 2008, Basics NMR-MRI course, RWTH Aachen

October 2007 - January 2008, Quantum mechanics in NMR course, RWTH Aachen

4 - 7 March 2008, Soil hydrology and geo-statistics course, Bonn University

April 2008, ‘’Hydrus 2D-3D, Modeling training in water flow and contaminant transport in soils’’, Prague, Czech Republic

26 May - 13 June 2008, ‘’In vivo NMR’’ – 7 th PhD Course, Wageningen NMR Centre, The Netherlands

List of publications

1) Stingaciu, L. R., Pohlmeier, A., Blümler, P., Weihermüller, L., van Dusschoten, D., Stapf, S., and H. Vereecken (2009), Characterization of unsaturated porous media by high-field and low-field NMR relaxometry, *Water Resources Research*, in press.

2) Stingaciu, L. R., Weihermüller, L., Haber-Pohlmeier, S., Stapf, S., Vereecken, H., and A. Pohlmeier (2010), Determination of pore size distribution and hydraulic properties from Nuclear Magnetic Resonance (NMR) relaxometry: a comparison study of laboratory methods, *Water Resources Research*, accepted.

3) Stingaciu, L. R., Weihermüller, L., Stapf, S., Vereecken, H., and A. Pohlmeier (2010), Determination of hydraulic properties of model soil column using combined magnetic resonance imaging and multi-step-outflow experiments, *in preparation*.

Schriften des Forschungszentrums Jülich
Reihe Energie & Umwelt / Energy & Environment

1. **Einsatz von multispektralen Satellitenbilddaten in der Wasserhaushalts- und Stoffstrommodellierung – dargestellt am Beispiel des Rureinzugsgebietes**
   von C. Montzka (2008), XX, 238 Seiten
   ISBN: 978-3-89336-508-1

2. **Ozone Production in the Atmosphere Simulation Chamber SAPHIR**
   by C. A. Richter (2008), XIV, 147 pages
   ISBN: 978-3-89336-513-5

3. **Entwicklung neuer Schutz- und Kontaktierungsschichten für Hochtemperatur-Brennstoffzellen**
   von T. Kiefer (2008), 138 Seiten
   ISBN: 978-3-89336-514-2

4. **Optimierung der Reflektivität keramischer Wärmedämmschichten aus Yttrium-teilstabilisiertem Zirkoniumdioxid für den Einsatz auf metallischen Komponenten in Gasturbinen**
   von A. Stuke (2008), X, 201 Seiten
   ISBN: 978-3-89336-515-9

5. **Lichtstreuende Oberflächen, Schichten und Schichtsysteme zur Verbesserung der Lichteinkopplung in Silizium-Dünnschichtsolarzellen**
   von M. Berginski (2008), XV, 171 Seiten
   ISBN: 978-3-89336-516-6

6. **Politikszenarien für den Klimaschutz IV – Szenarien bis 2030**
   hrsg.von P. Markewitz, F. Chr. Matthes (2008), 376 Seiten
   ISBN 978-3-89336-518-0

7. **Untersuchungen zum Verschmutzungsverhalten rheinischer Braunkohlen in Kohledampferzeugern**
   von A. Schlüter (2008), 164 Seiten
   ISBN 978-3-89336-524-1

8. **Inorganic Microporous Membranes for Gas Separation in Fossil Fuel Power Plants**
   by G. van der Donk (2008), VI, 120 pages
   ISBN: 978-3-89336-525-8

9. **Sinterung von Zirkoniumdioxid-Elektrolyten im Mehrlagenverbund der oxidkeramischen Brennstoffzelle (SOFC)**
   von R. Mücke (2008), VI, 165 Seiten
   ISBN: 978-3-89336-529-6

10. **Safety Considerations on Liquid Hydrogen**
    by K. Verfondern (2008), VIII, 167 pages
    ISBN: 978-3-89336-530-2

Schriften des Forschungszentrums Jülich
Reihe Energie & Umwelt / Energy & Environment

11. **Kerosinreformierung für Luftfahrtanwendungen**
    von R. C. Samsun (2008), VII, 218 Seiten
    ISBN: 978-3-89336-531-9

12. **Der 4. Deutsche Wasserstoff Congress 2008 – Tagungsband**
    hrsg. von D. Stolten, B. Emonts, Th. Grube (2008), 269 Seiten
    ISBN: 978-3-89336-533-3

13. **Organic matter in Late Devonian sediments as an indicator for environmental changes**
    by M. Kloppisch (2008), XII, 188 pages
    ISBN: 978-3-89336-534-0

14. **Entschwefelung von Mitteldestillaten für die Anwendung in mobilen Brennstoffzellen-Systemen**
    von J. Latz (2008), XII, 215 Seiten
    ISBN: 978-3-89336-535-7

15. **RED-IMPACT**
    Impact of Partitioning, Transmutation and Waste Reduction Technologies on the Final Nuclear Waste Disposal
    SYNTHESIS REPORT
    ed. by W. von Lensa, R. Nabbi, M. Rossbach (2008), 178 pages
    ISBN 978-3-89336-538-8

16. **Ferritic Steel Interconnectors and their Interactions with Ni Base Anodes in Solid Oxide Fuel Cells (SOFC)**
    by J. H. Froitzheim (2008), 169 pages
    ISBN: 978-3-89336-540-1

17. **Integrated Modelling of Nutrients in Selected River Basins of Turkey**
    Results of a bilateral German-Turkish Research Project
    project coord. M. Karpuzcu, F. Wendland (2008), XVI, 183 pages
    ISBN: 978-3-89336-541-8

18. **Isotopengeochemische Studien zur klimatischen Ausprägung der Jüngeren Dryas in terrestrischen Archiven Eurasiens**
    von J. Parplies (2008), XI, 155 Seiten, Anh.
    ISBN: 978-3-89336-542-5

19. **Untersuchungen zur Klimavariabilität auf dem Tibetischen Plateau - Ein Beitrag auf der Basis stabiler Kohlenstoff- und Sauerstoffisotope in Jahrringen von Bäumen waldgrenznaher Standorte**
    von J. Griessinger (2008), XIII, 172 Seiten
    ISBN: 978-3-89336-544-9

20. **Neutron-Irradiation + Helium Hardening & Embrittlement Modeling of 9%Cr-Steels in an Engineering Perspective (HELENA)**
by R. Chaouadi (2008), VIII, 139 pages
ISBN: 978-3-89336-545-6

21. **in Bearbeitung**

22. **Verbundvorhaben APAWAGS (AOEV und Wassergenerierung) – Teilprojekt: Brennstoffreformierung – Schlussbericht**
von R. Peters, R. C. Samsun, J. Pasel, Z. Porš, D. Stolten (2008), VI, 106 Seiten
ISBN: 978-3-89336-547-0

23. **FREEVAL**
Evaluation of a Fire Radiative Power Product derived from Meteosat 8/9 and Identification of Operational User Needs
Final Report
project coord. M. Schultz, M. Wooster (2008), 139 pages
ISBN: 978-3-89336-549-4

24. **Untersuchungen zum Alkaliverhalten unter Oxycoal-Bedingungen**
von C. Weber (2008), VII, 143, XII Seiten
ISBN: 978-3-89336-551-7

25. **Grundlegende Untersuchungen zur Freisetzung von Spurstoffen, Heißgaschemie, Korrosionsbeständigkeit keramischer Werkstoffe und Alkalirückhaltung in der Druckkohlenstaubfeuerung**
von M. Müller (2008), 207 Seiten
ISBN: 978-3-89336-552-4

26. **Analytik von ozoninduzierten phenolischen Sekundärmetaboliten in *Nicotiana tabacum* L. cv Bel W3 mittels LC-MS**
von I. Koch (2008), III, V, 153 Seiten
ISBN 978-3-89336-553-1

27. **IEF-3 Report 2009. Grundlagenforschung für die Anwendung**
(2009), ca. 230 Seiten
ISBN: 978-3-89336-554-8

28. **Influence of Composition and Processing in the Oxidation Behavior of MCrAlY-Coatings for TBC Applications**
by J. Toscano (2009), 168 pages
ISBN: 978-3-89336-556-2

29. **Modellgestützte Analyse signifikanter Phosphorbelastungen in hessischen Oberflächengewässern aus diffusen und punktuellen Quellen**
von B. Tetzlaff (2009), 149 Seiten
ISBN: 978-3-89336-557-9

30. **Nickelreaktivlot / Oxidkeramik – Fügungen als elektrisch isolierende Dichtungskonzepte für Hochtemperatur-Brennstoffzellen-Stacks**
von S. Zügner (2009), 136 Seiten
ISBN: 978-3-89336-558-6

31. **Langzeitbeobachtung der Dosisbelastung der Bevölkerung in radioaktiv kontaminierten Gebieten Weißrusslands – Korma-Studie**
von H. Dederichs, J. Pillath, B. Heuel-Fabianek, P. Hill, R. Lennartz (2009), Getr. Pag.
ISBN: 978-3-89336-532-3

32. **Herstellung von Hochtemperatur-Brennstoffzellen über physikalische Gasphasenabscheidung**
von N. Jordán Escalona (2009), 148 Seiten
ISBN: 978-3-89336-532-3

33. **Real-time Digital Control of Plasma Position and Shape on the TEXTOR Tokamak**
by M. Mitri (2009), IV, 128 pages
ISBN: 978-3-89336-567-8

34. **Freisetzung und Einbindung von Alkalimetallverbindungen in kohlebefeuerten Kombikraftwerken**
von M. Müller (2009), 155 Seiten
ISBN: 978-3-89336-568-5

35. **Kosten von Brennstoffzellensystemen auf Massenbasis in Abhängigkeit von der Absatzmenge**
von J. Werhahn (2009), 242 Seiten
ISBN: 978-3-89336-569-2

36. **Einfluss von Reoxidationszyklen auf die Betriebsfestigkeit von anodengestützten Festoxid-Brennstoffzellen**
von M. Ettler (2009), 138 Seiten
ISBN: 978-3-89336-570-8

37. **Großflächige Plasmaabscheidung von mikrokristallinem Silizium für mikromorphe Dünnschichtsolarmodule**
von T. Kilper (2009), XVII, 154 Seiten
ISBN: 978-3-89336-572-2

38. **Generalized detailed balance theory of solar cells**
by T. Kirchartz (2009), IV, 198 pages
ISBN: 978-3-89336-573-9

39. **The Influence of the Dynamic Ergodic Divertor on the Radial Electric Field at the Tokamak TEXTOR**
von J. W. Coenen (2009), xii, 122, XXVI pages
ISBN: 978-3-89336-574-6

40. **Sicherheitstechnik im Wandel Nuklearer Systeme**
von K. Nünighoff (2009), viii, 215 Seiten
ISBN: 978-3-89336-578-4

41. **Pulvermetallurgie hochporöser NiTi-Legierungen für Implanat- und Dämpfungsanwendungen**
von M. Köhl (2009), XVII, 199 Seiten
ISBN: 978-3-89336-580-7

42. **Einfluss der Bondcoatzusammensetzung und Herstellungsparameter auf die Lebensdauer von Wärmedämmschichten bei zyklischer Temperaturbelastung**
von M. Subanovic (2009), 188, VI Seiten
ISBN: 978-3-89336-582-1

43. **Oxygen Permeation and Thermo-Chemical Stability of Oxygen Permeation Membrane Materials for the Oxyfuel Process**
by A. J. Ellett (2009), 176 pages
ISBN: 978-3-89336-581-4

44. **Korrosion von polykristallinem Aluminiumoxid (PCA) durch Metalljodidschmelzen sowie deren Benetzungseigenschaften**
von S. C. Fischer (2009), 148 Seiten
ISBN: 978-3-89336-584-5

45. **IEF-3 Report 2009. Basic Research for Applications**
(2009), 217 Seiten
ISBN: 978-3-89336-585-2

46. **Verbundvorhaben ELBASYS (Elektrische Basissysteme in einem CFK-Rumpf) - Teilprojekt: Brennstoffzellenabgase zur Tankinertisierung - Schlussbericht**
von R. Peters, J. Latz, J. Pasel, R. C. Samsun, D. Stolten
(2009), xi, 202 Seiten
ISBN: 978-3-89336-587-6

47. **Aging of ^{14}C-labeled Atrazine Residues in Soil: Location, Characterization and Biological Accessibility**
by N. D. Jablonowski (2009), IX, 104 pages
ISBN: 978-3-89336-588-3

48. **Entwicklung eines energetischen Sanierungsmodells für den europäischen Wohngebäudesektor unter dem Aspekt der Erstellung von Szenarien für Energie- und CO_2 - Einsparpotenziale bis 2030**
von P. Hansen (2009), XXII, 281 Seiten
ISBN: 978-3-89336-590-6

59. **Sorption of polycyclic aromatic hydrocarbon (PAH) to Yangtze River sediments and their components**
by J. Zhang (2010), X, 109 pages
ISBN: 978-3-89336-616-3

60. **Weltweite Innovationen bei der Entwicklung von CCS-Technologien und Möglichkeiten der Nutzung und des Recyclings von CO_2**
Studie im Auftrag des BMWi
von W. Kuckshinrichs et al. (2010), X, 139 Seiten
ISBN: 978-3-89336-617-0

61. **Herstellung und Charakterisierung von sauerstoffionenleitenden Dünnschichtmembranstrukturen**
von M. Betz (2010), XII, 112 Seiten
ISBN: 978-3-89336-618-7

62. **Politikszenarien für den Klimaschutz V – auf dem Weg zum Strukturwandel, Treibhausgas-Emissionsszenarien bis zum Jahr 2030**
hrsg. von P. Hansen, F. Chr. Matthes (2010), 276 Seiten
ISBN: 978-3-89336-619-4

63. **Charakterisierung Biogener Sekundärer Organischer Aerosole mit Statistischen Methoden**
von C. Spindler (2010), iv, 163 Seiten
ISBN: 978-3-89336-622-4

64. **Stabile Algorithmen für die Magnetotomographie an Brennstoffzellen**
von M. Wannert (2010), ix, 119 Seiten
ISBN: 978-3-89336-623-1

65. **Sauerstofftransport und Degradationsverhalten von Hochtemperatur-membranen für CO2-freie Kraftwerke**
von D. Schlehuber (2010), VII, 139 Seiten
ISBN: 978-3-89336-630-9

66. **Entwicklung und Herstellung von foliengegossenen, anodengestützten Festoxidbrennstoffzellen**
von W. Schafbauer (2010), VI, 164 Seiten
ISBN: 978-3-89336-631-6

67. **Disposal strategy of proton irradiated mercury from high power spallation sources**
by S. Chiriki (2010), xiv, 124 pages
ISBN: 978-3-89336-632-3

68. **Oxides with polyatomic anions considered as new electrolyte materials for solid oxide fuel cells (SOFCs)**
by O. H. Bin Hassan (2010), vii, 121 pages
ISBN: 978-3-89336-633-0

Schriften des Forschungszentrums Jülich
Reihe Energie & Umwelt / Energy & Environment

69. **Von der Komponente zum Stack: Entwicklung und Auslegung von HT-PEFC-Stacks der 5 kW-Klasse**
von A. Bendzulla (2010), IX, 203 Seiten
ISBN: 978-3-89336-634-7

70. **Satellitengestützte Schwerewellenmessungen in der Atmosphäre und Perspektiven einer zukünftigen ESA Mission (PREMIER)**
von S. Höfer (2010), 81 Seiten
ISBN: 978-3-89336-637-8

71. **Untersuchungen der Verhältnisse stabiler Kohlenstoffisotope in atmosphärisch relevanten VOC in Simulations- und Feldexperimenten**
von H. Spahn (2010), IV, 210 Seiten
ISBN: 978-3-89336-638-5

72. **Entwicklung und Charakterisierung eines metallischen Substrats für nanostrukturierte keramische Gastrennmembranen**
von K. Brands (2010), vii, 137 Seiten
ISBN: 978-3-89336-640-8

73. **Hybridisierung und Regelung eines mobilen Direktmethanol-Brennstoffzellen-Systems**
von J. Chr. Wilhelm (2010), 220 Seiten
ISBN: 978-3-89336-642-2

74. **Charakterisierung perowskitischer Hochtemperaturmembranen zur Sauerstoffbereitstellung für fossil gefeuerte Kraftwerksprozesse**
von S.A. Möbius (2010) III, 208 Seiten
ISBN: 978-3-89336-643-9

75. **Characterization of natural porous media by NMR and MRI techniques: High and low magnetic field studies for estimation of hydraulic properties**
by L.-R. Stingaciu (2010), 96 pages
ISBN: 978-3-89336-645-3